Canadian Mineralogist
Vol. 17, pp. 785-830 (1979)

ELECTRON-MICROPROBE AND X-RAY-MICROBEAM STUDIES OF SERPENTINE TEXTURES

F. J. WICKS

Department of Mineralogy and Geology, Royal Ontario Museum, Toronto, Ontario M5S 2C6

A. G. PLANT

Geological Survey of Canada, 601 Booth Street, Ottawa, Ontario K1A 0E8

ABSTRACT

Studies by microbeam X-ray camera and electron microprobe indicate that the serpentine minerals in retrograde lizardite ± chrysotile ± brucite pseudomorphic textures become progressively more homogeneous and, in most cases, more Mg-rich as serpentinization progresses. Whereas lizardite ± brucite mesh-textures develop in a retrograde environment, the closely related lizardite ± brucite hourglass-textures are probably formed by a mild prograde event. Aluminum is a minor but persistent element in the mesh and hourglass textures, but lizardite-bastites after pyroxenes have distinctly higher Al and Cr contents. During prograde metamorphism, recrystallization of retrograde pseudomorphic textures usually begins in the fine-grained lizardite ± chrysotile mesh-centres. Relict olivine mesh-centres may alter to chrysotile + brucite or, at higher temperatures, to antigorite + brucite. Chrysotiles are usually slightly less Fe-rich, and antigorites either more or less Fe-rich, than the serpentine in the textures being replaced. Compositions tend to become more homogeneous with prolonged recrystallization to prograde nonpseudomorphic textures. However, prograde shearing produces variable Fe contents in the resulting chrysotiles and antigorites. Bastites undergo complex mineralogical and chemical changes during prograde metamorphism. In the simplest case, lizardite-bastites remain more or less unchanged by the development of prograde chrysotile + brucite. The development of antigorite + brucite may have two effects on lizardite-bastites: they may undergo a drastic loss of Fe and recrystallize directly to antigorite, or they may lose or gain Fe and Al and recrystallize to a chlorite-like mineral + antigorite. The development of antigorite without brucite may or may not produce a loss of Fe and Al from lizardite-bastites, but it may produce a recrystallization to Povlen-type chrysotile, without much visible effect on the bastites. Many of the veins that develop in the various assemblages have compositions closely related to those of the host minerals. However, veins of very different compositions also develop and these may or may not react with the wallrock minerals, depending on conditions at the time of crystallization.

SOMMAIRE

Des études par diffraction X (chambre à microfaisceau) et à la microsonde électronique montrent que les minéraux de serpentine dans les assemblages rétrogrades lizardite ± chrysotile ± brucite à textures pseudomorphes deviennent progressivement plus homogènes et, en général, plus magnésiens à mesure que progresse la serpentinisation. Les textures réticulées de lizardite ± brucite sont caractéristiques d'un milieu en rétromorphose, tandis que les textures en sablier du même assemblage signalent probablement un faible métamorphisme prograde. Toute serpentine, de l'une ou l'autre texture, contient un peu d'aluminium, mais les bastites à lizardite, formées à partir de pyroxènes, ont des teneurs en Al et Cr nettement supérieures. La recristallisation de textures pseudomorphes rétrogrades au cours du métamorphisme prograde débute généralement aux centres des mailles de la texture réticulée de lizardite ± chrysotile. Les reliques d'olivine qui s'y trouvent peuvent se transformer en chrysotile + brucite ou, à températures plus élevées, en antigorite + brucite. Ces chrysotiles sont généralement un peu moins ferrifères que la serpentine en voie de remplacement, tandis que les antigorites sont soit plus, soit moins ferrifères. Les compositions tendent à s'homogénéiser par recristallisation prolongée en textures progrades non-pseudomorphes, mais le cisaillement prograde produit une teneur en Fe variable dans les chrysotiles et antigorites. Les bastites subissent des modifications minéralogiques et chimiques compliquées pendant le métamorphisme prograde. Dans le cas le plus simple, les bastites à lizardite restent quasi inchangées durant la formation prograde de chrysotile + brucite. Lors de la cristallisation d'antigorite + brucite, les bastites à lizardite peuvent soit subir une perte énorme de Fe pour donner de l'antigorite, soit perdre ou recevoir Fe + Al pour donner un minéral chloritique + antigorite. La formation d'antigorite sans brucite peut ou non être accompagnée d'une perte en Fe et Al dans les bastites à lizardite, mais elle provoque la recristallisation d'un chrysotile de type Povlen, sans grand effet sur les bastites. Nombre de veinules qui se forment dans les divers assemblages ont une composition en relation étroite avec celles des minéraux encaissants. On trouve pourtant aussi des

veines de composition totalement différente, qui peuvent ou non réagir avec les minéraux des épontes, selon les conditions lors de la cristallisation.

(Traduit par la Rédaction)

INTRODUCTION

In previous papers the crystal chemistry of the serpentine minerals (Whittaker & Wicks 1970, Wicks & Whittaker 1975) and the mineralogy of serpentine textures (Wicks *et al.* 1977, Wicks & Whittaker 1977) were discussed. Although a model for serpentinization in various geological settings was proposed by Wicks & Whittaker (1977), few chemical data were presented; of the chemical analyses that were available, most pertain to vein serpentine and few to rock-forming serpentine (Whittaker & Wicks 1970). In order to obtain a better understanding of the chemistry of the rock-forming serpentine minerals and the serpentinization process, a combined electron-microprobe and X-ray-microbeam study has been undertaken as a companion study to the earlier X-ray-microbeam survey (Wicks & Whittaker 1977).

Since the discussion of the classification of the serpentine minerals by Wicks & Whittaker (1975), more data have become available on the polygonal structure of Povlen-type serpentines (Cressey & Zussman 1976, Middleton & Whittaker 1976, Morandi & Felice 1979). Povlen-type serpentines have been found with cylindrical cores of chrysotile–$2M_{c1}$ or chrysotile–$2Or_{c1}$, each with polygonal overgrowths of serpentine that approximates the chrysotile–

TABLE 1. TYPE OF SERPENTINIZATION, ROCK TYPES AND SAMPLE LOCATION

RETROGRADE		
TYPE 1 - ANTIGORITE ± MAGNETITE		
IB67-249	wehrlite	Tadamagouche Creek, Yukon
TYPE 3 - LIZARDITE ± MAGNETITE		
18479	harzburgite	Stillwater, Montana
18480	harzburgite	Stillwater, Montana
18491	dunite	Bowden Lake, Manitoba
18530	harzburgite	Mayaguez, Puerto Rico
18540*	harzburgite	Jeffrey mine, Quebec (also Type 7)
AG67-67b*	dunite	Jeffrey mine, Quebec (also Type 7)
FW-L-4	harzburgite	Lizard, England
TYPE 3 - LIZARDITE + BRUCITE ± MAGNETITE		
18508	dunite	Glen Urquhart, Scotland
18529	dunite	Mayaguez, Puerto Rico
AG67-70a	dunite	Jeffrey mine, Quebec
TYPE 3 - CHRYSOTILE + LIZARDITE ± BRUCITE ± MAGNETITE		
AG67-64a*	wehrlite	Jeffrey mine, Quebec (also Type 7)
IB67-265*	dunite	Telson Lake, Yukon
W70-72*	dunite	Normandie mine, Quebec (also Type 7)
PROGRADE		
TYPE 5 - CHRYSOTILE ±/OR LIZARDITE ± BRUCITE ± MAGNETITE		
18501	poss. dunite	Pipe Lake mine, Manitoba
18538	harzburgite	Jeffrey mine, Quebec (also Type 3)
18559	serpentinite	Porcupine Asbestos mine, Ontario
TYPE 6 - CHRYSOTILE ± LIZARDITE ± MAGNETITE		
W70-74	serpentinite	Normandie mine, Quebec (also Types 3 and 7)
TYPE 7 - ANTIGORITE + BRUCITE ± MAGNETITE		
18544	harzburgite	Jeffrey mine, Quebec (also Type 3)
W70-35	dunite	National Asbestos mine, Quebec (also Type 3)
W70-41a	dunite	National Asbestos mine, Quebec (also Types 3 and 5)
W70-55	dunite	Beaver mine, C Pit, Quebec (also Types 3 and 5)
W75-62	serpentinite	Bell Asbestos mine, Quebec (also Type 5)
TYPE 7 - ANTIGORITE ± MAGNETITE		
18478	peridotite	Stillwater, Montana (also Type 3)
18498	serpentinite	Oswagen Lake, Manitoba
18540	harzburgite	Jeffrey mine, Quebec (also Type 3)
18543	harzburgite	Jeffrey mine, Quebec (also Type 3)
AG67-64a	wehrlite	Jeffrey mine, Quebec (also Type 3)
AG67-67b	dunite	Jeffrey mine, Quebec (also Type 3)
W70-72	dunite	Normandie mine, Quebec (also Type 3)
W76-5	serpentinite	Flintkote mine, Quebec (also Type 3)
TYPE 8 - ANTIGORITE ± MAGNETITE		
T-179	serpentinite	Talon, Quebec (also Type 3)

*The development of the textures in these samples, although closely related to pseudomorphic processes of type 3, is promoted by mild prograde metamorphism of type 5. Thus, some of these textures form a link between types 3 and 5.

$2M_{c1}$ and lizardite–$2H$ structures, respectively (Middleton & Whittaker 1976). Recently, polygonal parachrysotile has been discovered (Middleton & Whittaker 1979). Transmission electron-microscopy (TEM) of ion-thinned samples (Cressey & Zussman 1976, Cressey 1979) has provided more detailed information on the morphology and distribution of the various serpentine minerals within different textural units and on the nature of the serpentinization process. In field and theoretical phase-diagram studies, Evans and his coworkers (as reviewed in Evans 1977) have unraveled many details of the serpentinization process, particularly in the prograde regime. Hydrothermal studies on the composition and stability of lizardite (Chernosky 1975, Caruso & Chernosky 1979) and the stability of antigorite (Evans *et al.* 1976), and microprobe studies of serpentine textures (Page 1967, 1968, Trommsdorff & Evans 1972, Frost 1975, Dungan 1979a, b) have provided further data on the serpentinization process. The distribution of Cl in partly serpentinized ultramafic rocks has been studied by Rucklidge & Patterson (1977).

In order to relate some of these studies to the work of Wicks & Whittaker (1977) and to test the model of serpentinization proposed in that study, a series of samples representing the various serpentine minerals and the various types of serpentinization were selected for microprobe analysis. Some of the samples had been identified by Wicks & Whittaker (1977) but many new samples were added to fill in types not completely covered by the earlier study (Table 1). It is the purpose of this paper to discuss the chemistry of the serpentine minerals and the various processes of serpentinization.

ANALYTICAL METHODS

Two thin-sections were made from each sample, usually from back-to-back slices, one left uncovered for the microbeam camera and one polished for the microprobe. Both types of section were examined optically to select areas for analysis. Previous microprobe studies have been limited by the uncertainties of the identification of some of the serpentine minerals, but in our study all serpentine-mineral assemblages to be studied with the electron microprobe were identified with the microbeam X-ray-diffraction camera (Wicks & Zussman 1975). A total of 310 microbeam X-ray-diffraction patterns were taken. Furthermore, all analyses of individual points within the selected areas were recorded on photomicrographs. The examination of the polished thin-sections in reflected light served as an aid in distinguishing antigorite from lizardite and chrysotile: antigorite is slightly harder and thus takes a better polish. This distinction is illustrated in Figures 15a and 15b where the same field of view is seen in transmitted and reflected light, respectively, and where antigorite blades are clearly distinguished from the enclosing chrysotile in reflected light. Lizardite usually takes a good polish, although it is softer than antigorite, and chrysotile takes a good-to-poor polish depending on its morphology and orientation with respect to the plane of the thin section.

Recent TEM studies of ion-thinned samples from the Wicks & Whittaker (1977) study (Cressey & Zussman 1976, Cressey 1979) have definitely shown that some serpentine textures are morphologically and mineralogically more complex than the microbeam-camera results would suggest. In particular, mesh centres after olivine, though mainly lizardite, often contain fine chrysotile and polygonal Povlen-type serpentine, which does not produce a recognizable microbeam diffraction-pattern. The presence of chrysotile may be suggested on microbeam X-ray-diffraction patterns by diffuse fogging of the film in the 202 to 204 region (Wicks & Whittaker 1977) but cannot be proved positively. The presence of semicircular polygonal serpentine in bastites (Cressey 1979) is consistent with the asymmetrical distribution of intensities and the gross similarity of lizardite microbeam diffraction-patterns to chrysotile-fibre X-ray-diffraction patterns (WZ, Fig. 6m; for brevity, references made to figures in Wicks & Zussman (1975), Wicks, Whittaker & Zussman (1977) and Wicks & Whittaker (1977) are referred to as WZ, WWZ and WW respectively). However, minor amounts of chrysotile could be masked in this type of microbeam pattern. In spite of the greater detail provided by the TEM on minor components, the larger X-ray microbeam does give a better representative average of the main components, over an area roughly comparable with the area analyzed by the microprobe. The microbeam X-ray camera is, therefore, the best instrument to use in conjunction with the electron microprobe.

There is a problem in the identification of two-layer structures, chrysotile–$2Or_{c1}$ and lizardite–$2H$ (Wicks 1979). Both produce the same series of $20l$ reflections but with different intensities. It is not possible on most microbeam diffraction-patterns to make the intensity measurements necessary to distinguish these two structures, particularly in mixtures with other structures. The following convention has been adopted in this paper for ambiguous cases. Where a two-layer structure was noted in association with chrysotile–$2M_{c1}$ it has been called chrysotile–$2Or_{c1}$, and where in association with lizardite–$1T$ it has been called lizardite–$2H$.

Microprobe analyses of olivine, pyroxene and serpentine assemblages identified by the microbeam camera are reported in Tables 2 to 13. These 197 average analyses, which represent a selection of 772 analyses from the 1140 individual analyses available, were obtained using a Materials Analysis Company electron microprobe equipped with a Kevex energy-dispersive spectrometer Model 5000A, and automated to produce simultaneous multi-element analysis and data reduction (Plant & Lachance 1973). Operating conditions were as follows: 20 kV accelerating voltage, specimen current of 10 nA measured on a standard kaersutite, and a counting time of 100 seconds. Under these conditions no effects of volatilization of the minerals under electron-beam bombardment were observed. For the serpentine analyses, a natural serpentine (Aumento 1967) was used as a standard for Mg and Si, with kaersutite for Al, Ca and Fe, chromite for Cr, biotite for Mn and Cl, and a synthetic Ni-bearing magnetite for Ni. A series of mineral and synthetic standards was used for olivine and pyroxene. Although no statistical analysis of the data has been undertaken, the precision of the replicate analyses of the standard serpentine and other standards indicate that the determinations have a relative accuracy of $\pm$ 1 to 2% for major elements and up to $\pm$ 10% for minor elements. In addition to the reported elements Si, Al, Cr, Fe, Mn, Mg, Ca, Na and K, the energy-dispersive spectra permit the identification of any other element with atomic number > 10 that may be present. All spectra were monitored for significant concentrations of other elements but Ni and Cl were the only other elements identified. Minor Ni was noted in most olivine and serpentine after olivine, and lesser amounts usually were noted in pyroxene and serpentine after pyroxene but it is not specifically reported. However, where minor Cl was detected it has been noted in the text. Two samples, FW–L–4 and 18540, were selected for detailed analysis of Ni and Cl distribution using wavelength-dispersive spectrometers. During analysis care was taken to avoid fine grains of magnetite and other opaque minerals, and in most cases, with the aid of the energy-dispersive spectrometer, it was possible to do this. However, in some samples very fine grained magnetite and sulfides were evenly dispersed through the sample; it was impossible to be certain that they were avoided during analysis. These cases are noted in the tables and the text.

To simplify the presentation of the data, the analyses of homogeneous serpentines have been grouped and an average analysis is given in the tables. For inhomogeneous serpentines individual analyses are reported. The analyses are primarily intended to illustrate the migration of elements during serpentinization and were not gathered specifically as mineral analyses. Iron is reported as FeO in the analyses and in the calculation of cation values. These were calculated on the basis of 14 oxygens for the serpentines, 4 oxygens for olivine and 6 oxygens for the pyroxenes but, to conserve space, have not been included in the tables.

CHEMICAL COMPOSITION OF THE SERPENTINE MINERALS

Electron-microprobe analyses of serpentines are limited because the H_2O^+ content and ferrous–ferric ratio cannot be determined. Ideally the major elements calculated as oxides should total 87% for chrysotile and lizardite and about 88% for an average antigorite. The actual H_2O^+ contents of chemically analyzed chrysotile and lizardite tend to exceed the ideal 13%, whereas antigorites tend to be under 13% (Whittaker & Wicks 1970). This general trend was usually noted in the difference from 100% in our micropobe analyses, though it must be emphasized that the results cannot be used as an indirect determination of the H_2O^+ content.

The lack of data on the oxidation state of Fe is a further difficulty in the interpretation of the microprobe analyses. In the limited number of wet-chemical analyses (22) examined by Whittaker & Wicks (1970), there is a very strong tendency for Fe to be in the trivalent state in lizardites ($Fe^{3+}/Fe^{2+} = 7.0$ to ∞), a weaker tendency for Fe to be in the trivalent state in chrysotiles ($Fe^{3+}/Fe^{2+} = 1.0$ to 9.0), and a moderately strong tendency for Fe to be in the divalent state, or at least for the divalent and trivalent states to be equal, in antigorite ($Fe^{3+}/Fe^{2+} = 0$ to 1.2). Recent Mössbauer studies of Fe in serpentines (Blaauw *et al.* 1979, Rozenson *et al.* 1979) have indicated that in some cases Fe^{3+}/Fe^{2+} ratios are significantly different from those determined by classical chemical methods. Rozenson *et al.* suggest that Fe^{3+}/Fe^{2+} trends noted by Whittaker & Wicks (1970) may not be as definite as suggested.

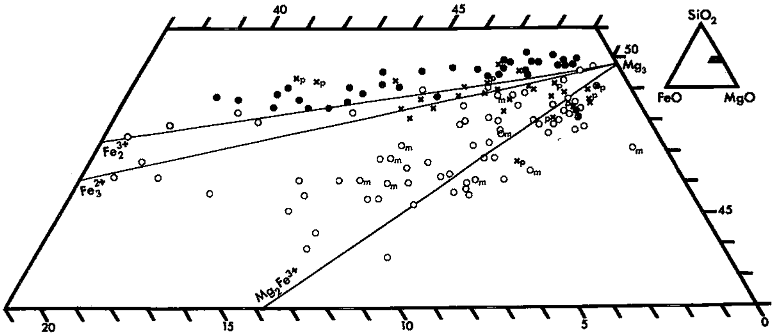

FIG. 1. MgO–FeO–SiO_2 diagram. A selection of microprobe analyses of antigorite, chrysotile and lizardite from the present study. Symbols are the same as in Figure 4.

The Fe^{3+}/Fe^{2+} ratio in serpentine minerals is a reflection of the oxidation/reduction environment in which the minerals formed. Many, but not all, lizardites are formed in an oxidizing retrograde environment, most antigorites in a reducing prograde environment, and chrysotile in both. Thus one would expect many lizardites to be Fe^{3+}-dominant and many antigorites to be Fe^{2+}-dominant, but it would not be surprising to find exceptions to these generalizations. In spite of these limitations, the results of the microprobe study can be compared with, and extend the earlier study of, samples analyzed by wet chemistry and discussed by Whittaker & Wicks (1970).

Representative microprobe analyses are plotted on an MgO–FeO–SiO_2 triangular diagram in Figure 1. The FeO represents the total Fe content calculated as FeO. [In discussing these diagrams the corresponding relative proportions of the components of each diagram are described as "values" to distinguish them from the true "contents".] The selected analyses represent the compositional range of the antigorites, chrysotiles and lizardites, including Povlen-type serpentine and multilayer lizardite polytypes encountered in this study. In discussing compositions on these diagrams it is useful to refer to a series of lines joining ideal compositions: (1) $Mg_3Si_2O_5(OH)_4$ – $(Mg_2Fe^{3+})(SiFe^{3+})O_5(OH)_4$, (2) $Mg_3Si_2O_5(OH)_4$ – $Fe^{2+}_3Si_2O_5(OH)_4$ and (3) $Mg_3Si_2O_5(OH)_4$ – $Fe^{3+}_2Si_2O_5(OH)_4$, respectively abbreviated the Mg_3–Mg_2Fe^{3+}, Mg_3–Fe^{2+}_3 and Mg_3–Fe^{3+}_2 composition lines. The first two composition-lines involve trioctahedral structures but the last, Mg_3–Fe^{3+}_2, joins the trioctahedral serpentine composition to the dioctahedral ferric analogue of kaolinite plotted in terms of FeO. It is not suggested that the relationship of a point to one of these composition lines be used to determine the oxidation state of the Fe, but it does give some idea of how an analysis relates to ideal compositions. The position of the points plotted is also affected by the substitution of other elements, mainly Al, not included in this plot. For instance, several of the lizardites and the chrysotiles that plot below the Mg_3–Mg_2Fe^{3+} composition line contain appreciable amounts of Al substituting for Si, which accounts for their positions below the line. Associated brucite and talc can also influence the plot but analyses of samples in which impurities were detected with the microbeam camera are omitted from this diagram.

Antigorites (Fig. 1) lie above the Mg_3–Fe^{2+}_3 composition line and illustrate the SiO_2 enrichment and MgO depletion relative to the ideal stoichiometric ratio, which is produced by the systematic omission of Mg, Fe and OH at points of inversion in the antigorite structure (Kunze 1956, 1958, 1961, Wicks & Whittaker 1975).

Lizardites, including the common 1*T* and less common multilayer polytypes, have a wide distribution. Most plot closer to the Mg_3–Mg_2Fe^{3+} composition line than to the other two composition lines, but there is a second group that plots along the Mg_3–Fe^{2+}_3 and Mg_3–Fe^{3+}_2 composition lines. Chrysotiles and the Povlen-type serpentines, most of which are at least in part chrysotile-$2M_{c1}$, plot in several positions. Most Fe-poor chrysotiles plot near or below the Mg_3–Mg_2Fe^{3+} composition line. A second group of more Fe-rich chrysotiles plot along the Mg_3–Fe^{2+}_3 and Mg_3–Fe^{3+}_2 composition lines. A third smaller group of Fe-poor to Fe-rich chrysotiles plot well above the Mg_3–Fe^{3+}_2 composition line, in the area occupied by antigorites. The maximum FeO value of chrysotile and Povlen-type

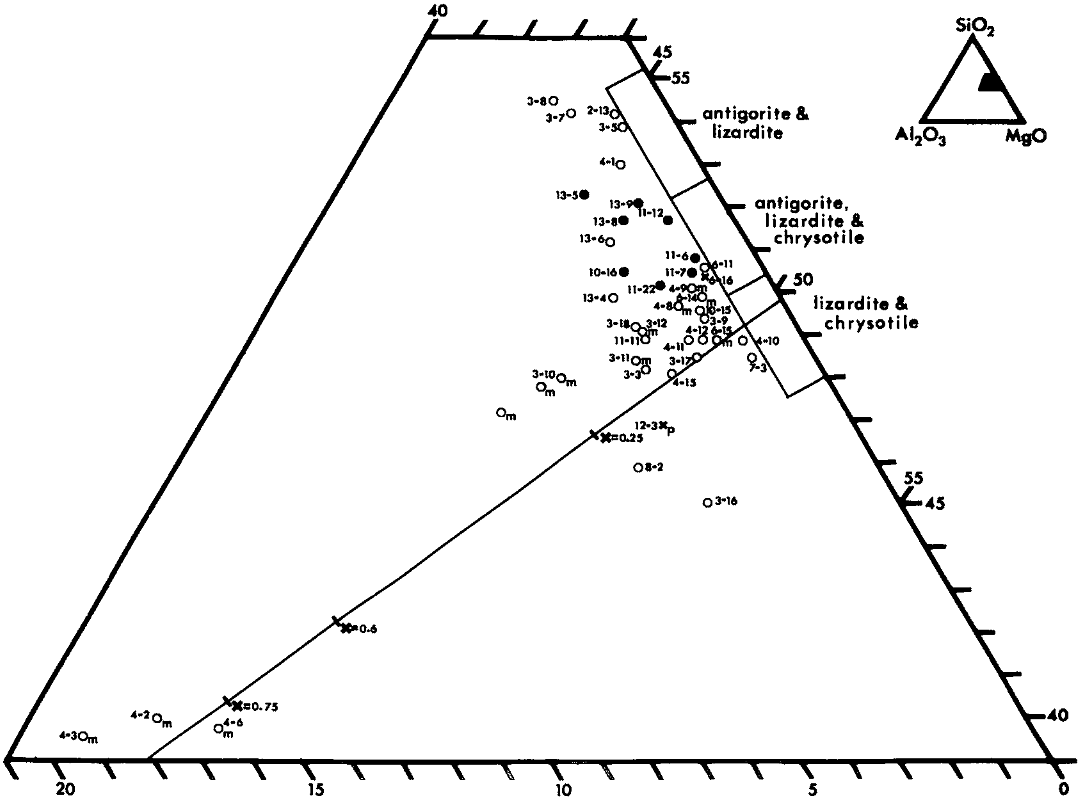

FIG. 2. MgO–Al₂O₃–SiO₂ diagram. A selection of microprobe analyses of antigorite, chrysotile and lizardite from the present study. The three rectangles outline areas of high concentrations of analyses. The line joins the compositions $Mg_3Si_2O_5(OH)_4$ and $(Mg_2Al)(SiAl)O_5(OH)_4$. Symbols are the same as in Figure 4. The numbers refer to the analyses given in the tables.

chrysotile is 9% on Figure 1, significantly less than lizardite at 16% FeO or antigorite at 12% FeO. All these are appreciably greater than the FeO values of 3% for chrysotile, 6% for lizardite and 7% for antigorite found by Whittaker & Wicks (1970). The multilayer lizardites analyzed all have low (1%) to intermediate (10%) FeO values.

Figure 2, an MgO–Al_2O_3–SiO_2 triangular diagram, contains representative analyses to illustrate the range of Al contents. Most specimens analyzed have Al_2O_3 values of less than 1%. Thus Al is not a major component of most of the antigorites, chrysotiles and lizardites studied. The serpentines with Al_2O_3 values below 1% can be subdivided into three groups on Figure 2: (1) chrysotiles and lizardites plotting between values of 48 to 50.2% SiO_2, (2) chrysotiles, lizardites and antigorites plotting between 50.2 to 52.6% SiO_2, and (3) lizardites and antigorites plotting between 52.6 to 55.2% SiO_2. The first group of chrysotiles and lizardites, including Povlen-types, plot around the ideal composition and are similar to those studied by Whittaker & Wicks (1970). The antigorites of the second group also plot where the antigorites of Whittaker & Wicks plotted, but the chrysotiles and lizardites in this group, including Povlen-types, and the antigorites and lizardites of the third group are anomalous in comparison with the earlier study. These are all Fe-rich, Mg-poor serpentines not included in the earlier study; this Fe-for-Mg substitution shifts them to higher SiO_2 values on the MgO–Al_2O_3–SiO_2 diagram.

Two chrysotiles have Al_2O_3 values of greater than 1% (Fig. 2: 6-16, 12-3) and eight antigorites attain Al_2O_3 values of 3%. Many lizardites plot at or below the 1% Al_2O_3 value but, in contrast to the chrysotiles and antigorites, lizardites, generally from bastites, plot out to 7% Al_2O_3 and a few, from veins, plot at 19% Al_2O_3.

The Si occupancy of the tetrahedral sites is illustrated in Figure 3. The majority of the

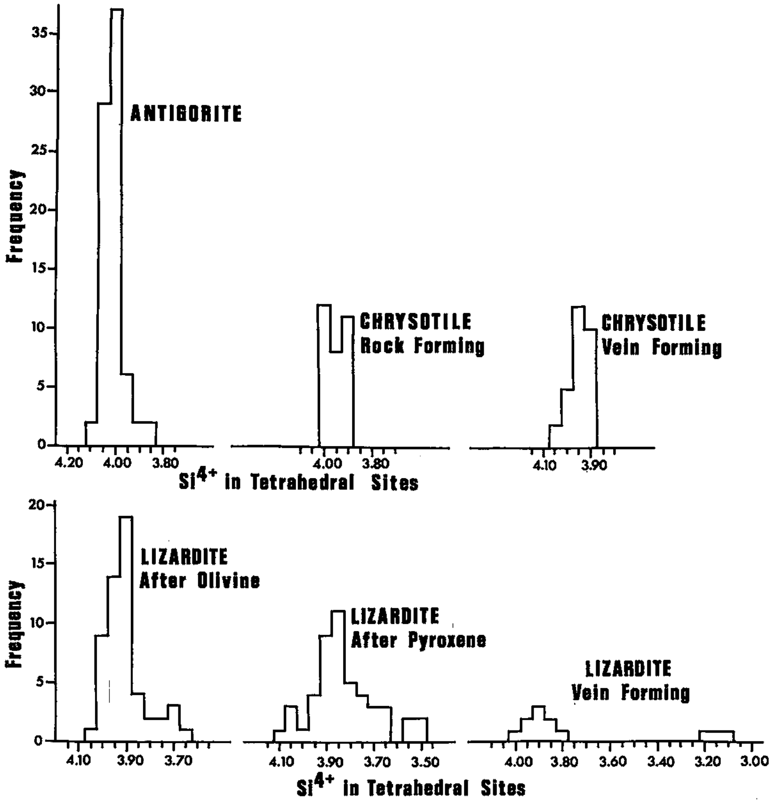

FIG. 3. Frequency of occupancy of the tetrahedral sites by Si^{4+} for various serpentine minerals.

antigorites seem to the filled completely, or overfilled, by Si but this is in part produced by the method of calculating the formula on the basis of 14(O), which does not take into account the effect of the omission of Mg and OH in the antigorite structure (Wicks 1979). Adjusting for this would shift the occupancy by approximately 0.10, so that the majority of the antigorites would be shifted from 4.05 and 4.00 to 3.95 and 3.90. A discussion and interpretation of Figures 1 to 3 are presented at the end of the paper.

A MODEL OF THE SERPENTINIZATION PROCESS

A possible model of the serpentinization process was described by Wicks & Whittaker (1977). Eight processes were described, four retrograde and four prograde. The retrograde processes from the higher- to lower-temperature assemblages are: Type 1, antigorite ± magnetite pseudomorphic textures formed in the absence of substantial shearing; Type 2, antigorite nonpseudomorphic foliated textures formed during shearing; Type 3, lizardite ± brucite ± magnetite pseudomorphic textures formed in the absence of substantial shearing, and Type 4, chrysotile + lizardite ± brucite ± magnetite nonpseudomorphic foliated textures formed during shearing. The prograde processes from the lower- to higher-temperature assemblages are: Type 5, chrysotile ± lizardite ± brucite ± magnetite nonpseudomorphic textures formed in the absence of substantial shearing; Type 6, chrysotile ± lizardite ± brucite ± magnetite nonpseudomorphic foliated textures formed during shearing; Type 7, antigorite ± brucite ± magnetite nonpseudomorphic textures formed in the absence of substantial shearing, and Type 8, antigorite ± brucite ± magnetite nonpseudomorphic foliated textures formed during shearing. No examples of types 2 and 4 were examined. This model will be used as an outline for the description of the results obtained for the samples examined in this study, and will be modified slightly by the interpretation of these results.

Type 1: antigorite

Type-1 serpentinization is represented by a single sample, IB67–249 (Table 1) in this study.

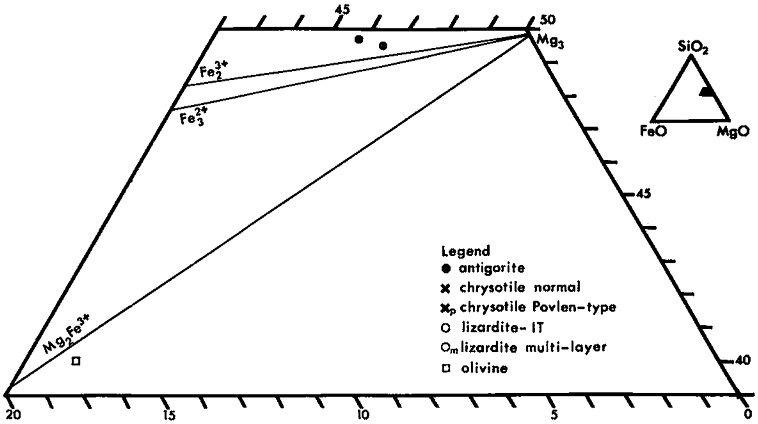

FIG. 4. MgO–FeO–SiO$_2$ diagram for type 1. IB67–249. Olivine alteration to antigorite. The symbols in the legend apply to all the triangular diagrams.

TABLE 2. RETROGRADE TYPE-3 LIZARDITE AFTER OLIVINE

Sample No.	FW-L-4				18480						
Analysis No.	1	2	3	4	5	6	7	8	9	10	11
Pts. Analyzed	5	1	2	1	4	2	2	2	3	1	1
SiO_2	41.3	39.6	38.1	40.8	40.0	40.3	39.7	38.8	38.9	47.6	43.5
Al_2O_3	0.0	0.34	0.78	0.20	0.0	0.15	0.18	0.27	0.26	0.23	0.21
Cr_2O_3	0.0	0.0	0.0	0.0	0.0	0.0	0.0	0.0	0.0	0.0	0.0
FeO^*	9.9	5.3	10.1	5.7	14.8	8.4	9.4	12.3	13.4	11.8	14.9
MnO	0.08	0.0	0.11	0.16	0.16	0.0	0.02	0.09	0.12	0.14	0.15
MgO	48.9	41.2	38.7	31.8	44.8	37.2	38.1	33.0	32.0	27.9	27.4
CaO	0.0	0.0	0.0	0.18	0.0	0.0	0.0	0.0	0.0	0.0	0.0
NiO	0.36	0.29	0.36	0.51		-	-	-	-	-	-
Cl	0.0	0.32	0.20	0.18	-	-	-	-	-	-	-
Less O ≡ Cl		0.07	0.05	0.04							
Total	100.54	86.98	88.30	79.49	99.76	86.05	87.40	84.46	84.68	87.67	86.16

Sample No.	18479				18491				18540	AG67-67b
Analysis No.	12	13	14	15	16	17	18	19	20	21
Pts. Analyzed	1	2	1	4	3	6	2	2	10	8
SiO_2	38.2	39.5	38.5	42.3	44.0	41.7	41.5	42.6	42.7	41.9
Al_2O_3	0.27	0.78	0.36	0.89	0.18	0.17	0.19	0.16	0.26	0.32
Cr_2O_3	0.0	0.0	0.0	0.04	0.0	0.0	0.01	0.01	0.03	0.0
FeO^*	9.8	12.5	11.3	12.5	0.60	1.5	0.93	1.5	5.0	2.8
MnO	0.08	0.12	0.0	0.19	0.0	0.02	0.03	0.0	0.04	0.05
MgO	36.8	32.5	34.4	31.3	43.9	41.4	41.3	41.8	39.3	42.7
CaO	0.0	0.10	0.01	0.16	0.0	0.01	0.0	0.0	0.0	0.0
NiO	-	-	-	-	-	-	-	-	0.31	-
Cl	-	-	-	-	-	-	-	-	0.0	-
Less O ≡ Cl										
Total	85.15	85.50	84.57	87.38	88.68	84.80	83.96	86.07	87.64	87.77

Analysis Nos. 1 and 5, olivine Fo$_{91}$ and Fo$_{84}$ respectively; 2, 3, 6, 7, 12, 13, and 17, lizardite-1*T* mesh rims; 16, lizardite-1*T* central parting in mesh rim; 8, 9, 14, 18, and 19, lizardite-1*T* mesh centres, 18 without spherical inclusions and 19 with fine spherical inclusions of nickel sulfide; 4, 10, 11, and 15, lizardite-1*T* + ? anomalous mesh centres; 20 and 21, lizardite-1*T* hourglass texture.

*Total iron calculated as FeO.

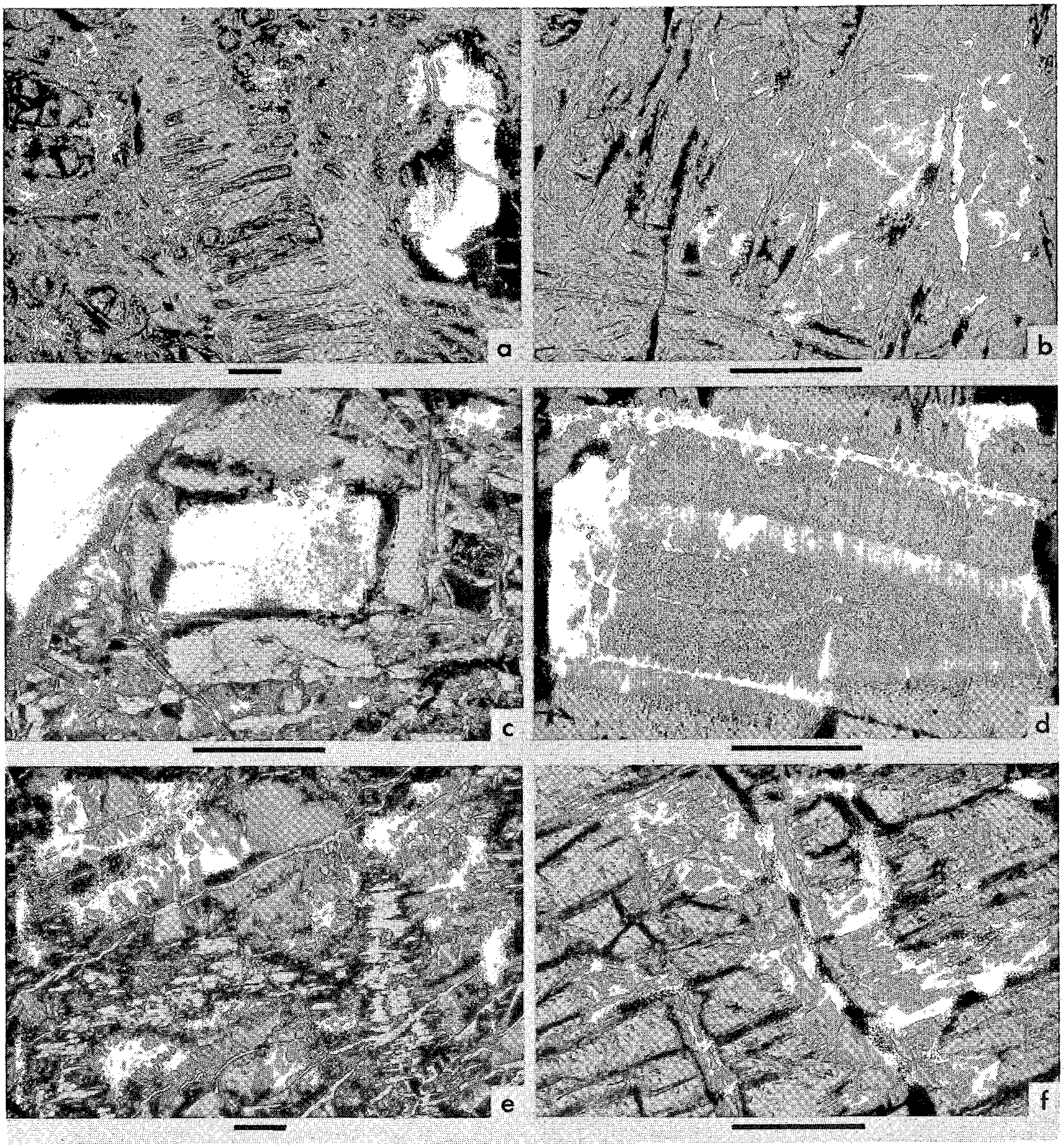

FIG. 5. (a) Mesh rims of lizardite–1*T* (2–2, 2–3) + magnetite, mesh centres of olivine (2–1) and intermediate, high-relief, Si-rich material (2–4) left side and top centre, lizardite–1*T* bastite (3–2, 3–3) and relict enstatite (3–1) central portion, lizardite–1*T* (3–16, 3–17) and dusty brown alteration after diopside (3–15) right side. Sample FW–L–4, plane-polarized light. (b) Mesh rims of lizardite–1*T* (2–6, 2–7) lined with magnetite, mesh centres of olivine (2–5), intermediate high-relief, Si-rich material (2–10, 2–11) and normal lizardite–1*T* (2–8, 2–9). Sample 18480, plane-polarized light. (a) Mesh rims of lizardite–1*T* (4–10, 4–11), small mesh-centres of lizardite–1*T* (4–13), large mesh-centre of multilayer lizardite (4–9) with magnetite along mesh-rim–centre boundary, vein of multilayer lizardite (4–9) top left. Sample 18530. Partly crossed nicols. (d) Central parting of lizardite–1*T* (2–16), mesh rims of lizardite–1*T* (2–17), mesh centres of lizardite–1*T* without (2–18) and with very fine spheres of nickel–iron sulfide (2–19). Sample 18491. Crossed nicols. (e) Hourglass texture of lizardite–1*T* (2–21) partly replaced by antigorite blades (11–1) and cut by fine chrysotile–$2M_{c1}$ and minor $2Or_{c1}$ cross-fibre-asbestos veins (4–17). Sample AG67–67b. Crossed nicols. (f) Early lizardite–1*T* bastite (3–5) adjacent to fracture (sinuous black line), later lizardite–1*T* bastite (3–6) adjacent to enstatite (3–4). Sample 18480. Crossed nicols. All numbers refer to analyses in the tables. Bar represents 0.2 mm.

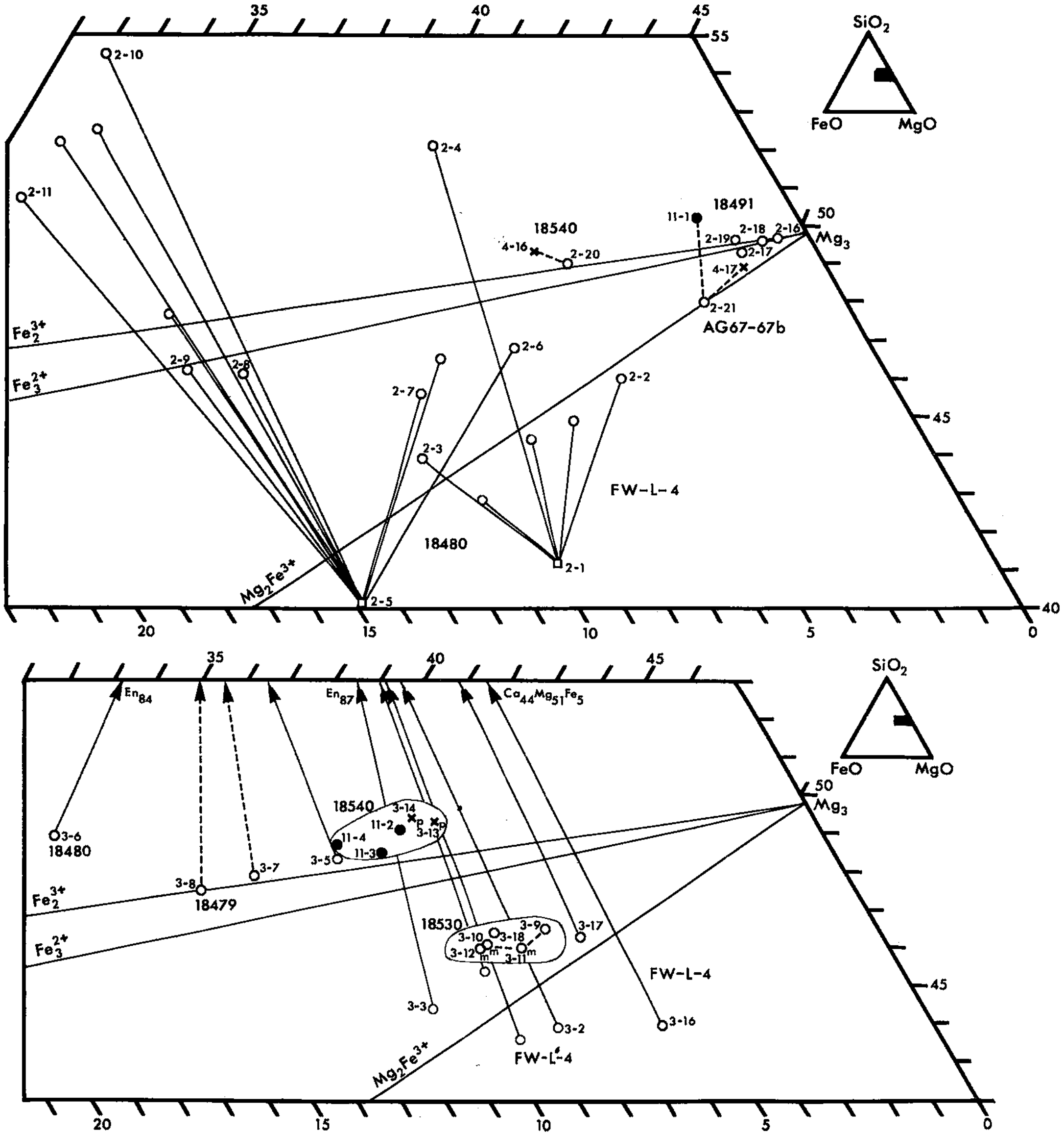

FIG. 6. MgO–FeO–SiO$_2$ diagrams for type 3. Upper figure: olivine alteration. FW–L–4: 2–1 olivine Fo$_{90}$, 2–2, 2–3 and associated points, lizardite–1T mesh-rims, 2–4 lizardite–1T in intermediate, high-relief, Si-rich mesh-centre. 18480: 2–5 olivine Fo$_{84}$, 2–6, 2–7 and associated point, lizardite–1T mesh-rims, 2–8, 2–9 and associated point, lizardite–1T mesh-centres, 2–10, 2–11 and associated points, lizardite–1T in intermediate, high-relief, Si-rich mesh-centres. 18491: 2–16 lizardite–1T central parting of mesh rim, 2–17 lizardite–1T mesh-rims, 2–18 lizardite–1T mesh-centres, 2–19 lizardite–1T and spherical nickel sulfide inclusions. 18540: 2–20 lizardite–1T hourglass-textures, 4–16 chrysotile–2M_{c1} cross-fibre-asbestos veins. AG67–67b: 2–21 lizardite–1T hourglass-texture, 4–17 chrysotile–2M_{c1} + minor 2Or_{c1} cross-fibre-asbestos veins, 11–1 antigorite after lizardite hourglass. Lower figure: pyroxene alteration. FW–L–4: 3–2, 3–3 and associated points, lizardite–1T bastite after enstatite, 3–16 and 3–17 lizardite–1T after diopside. 18479: 3–7 and 3–8 lizardite–1T after enstatite. 18480: 3–5 and 3–6 lizardite–1T after enstatite. 18530: 3–9 lizardite–1T bastite partly after enstatite and partly vein, 3–10, 3–11 and 3–12 multilayer-lizardite bastites after enstatite, 3–18 lizardite–1T bastites after clinopyroxene. 18540: 3–13 and 3–14 Povlen-type chrysotile–2M_{c1} and 2Or_{c1} + minor Povlen-type parachrysotile after enstatite, 11–2, 11–3 and 11–4 antigorite blades after Povlen-type chrysotile.

(It should be noted that this sample is listed mistakenly as type 3 in WW, Table 1 and Fig. 1c. The location in the caption in WW, Fig. 1a should be Tadamagouche Creek, not Telson Lake). Microprobe analyses yielded the following: olivine, average of five points, SiO_2 40.1, FeO 16.8, MnO 0.21, MgO 43.4, CaO 0.02, total 100.53; antigorite, average of two points, SiO_2 44.5, Al_2O_3 0.23, FeO 3.6, MnO 0.08, MgO 41.9, CaO 0.21, total 90.52; antigorite, average of five points, SiO_2 44.6, Al_2O_3 0.21, Cr_2O_3 0.02, FeO 4.1, MnO 0.04, MgO 41.1, total 90.07.

The olivine (Fo_{82}) has been altered along grain boundaries and fractures to antigorite + magnetite, forming a mesh texture of antigorite mesh-rims and forsterite mesh-centres (WW,

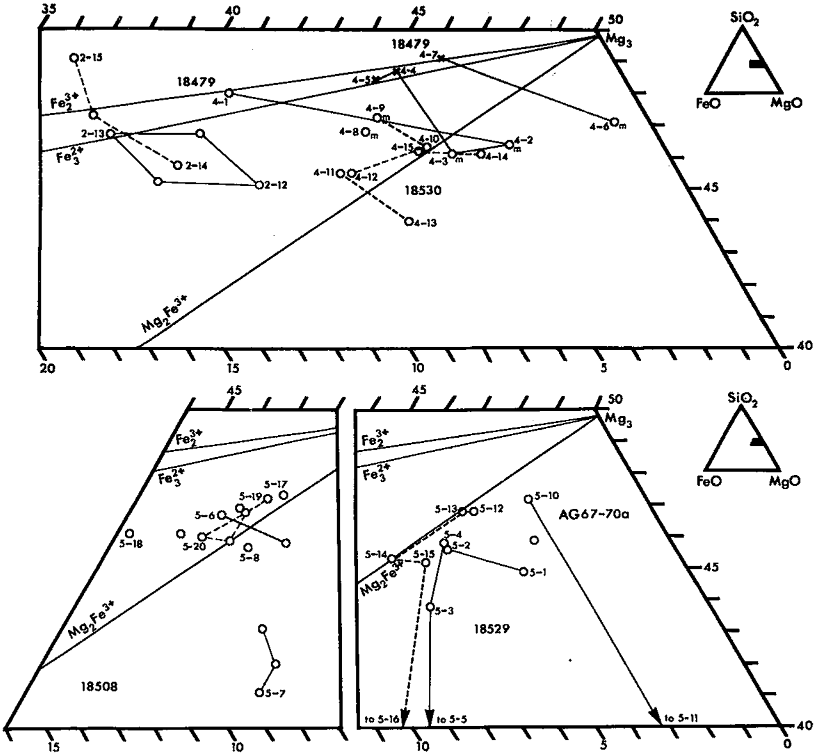

FIG. 7. MgO–FeO–SiO_2 diagrams for type 3. Upper figure: olivine alteration and veins. 18479: 2–12, 2–13 and associated points, lizardite–1*T* mesh-rims, 2–14, 2–15 and associated point, lizardite–1*T* mesh-centres, 4–1 lizardite–1*T* early vein, 4–2, 4–3 and 4–6 multilayer-lizardite continuous marginal zone, 4–4, 4–5 and 4–7 chrysotile–$2M_{c1}$ central zone. 18530: 4–10, 4–11 and 4–14 lizardite–1*T* mesh-rims, 4–12, 4–13 and 4–15 lizardite–1*T* mesh-centres, 4–9 multilayer-lizardite mesh-centre, 4–8 and 4–9 multilayer-lizardite veins. Lower figure: olivine and other silicate alteration to lizardite–1*T* ± brucite. 18529: 5–2 lizardite–1*T* mesh-rim, 5–1 and 5–3 lizardite–1*T* + brucite mesh-rim, 5–4 lizardite–1*T* mesh-centres, 5–5 brucite + lizardite–1*T* mesh-centre, 5–12 lizardite–1*T* + minor 2*H* marginal zone of bastite, 5–13 lizardite–1*T* colorless interior of bastite, 5–14 lizardite–1*T* pale brown interior, 5–15 lizardite–1*T* + brucite red-brown central zone, 5–16 brucite + lizardite–1*T* red-brown central zone. 18508: 5–6 and associated point, lizardite–1*T* ± brucite central parting of mesh rim, 5–7 and associated points, lizardite–1*T* + brucite mesh-rims, 5–8 lizardite–1*T* grey and colorless mesh-centres, 5–19, 5–20 and associated points, lizardite–1*T* bastite after talc, 5–17, 5–18 and all associated points not already accounted for, lizardite–1*T* bastite after amphibole. AG67–70a: 5–10 lizardite–1*T* hourglass and associated point, lizardite–1*T* + brucite hourglass, 5–11 brucite grain.

Fig. 1c). The magnetite occupies former forsterite grain-boundaries and the central partings of the antigorite mesh-rims. The antigorite contains considerably less Fe and more Al than the olivine, and plots well above the Mg_3–$Fe^{2+}{}_3$ composition line (Fig. 4), as is typical of antigorite.

Type 3: lizardite ± chrysotile ± brucite

Type-3 serpentinization occurs in a retrograde or static environment at lower temperatures than type 1. Several samples of three different assemblages were analyzed: lizardite ± magnetite, lizardite + brucite ± magnetite, and chrysotile + lizardite ± brucite ± magnetite (Table 1). All are pseudomorphic textures.

Lizardite after olivine. The early of lizardite ± magnetite development is represented by samples FW–L–4 and 18480 (Table 1) in which the olivines are 70 to 90% serpentinized. The olivine (Fo_{90}) in FW–L–4 produced colorless lizardite-1*T* mesh-rims (Table 2) with both lesser and greater Fe values than the original olivine (Fig. 6, 2–1, 2–2, 2–3: in these pairs of numbers, the first number is the table number and the second is

TABLE 3. RETROGRADE TYPE-3 LIZARDITE AFTER PYROXENE

Sample No.	FW-L-4			18480			18479	
Analysis No.	1	2	3	4	5	6	7	8
Pts. Analyzed	5	5	1	4	2	3	3	6
SiO_2	54.4	36.1	37.9	55.4	41.2	40.3	40.0	39.2
TiO_2	0.07	0.07	0.04	0.03	0.0	0.08	0.11	0.11
Al_2O_3	4.6	3.8	2.8	1.8	0.83	2.2	1.5	1.6
Cr_2O_3	0.56	0.63	0.41	0.59	0.02	0.80	0.59	0.64
FeO^*	6.6	7.8	9.4	9.5	9.6	14.3	11.2	12.2
MnO	0.10	0.14	0.15	0.15	0.11	0.21	0.17	0.15
MgO	32.5	38.8	38.0	31.4	34.4	27.9	32.4	31.2
CaO	1.4	0.03	0.0	1.3	0.07	0.08	0.07	0.07
NiO	0.09	0.10	0.10	-	-	-	-	-
Cl	0.0	0.13	0.10	-	-	-	-	-
Less O ≡ Cl	-	0.03	0.02	-	-	-	-	-
Total	100.32	87.57	88.88	100.17	86.23	85.87	86.04	85.17

Sample No.	18530				18540		FW-L-4			18530
Analysis No.	9	10	11	12	13	14	15	16	17	18
Pts. Analyzed	5	3	3	3	4	3	7	1	2	4
SiO_2	39.3	37.8	38.2	38.3	42.7	42.1	50.9	36.6	40.3	36.7
TiO_2	0.02	0.03	0.0	0.05	0.0	0.0	0.18	0.10	0.05	0.04
Al_2O_3	1.4	4.1	2.8	2.4	0.51	0.30	5.8	3.1	1.9	2.4
Cr_2O_3	0.07	0.61	0.61	0.73	0.43	0.39	0.93	1.0	0.18	0.32
FeO^*	6.3	7.4	6.9	7.6	7.4	7.8	3.3	5.1	5.9	6.9
MnO	0.07	0.15	0.05	0.06	0.11	0.13	0.03	0.0	0.08	0.22
MgO	38.9	36.8	37.8	37.3	36.4	35.4	17.6	41.5	40.9	35.5
CaO	0.04	0.08	0.02	0.01	0.10	0.09	21.0	0.04	0.09	0.34
NiO	-	-	-	-	0.28	0.23	0.06	0.03	0.05	-
Cl	-	-	-	-	0.0	0.0	0.0	0.31	0.21	-
Less O ≡ Cl	-	-	-	-	-	-	-	0.07	0.05	-
Total	86.10	86.97	86.38	86.45	87.93	86.44	99.80	87.71	89.61	82.42

Analysis Nos. 1 and 4, orthopyroxene ($Ca_3Mg_{87}Fe_{10}$ and $Ca_2Mg_{84}Fe_{14}$ respectively); 2, 3, 5, 6, 7, 8, and 9, lizardite-1*T*; 10 and 11, multi-layer lizardite; 12, multi-layer lizardite and unidentified sulfide, broad beam analysis; 13 and 14, Povlen-type chrysotile-$2M_{c1}$ and $2Or_{c1}$ + minor parachrysotile; 15, clinopyroxene ($Ca_{44}Mg_{51}Fe_5$); 16, 17, and 18, lizardite-1*T*.

*Total iron calculated as FeO.

the analysis number within that table), as well as cloudy lenses of very fine-grained magnetite within the mesh rims and along some mesh-rim–centre boundaries (Fig. 5a). The olivine (Fo_{84}) in 18480 produces colorless to very pale yellow lizardite–1*T* mesh-rims with less Fe than the original olivine (Table 2, Fig. 6: 2–5, 2–6, 2–7). The secondary magnetite produced occurs in irregular grains and lenses along the mesh-rim–centre boundaries so that both the rims and centres are largely clear of magnetite (Fig. 5b).

In FW–L–4 the mesh centres are usually composed of relict olivine, but some pale green, high-relief alteration material that seems to be intermediate between olivine and serpentine occurs infrequently in some mesh centres. In 18480 a similar intermediate type of yellow to yellow-brown high-relief alteration material occurs in some mesh centres between the relict olivine and the mesh rims (Fig. 5b). In both cases this material gives lizardite–1*T* microbeam diffraction-patterns that vary from diffuse to sharp, and both have anomalously high Si contents (Fig. 6: 2–4, 2–10, 2–11). Other mesh centres in 18480 contain normal randomly oriented yellow lizardite–1*T*, and plot near the Mg_3–$Fe^{2+}{}_3$ composition line with Fe values similar to the original olivine (Fig. 6: 2–8, 2–9).

An intermediate stage of complete serpentinization is represented by samples 18479 and 18530 (Table 1). Sample 18479 is similar to 18480 but serpentinization is slightly more advanced and the Fe content of the lizardite–1*T* mesh rims and centres (Table 2) is more closely grouped but still variable (Fig. 7: 2–12 to 2–15). A thin selvage of the high-relief mesh-centre material plots at a slightly less anomalous SiO_2 value than those in 18480 (Fig. 7: 2–15). In

TABLE 4. RETROGRADE TYPE-3 VEINS AND RECRYSTALLIZATION

Sample No.	18479						
Analysis No.	1	2	3	4	5	6	7
Pts. Analyzed	2	3	3	2	2	6	4
SiO_2	41.4	31.9	31.3	41.4	41.2	33.2	42.0
Al_2O_3	1.2	13.9	15.1	0.70	0.78	13.6	0.84
Cr_2O_3	0.0	0.0	0.0	0.02	0.02	0.0	0.0
FeO^*	9.4	2.8	4.0	5.1	5.7	0.64	3.9
MnO	0.13	0.44	0.43	0.15	0.25	0.37	0.17
MgO	35.5	34.0	32.7	38.5	38.2	36.7	39.6
CaO	0.03	0.03	0.08	0.0	0.0	0.0	0.0
NiO	-	-	-	-	-	-	-
Cl	-	-	-	-	-	-	-
Total	87.66	83.07	83.61	85.87	86.15	84.51	86.51

Sample No.	18530								18540	AG67-67b
Analysis No.	8	9	10	11	12	13	14	15	16	17
Pts. Analyzed	3	6	8	2	3	2	2	2	8	5
SiO_2	39.6	40.4	38.9	37.9	37.6	33.9	39.0	37.6	43.0	42.4
Al_2O_3	1.7	1.3	0.98	1.8	1.5	4.1	0.58	2.3	0.39	0.40
Cr_2O_3	0.0	0.0	0.0	0.0	0.0	0.0	0.0	0.0	0.06	0.0
FeO^*	6.6	6.3	5.4	7.6	7.3	6.1	4.3	5.4	5.6	1.6
MnO	0.04	0.07	0.07	0.12	0.13	0.0	0.03	0.11	0.06	0.07
MgO	38.4	38.9	39.7	37.9	37.8	36.9	41.4	38.3	38.6	42.7
CaO	0.02	0.0	0.11	0.24	0.17	0.05	0.04	0.17	0.0	0.0
NiO	-	-	-	-	-	-	-	-	0.28	-
Cl	-	-	-	-	-	-	-	-	0.0	-
Total	86.36	86.97	85.16	85.56	84.50	81.05	85.35	83.88	87.99	87.17

Analysis No. 1, lizardite-1*T* early vein associated with 2 to 7; 2, 3, and 6, multi-layer lizardite continuous marginal zone of vein; 4, 5, and 7, chrysotile-$2M_{c1}$ central zone of vein; 8, multi-layer lizardite vein; 9, multi-layer lizardite vein and mesh centre; 10, 11, and 14, lizardite-1*T* mesh rim; 12, 13, and 15, lizardite-1*T* mesh centre; 16, chrysotile-$2M_{c1}$ cross-fibre asbestos veins; 17, chrysotile-$2M_{c1}$ and minor $2Or_{c1}$ cross-fibre asbestos veins.

*Total iron calculated as FeO.

sample 18530 (Table 4, Fig. 5c), serpentinization is more advanced than in sample 18749. The lizardite–1*T* mesh-rims (Fig. 7: 4–10, 4–14) are somewhat less Fe-rich than the randomly oriented lizardite–1*T* mesh-centres (4–12, 4–15), although one reversal was noted (4–11, 4–13), but the lizardite–1*T* in this centre is Al-rich (Table 4). The lizardite–1*T* compositions of both the mesh rims and centres are grouped more tightly than the lizardites from earlier-stage serpentinization on Figure 7 and are slightly or significantly less Fe-rich than the olivine compositions of Fo_{90} determined by Hess & Otalora (1964). Some very fine grains of magnetite and Fe-rich sulfides (Lapham 1964) occur dispersed through the lizardite, but most of the magnetite occurs as irregular lenses of coarser anhedral grains in the mesh centres.

The most advanced stage of a thoroughly developed lizardite mesh-texture is represented by 18491 (Table 1, Fig. 5d). The Fe content of all textural units is very low (Table 2). The central parting of the mesh rim contains the least Fe (Fig. 6: 2–16) and the lizardite–1*T* of the main part of the mesh rims contains slightly more (2–17). The lizardite–1*T* mesh-centres (2–19) have a similar Fe content to the mesh rims, but this lizardite also contains very fine spheres of a nickel–iron sulfide that increase slightly the apparent Fe content. A band of grey lizardite–1*T* at the edge of the mesh centre is relatively clear of these spheres and has an Fe content intermediate between the central parting and the mesh rims (Fig. 6: 2–18). Magnetite is present as fine anhedral grains in the central parting and as irregular lenses at the former olivine grain-boundaries and in interstitial zones.

The most completely developed pseudomorphic textures after olivine are lizardite hourglass-textures (Table 2) represented by two samples, 18540 (WW, Fig. 1a) and AG67–67b (Fig. 5e). The Fe content of 18540 lizardite–1*T* is moderately high and the analyses plot just above the Mg_3–Fe^{3+}_2 composition line, which is high for lizardites (Fig. 6: 2–20). Only traces of magnetite are present in this sample. The lizardite–1*T* hourglass of sample AG67–67b has a low Fe content (Fig. 6: 2–21) and contains minor secondary magnetite as discrete anhedral dispersed grains along what were the fractures in the original olivine.

A striking feature of all lizardite mesh- and hourglass-textures is that although the host olivine contains no Al, minor amounts of Al are present in all lizardite formed after olivine (Tables 2, 4). The Al_2O_3 content is usually well under 1% but in a lizardite–1*T* mesh-centre in 18530 it reaches 4.1% (Table 4: 4–13).

Nickel and chlorine were specifically analyzed for in FW–L–4 and 18540. The olivine in FW–L–4 contains 0.36% NiO (Table 2: 2–1) and the lizardites after olivine have similar NiO values (Table 2: 2–2 to 2–4). The

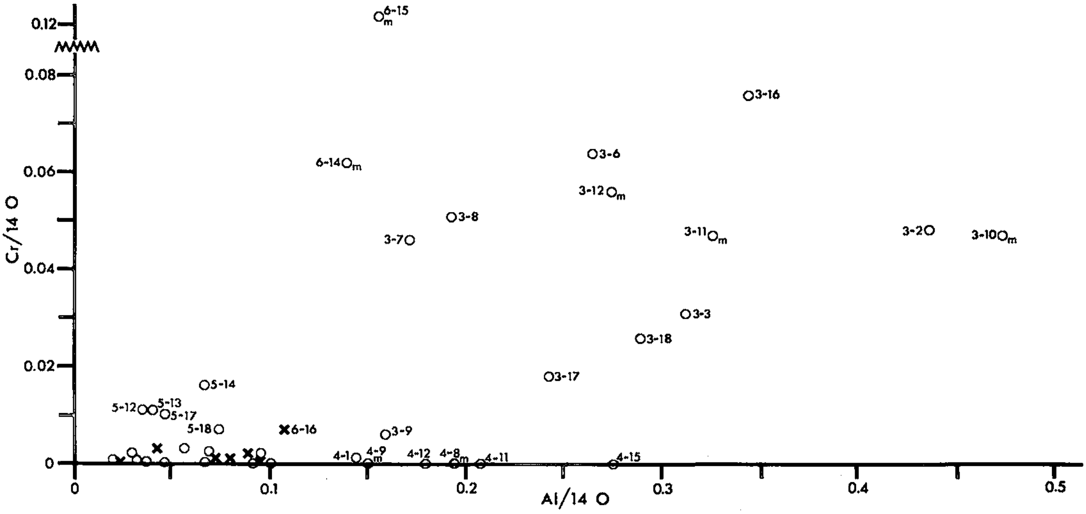

FIG. 8. Aluminum and chromium ions *per* formula unit for retrograde bastites, all of which are numbered, and for serpentines in mesh textures, hourglass textures and veins, most of which are not numbered as they cluster too closely along the abscissa. Point 3–5 is not numbered but it occurs in the cluster of points near 0.1 on the abscissa.

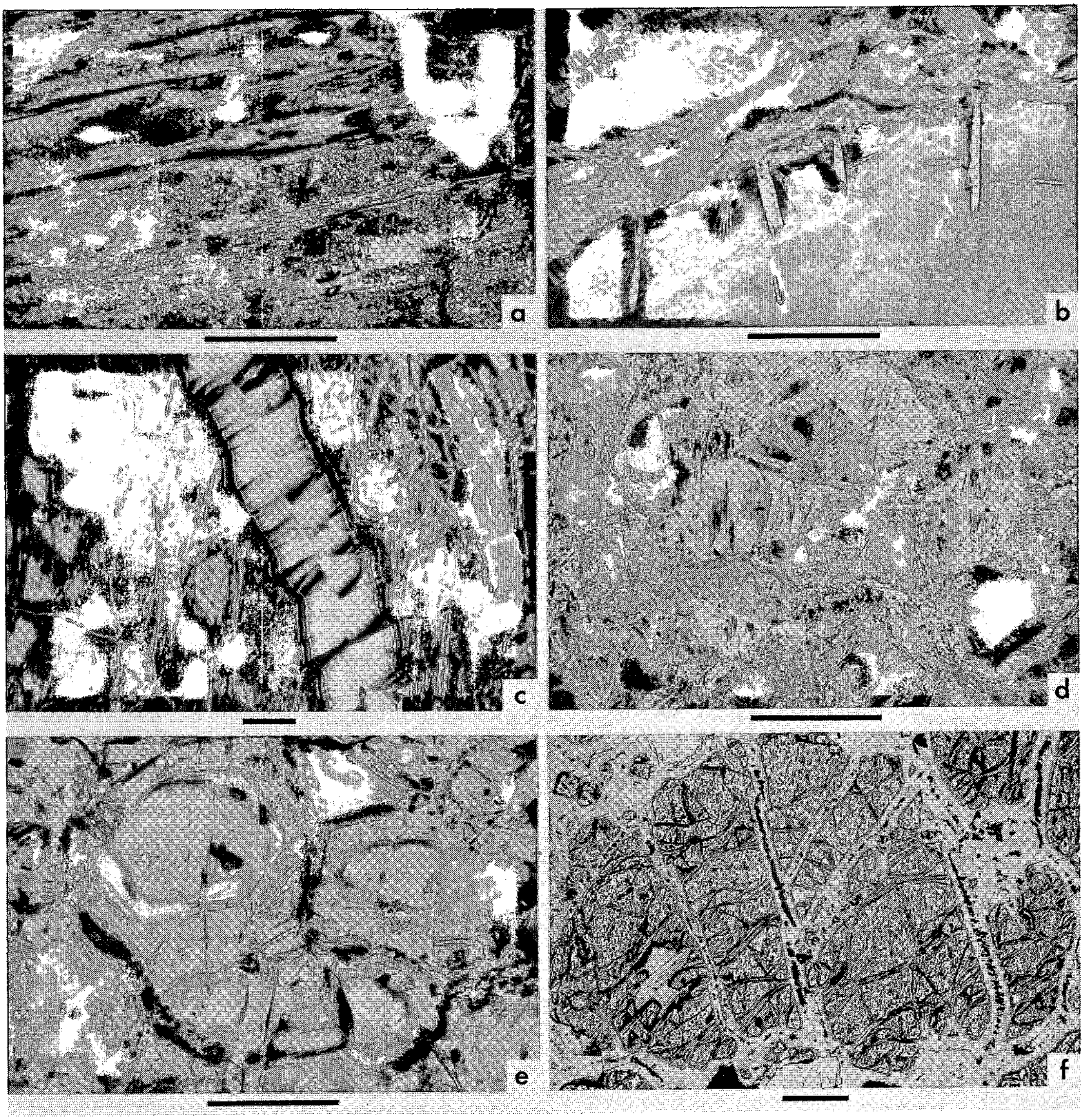

FIG. 9. (a) Enstatite bastites of multilayer lizardite (3–10 to 3–12), part veinlet and part bastite of lizardite–1*T* (3–9) in thin very dark grey zone running from right of centre to the left side. Sample 18530. Crossed nicols. (b) Enstatite bastite (in lower half) Povlen-type chrysotile–$2M_{c1}$ and $2Or_{c1}$ + minor Povlen-type parachrysotile (3–13, 3–14) partly replaced by antigorite blades (11–2 to 11–4); hourglass texture of lizardite–1*T* (2–20) in top-left corner, vein of chrysotile–$2M_{c1}$ cross-fibre asbestos (4–16) running diagonally from lower left to top-right side. Sample 18540. Partly crossed nicols. (c) Early vein of lizardite–1*T* (4–1) along right side, late vein of a multilayer lizardite (4–2, 4–3, 4–6) marginal zone and chrysotile–$2M_{c1}$ (4–4, 4–5, 4–7) central zone, enstatite bastite mostly to the left of multilayer-lizardite vein, composed of early lizardite–1*T* (3–7) (dark grey to black) and late lizardite–1*T* (3–8) (light grey polygons). Sample 18479. Crossed nicols. (d) Mesh rims (pale grey) of lizardite ± brucite (5–1, 5–2, 5–3), mesh centres (medium to dark grey) of lizardite + brucite (5–5), enstatite bastites (very pale grey areas in centre) composed of a thin lizardite–1*T* and minor 2*H* margin (5–12), an interior of lizardite–1*T* (5–13, 5–14) and a centre of lizardite + brucite (5–15, 5–16). Sample 18529, plane-polarized light. (e) Mesh rims of lizardite + brucite (5–7), concentrically zoned mesh-centres of lizardite (5–8). Sample 18508. Crossed nicols. (f) Mesh rims of lizardite–1*T* + minor chrysotile–$2M_{c1}$ ± brucite (6–2) with magnetite in central parting, later magnetite-free mesh-rims of lizardite–1*T* + brucite (6–3), mesh centres of olivine (6–1). Sample IB67–265, plane-polarized light. Bar represents 0.2 mm.

lizardite–1*T* after olivine in 18540 contains 0.31% NiO (Table 2: 2–20), although the Ni content of the original olivine is unknown. Similar small amounts of Ni were detected, but not analyzed for, in most of the other lizardites after olivine. Chlorine is present in amounts of up to 0.32% in lizardites after olivine in FW–L–4 (Table 2: 2–2 to 2–4). In the other samples, chlorine was found to be less common as the degree of serpentinization increased. Thus it was detected in half or more of the points analyzed in lizardite mesh-textures in 18479, 18480 and 18530 but very rarely in 18491; it is not present at all in the lizardite hourglass-textures in 18540 (Table 2) or AG67–67b.

Lizardite after pyroxene. The same stages of early, intermediate and fully developed serpentinization occur in pyroxenes, although these tend to serpentinize slightly less readily than olivine. The early stage is represented by FW–L–4 and 18480 (Table 3). In FW–L–4, lizardite–1*T* with slightly variable Fe content (similar to the variation in the lizardite after olivine, Fig. 6: 3–2, 3–3) has formed along cleavages in the enstatite (En_{87}), producing γ–serpentine apparent fibres (Fig. 5a). The enstatite (En_{84}) in sample 18480 (Fig. 5f) has two generations of lizardite–1*T*, an early-formed high-Fe γ-serpentine (Fig. 6: 3–5) and a later, very-high-Fe α-serpentine (3–6). Aluminum and chromium are high in the bastite of both samples (Fig. 8: 3–2, 3–3, 3–6) except for the lizardite adjacent to the fracture in the bastite in sample 18480; it seems to have lost both Al and Cr (3–5), plotting near 0.1 Al in Figure 8, within the group of non-bastite serpentines. No magnetite was produced in the bastites of either sample.

The diopside ($Ca_{44}Mg_{51}Fe_5$) in FW–L–4 (Table 3) is slightly serpentinized to a lizardite–1*T* with limited Fe variations (Fig. 6: 3–16, 3–17) along fractures and cleavages, but is also extensively altered to a dusty-brown material (Fig. 5a). The Al and Cr contents are variable but higher than in the lizardite after olivine (Fig. 8: 3–16, 3–17). The dusty-brown material has a variable composition, and in terms of Fe, plots along a line joining the diopside and lizardite compositions, suggesting that the brown material is a mixture of very fine diopside and lizardite. This is a different style of serpentinization from the advancing-front type found in orthopyroxenes. No magnetite is produced in any of the diopside serpentinization or alteration.

The intermediate stage of serpentinization is represented by bastites in 18479 and 18530 (Table 3). In 18479 (Fig. 9c), two generations of lizardite–1*T* have developed, an early Fe-rich α-serpentine along fractures and cleavages in the enstatite (Fig. 6: 3–7) and a late, slightly more Fe-rich γ-serpentine in the centres of the fracture fragments (3–8). The Al and Cr contents of these bastites (Fig. 8: 3–7, 3–8) are slightly lower than the early-stage bastites (3–6) and they have no secondary magnetite. The serpentinization history of the bastites after enstatite in 18530 (Table 3) is more complex (Fig. 9a). The earliest serpentine formed is colorless lizardite–1*T* that follows along and between enstatite cleavages and is in part after enstatite and in part vein material (Table 3: 3–9). It has the lowest Fe values of the results plotted (Fig. 6: 3–9) and low Al and particularly Cr contents (Fig. 8: 3–9). Later, colorless, variable-Fe, multilayer lizardites were developed (Fig. 6: 3–10, 3–11) and finally a pale green multilayer lizardite with irregular clusters of very fine grains of an unidentified Fe-, Ni-, Co- and S-bearing mineral noted earlier by Lapham (1964). Broad-beam analyses of this intimately mixed green multilayer lizardite and very fine-grained sulfides plot at very similar Fe (Fig. 6: 3–12) and Cr contents and a lower Al content (Fig. 8: 3–12) than the enclosing multilayer lizardite (3–10, 3–11).

Sample 18530 also contains lizardite–1*T* after diopside, with no secondary magnetite or sulfides. The Fe content of this lizardite is similar to the more Fe-rich multilayer lizardites after enstatite (Fig. 6: 3–18); the Al is generally similar but the Cr is lower (Fig. 8: 3–18).

The most advanced stage of this type of serpentinization is represented by the bastites after enstatite (Fig. 9b; WW, Fig. 2b) in specimen 18540 (Table 3). In contrast to the bastites described above, these are composed either of Povlen-type chrysotile–$2M_{c1}$ with minor Povlen-type parachrysotile, or of Povlen-type chrysotile–$2Or_{c1}$. However, the intensities of the two halves of the diffraction patterns, across the trace of the fibre axis, are not identical, indicating that the chrysotile does not have a completely developed cylindrical structure. The broadening of, and streaking between, 20*l* reflections suggest a certain amount of stacking disorder. In the earlier study (Wicks & Whittaker 1977), these were identified as lizardite bastites but detailed study of several more bastites clearly revealed their incomplete cylindrical Povlen-type chrysotile structure. The intensity of the 20*l* reflections is very sensitive to the position of the microbeam relative to the sample and this makes it difficult to estimate the relative intensities of 202, 203 and 204 reflections, so that $2Or_{c1}$ and $2H$ types of stacking could not be distinguished. Thus the identification of chrysotile–$2Or_{c1}$ is based on its association with chrysotile–$2M_{c1}$.

The Fe content of the chrysotile bastites is high, the highest of the chrysotiles studied, and the analyses plot above the Mg–Fe^{3+}_2 composition line in the area usually occupied by antigorites (Fig. 6: 3–13, 3–14). The Cr and particularly the Al contents are low compared with other bastites (compare Fig. 13: 3–13, 3–14 with Fig. 8).

Nickel and chlorine were specifically sought in the bastites in FW–L–4 and 18540 (Table 3). In FW–L–4 the pyroxenes and associated bastites have similar Ni contents. Diopside has the least Ni and enstatite is intermediate compared with the olivine. The Ni in the chrysotile bastites of 18540 (Table 3) approaches the Ni contents of the associated lizardite hourglass (Table 2). Up to 0.31% chlorine is present in both types of lizardite bastites in FW–L–4 but is absent in the chrysotile bastites in 18540. In other samples monitored for Cl, its presence is variable but generally it decreases with degree of serpentinization. Chlorine was detected in most of the points analyzed in the diopside bastite in 18530, half the points in the enstatite bastite in 18480, only the occasional point in lizardite–$1T$ enstatite bastites in 18530 and not at all in the multilayer lizardites of the enstatite bastites in 18530.

Lizardite + chrysotile veins. Veins were encountered in the intermediate-stage samples, 18479 and 18530. An early-banded lizardite–$1T$ vein filled fractures in sample 18479 and was succeeded by a complex vein which in part followed the earlier vein and in part, new

TABLE 5. RETROGRADE TYPE-3 LIZARDITE + BRUCITE AFTER OLIVINE AND OTHER SILICATES

Sample No.	18529					18508			
Analysis No.	1	2	3	4	5	6	7	8	9
Pts. Analyzed	2	2	2	2	2	1	2	11	2
SiO_2	39.1	40.0	36.4	38.5	10.5	42.0	34.1	38.0	11.5
TiO_2	0.0	0.0	0.0	0.02	0.0	0.03	0.03	0.0	0.03
Al_2O_3	0.16	0.16	0.22	0.15	0.38	0.33	0.24	0.39	0.49
Cr_2O_3	0.0	0.0	0.0	0.0	0.0	0.0	0.0	0.0	0.06
FeO^*	3.9	5.4	6.3	5.2	16.9	6.1	7.2	5.5	20.2
MnO	0.03	0.0	0.03	0.06	0.33	0.04	0.06	0.04	0.64
MgO	44.0	42.3	40.5	40.4	48.6	41.9	41.8	39.6	42.23
CaO	0.0	0.03	0.09	0.05	0.20	0.02	0.08	0.12	0.49
Total	87.19	87.89	83.54	84.38	76.91	90.42	83.51	83.65	75.64

Sample No.	AG67-70a		18529					18508			
Analysis No.	10	11	12	13	14	15	16	17	18	19	20
Pts. Analyzed	11	1	2	3	2	3	1	2	2	2	2
SiO_2	40.1	1.4	39.2	38.5	39.2	38.4	12.0	39.6	39.1	39.8	38.9
TiO_2	0.0	0.0	0.0	0.0	0.0	0.0	0.09	0.0	0.05	0.0	0.03
Al_2O_3	0.28	0.22	0.30	0.34	0.58	0.33	0.44	0.40	0.63	0.41	0.30
Cr_2O_3	0.05	0.04	0.13	0.14	0.21	0.21	0.28	0.12	0.09	0.06	0.04
FeO^*	2.7	2.6	4.1	4.3	6.80	5.9	16.9	4.0	8.1	4.4	6.5
MnO	0.02	0.42	0.06	0.02	0.03	0.04	0.34	0.0	0.11	0.04	0.12
MgO	42.2	75.3	40.4	39.5	40.5	40.6	47.9	40.1	37.6	40.1	39.2
CaO	0.0	0.0	0.05	0.44	0.22	0.04	0.33	0.0	0.03	0.0	0.06
Total	85.35	79.98	84.24	83.24	87.54	85.52	78.28	84.22	85.71	84.81	85.15

Analysis Nos. 1, 3, and 7, lizardite-$1T$ + brucite mesh rims; 2, lizardite-$1T$ mesh rim; 6, lizardite-$1T$ central parting; 4 and 8, lizardite-$1T$ mesh centres; 5 and 9, lizardite-$1T$ + brucite mesh centres; 10, lizardite-$1T$ hourglass textures; 11, individual brucite grain associated with magnetite and lizardite-$1T$ hourglass textures; 12, 13, 14, 15, and 16, orthopyroxene-bastite composed of lizardite-$1T$ and minor $2H$ marginal zone (12), lizardite-$1T$ colorless interior (13), lizardite-$1T$ pale brown interior (14), lizardite-$1T$ + brucite red-brown central zone (15), and brucite + lizardite-$1T$ central zone (16); 17 and 18, lizardite-$1T$ amphibole-bastite; 19 and 20, lizardite-$1T$ talc-bastite.

*Total iron calculated as FeO.

fractures (Fig. 9c; WW, Fig. 7a). The lizardite–1*T* of the earlier vein (Table 4, Fig. 7: 4–1) is of a somewhat similar, but slightly Fe-poor composition, compared to the host lizardite-1*T* mesh textures (Table 2, Fig. 7: 2–12 to 2–15) and lizardite–1*T* bastites (Table 3, Fig. 6: 3–7, 3–8). The complex vein is composed of a continuous marginal zone of multilayer lizardite of variable Fe and high Al contents (Table 4, Fig. 7: 4–2, 4–3, 4–6) and a central zone of chrysotile–$2M_{c1}$ of a lower and less variable Fe content and very much lower Al content (4–4, 4–5, 4–7). Aside from the Al content, the high Mn content of the multilayer lizardite marginal zone is the only other noteworthy feature (Table 4: 4–2, 4–3, 4–6). There is no magnetite associated with either vein and no reaction between the veins and the host serpentines.

Sample 18530 contains multilayer-lizardite veins, with traces of magnetite, that are associated with recrystallization of the host lizardite–1*T* (Fig. 5c; WW, Fig. 6a). These multilayer lizardites have a moderately high Fe content (Table 4) and the analyses (Fig. 7: 4–8, 4–9) plot near the multilayer-lizardite bastites (Fig. 6: 3–10, 3–11, 3–12). The Al content of the multilayer lizardite in the veins is lower than the bastistes (Tables 3, 4, Fig. 2). Some mesh centres near the multilayer veins have been recrystallized to multilayer lizardite + minor magnetite (Fig. 5c) of the same composition as the vein lizardite (4–9) but some high-Al mesh-centres, still composed of lizardite–1*T* (4–13), have not recrystallized.

In the most advanced stage of type-3 serpentinization, fine chrysotile-asbestos cross-fibre veins were analyzed in samples 18540 and AG67–67b (Table 4). The chrysotile–$2M_{c1}$ in 18540 has a composition similar to (Fig. 6: 4–16), although slightly more Fe-rich than, the host lizardite–1*T* hourglass-texture (2–20) including the anomalous plot above the Mg_3–Fe^{3+}_2 composition line in the area generally occupied by antigorites. In sample AG67–67b the chrysotile–$2M_{c1}$ and minor $2Or_{c1}$ has a similar composition but slightly lower Fe content than the host lizardite–1*T* hourglass-textures (Fig. 6: 4–17). Magnetite and Cl are absent from both veins. The relationship of these veins to the antigorite (11–1 to 11–4) is discussed in type 7.

Lizardite + brucite. The lizardite + brucite ± magnetite retrograde assemblage is represented by mesh textures in samples 18529 and 18508 and hourglass textures in AG67–70a (Table 5). In sample 18529, increasing brucite-content can be identified by an increase in intensity of color, from colorless through pale brown to reddish-brown (Fig. 9d; WW, Fig. 1b). Mesh rims have less brucite than mesh centres but the distribution is variable and content very minor; fine grains of magnetite occur at the centres and edges of the mesh rims. The colorless zones of the mesh rims are composed of pure, moderately Fe-rich lizardite–1*T* that plots near the Mg_3–Mg_2Fe^{3+} composition line (Fig. 7: 5–2). The pale brown zones are composed of mixtures of lizardite + brucite that plot away from the composition line towards the MgO–FeO baseline (Fig. 7: 5–1, 5–3). The mesh centres are concentrically arranged zones of pale grey, moderately Fe-rich lizardite–1*T* (Fig. 7: 5–4) and reddish-brown brucite + minor lizardite–1*T* (Fig. 7: 5–5). The Fe content of all the lizardite is slightly less than the parent olivine, Fo_{90} (Hess & Otalora 1964). A rough estimation of the Fe content of the brucite can be made by projecting from the lizardite points through the brucite + lizardite mixtures to the MgO–FeO baseline. This suggests an FeO value of between 15 and 30%, where the value is defined as (FeO/MgO + FeO) x 100. The brucite in the mesh rims has the lower Fe content. Chlorine was detected in some mesh rims and mesh centres.

The lizardite + brucite textures of sample 18508 (Fig. 9e; WWZ, Figs. 1b, 2a) have brucite in the mesh rims and not in most mesh centres. The central partings of mesh rims are composed of colorless, moderately Fe-rich lizardite–1*T* ± brucite (Fig. 7: 5–6 and associated point), and the mesh rims are composed of pale green, moderately Fe-rich lizardite–1*T* + brucite, with a variable, submicroscopic brucite content (Fig. 7: 5–7 and associated points). The mesh centres are commonly composed of grey lizardite–1*T* surrounding colorless lizardite–1*T*, but there is no measurable compositional difference between the two (Fig. 7: 5–8). Less commonly, the mesh centres are composed of brucite + minor lizardite–1*T* occasionally with very minor pyroaurite (Table 5: 5–9). There is no magnetite associated with the lizardite or brucite. Estimates of the FeO values of the brucites are between 15 and 30%. Chlorine was detected occasionally in mesh centres.

Sample AG67–70a is composed of lizardite–1*T* + brucite hourglass-textures. The lizardite occasionally contains minor submicroscopic brucite (Fig. 7: 5–10 and associated point), but in contrast with the mesh textures examined, where brucite is not visible unless it has a reddish-brown stain, most of the brucite in AG67–70a is clearly visible as fine anhedral grains with fine anhedral magnetite at sites of former olivine grain-boundaries and fractures. The Fe content of the brucite is low (Table 5: 5–11). Chlorine was not detected. Minor Al is consistently present in all three lizardite + brucite mesh- and hourglass-textures (Table 5), and Mn is preferentially concentrated in brucites (Table 5: 5–5, 5–9, 5–11, 5–16).

Crudely zoned lizardite + brucite bastites after orthopyroxene, or possibly clinopyroxene (Fig. 9d), are present in 18529 (Table 5). A narrow zone of colorless lizardite–1*T* and minor 2*H* (Fig. 7: 5–12) followed by a wider zone of colorless lizardite–1*T* (5–13), both relatively Mg-rich, form the margin. A pale brown zone of lizardite–1*T* (5–14), followed by a central reddish-brown zone of lizardite–1*T* + brucite (5–15) and brucite ± lizardite–1*T* (5–16), all relatively Fe-rich, form the central zone. The estimated FeO values of the brucite are between 30 and 35%. The Al and Cr contents of these bastites (Fig. 8: 5–12, 5–13, 5–14) are low relative to other bastites, but higher than the associated mesh-textures. Again Mn is concentrated in the brucite, and Cl was detected in several points analyzed.

Amphibole bastites (WW, Fig. 4b) composed of lizardite–1*T* with variable Fe (Fig. 7: 5–17, 5–18 and associated points) are present in sample 18508. The Al and Cr contents of these bastites are low relative to pyroxene bastites

TABLE 6. RETROGRADE TYPE-3 CHRYSOTILE + LIZARDITE

Sample No.	IB67-265			W70-72			AG67-64a		
Analysis No.	1	2	3	4	5	6	7	8	9
Pts. Analyzed	4	5	2	8	10	8	2	9	2
SiO_2	39.9	42.9	32.8	43.1	42.8	42.9	41.5	42.3	41.5
TiO_2	0.0	0.02	0.0	0.0	0.02	0.0	0.0	0.0	0.0
Al_2O_3	0.0	0.21	0.20	0.33	0.30	0.33	0.65	0.85	0.29
Cr_2O_3	0.0	0.02	0.0	0.02	0.02	0.02	0.02	0.02	0.0
FeO^*	13.6	2.1	8.8	3.4	3.4	2.4	3.3	2.7	2.7
MnO	0.19	0.07	0.17	0.06	0.03	0.02	0.09	0.15	0.04
MgO	45.7	43.4	38.2	41.1	41.3	42.1	41.0	40.0	42.5
CaO	0.06	0.0	0.04	0.0	0.0	0.02	0.0	0.0	0.0
Na_2O	0.0	0.0	0.0	0.0	0.0	0.0	0.0	0.0	0.0
K_2O	0.0	0.0	0.0	0.0	0.0	0.0	0.0	0.0	0.0
Total	99.45	88.72	80.21	88.01	87.87	87.79	86.56	86.02	87.03

Sample No.	AG67-64a								
Analysis No.	10	11	12	13	14	15	16	17	18
Pts. Analyzed	3	2	2	5	4	3	5	5	5
SiO_2	41.1	42.1	40.9	53.4	40.8	39.9	42.3	41.5	41.2
TiO_2	0.04	0.0	0.04	0.04	0.02	0.03	0.0	0.0	0.0
Al_2O_3	0.50	0.91	0.61	1.9	1.2	1.4	0.96	0.79	0.60
Cr_2O_3	0.04	0.0	0.02	0.97	0.82	1.6	0.09	0.02	0.0
FeO^*	3.5	3.3	3.7	2.4	3.2	3.6	2.4	3.0	3.8
MnO	0.08	0.06	0.07	0.04	0.16	0.09	0.11	0.06	0.12
MgO	40.9	40.2	41.1	17.8	39.7	40.3	40.6	40.7	40.7
CaO	0.0	0.0	0.0	23.2	0.03	0.09	0.0	0.0	0.0
Na_2O	0.0	0.0	0.0	0.29	0.0	0.0	0.0	0.0	0.0
K_2O	0.0	0.0	0.0	0.03	0.0	0.0	0.0	0.0	0.0
Total	86.16	86.57	86.44	100.07	85.93	87.01	86.46	86.07	86.42

Analysis No. 1, olivine (Fo_{86}); 2, lizardite-1*T* and very minor chrysotile-$2M_{c1}$ mesh rims; 3, lizardite-1*T* + brucite mesh rims; 4, weakly Povlen-type chrysotile-$2M_{c1}$ mesh rims; 5, lizardite-1*T* mesh centres; 6, chrysotile-$2M_{c1}$ slip veins; 7, chrysotile-$2M_{c1}$ central parting; 8, chrysotile-$2M_{c1}$ mesh rims; 9 and 10, lizardite-1*T* mesh rims; 11 and 12, lizardite-1*T* mesh centres; 13, clinopyroxene ($Ca_{46}Mg_{50}Fe_4$); 14 and 15, multi-layer lizardite after clinopyroxene; 16, chrysotile-$2M_{c1}$ and $2Or_{c1}$ cross-fibre asbestos vein; 17, chrysotile-$2Or_{c1}$ slip veins; 18, lizardite-1*T* and 2*H* veins.

*Total iron calculated as FeO.

(Fig. 8: 5–17, 5–18). Chlorine was detected in a few points. Talc bastites composed of lizardite–1*T* with a slightly more restricted Fe range (Fig. 7: 5–19, 5–20) are also present in 18508. The Cr content is only slightly above associated mesh-textures; no Cl was detected.

Chrysotile + lizardite ± brucite. The retrograde lizardite + chrysotile + brucite stage of type-3 serpentinization is represented by sample IB67–265 (Table 6). Grain boundaries and major fractures in olivine (Fo_{86}) have been altered to γ–serpentine composed of lizardite ± minor Povlen-type chrysotile–$2M_{c1}$ ± minor brucite (Fig. 9f). The Fe content of this mixture is low (Table 6, Fig. 10: 6–2) and lenses and stringers of magnetite occupy the centres of the mesh rims. The secondary fractures are the sites of narrow mesh-rims of green Fe-rich lizardite–1*T* + brucite (Table 6, Fig. 10: 6–3) with no magnetite. Minor Al is present in both types of serpentine in spite of its absence in the olivine. The Mn found in the olivine is retained in the green Fe-rich lizardite + brucite mixture but lost in the Fe- and brucite-poor lizardite (Table 6). Chlorine was detected in only one of seven points analyzed.

The brucite-absent assemblage is represented by samples W70–72 and AG67–64a. Sample W70–72 is composed of γ–serpentine mesh-rims of Povlen-type chrysotile–$2M_{c1}$ and α–serpentine mesh-centres of lizardite–1*T* hourglass. Both mesh rims and centres have similar compositions (Table 6, Fig. 10: 6–4, 6–5) but the associated chrysotile–$2M_{c1}$ slip-veins have a lower Fe-content (6–6). Magnetite is a minor component occurring in fine isolated anhedral grains. Chlorine was not detected.

The mesh textures of sample AG67–64a are composed of compound mesh-rims, made up of a chrysotile–$2M_{c1}$ filled central parting (6–7), a chrysotile–$2M_{c1}$ zone (6–8) followed by a lizardite–1*T* zone (6–9, 6–10) surrounding mesh-centres (6–11, 6–12) of lizardite–1*T* hourglass-configurations (Fig. 11a; WWZ, Fig. 1d). Magnetite is abundant as lenses along mesh rims, and as lenses and grains in mesh centres. The Fe contents of these phases are variable but fairly closely grouped (Table 6) but in Figure 10 they plot from the Mg_3–Mg_2Fe^{3+} composition line up to above the Mg_3–Fe^{3+}_2 composition line in the zone usually occupied by antigorite. Sample AG67–64a also contains diopside ($Ca_{46}Mg_{50}Fe_4$) partly altered to multilayer lizardite of slightly variable composition (Table 6, Fig. 10: 6–14, 6–15). Cross-fibre-asbestos veins (Fig. 11a) composed of chrysotile–$2M_{c1}$ and $2Or_{c1}$ (Table 6: 6–16) cut all pseudomorphic textures, but are themselves cut and disrupted by slip-veins of chrysotile–$2Or_{c1}$ (6–17) and by fracture-filling veins of well-crystallized lizardite–1*T* and 2*H* (6–18). The

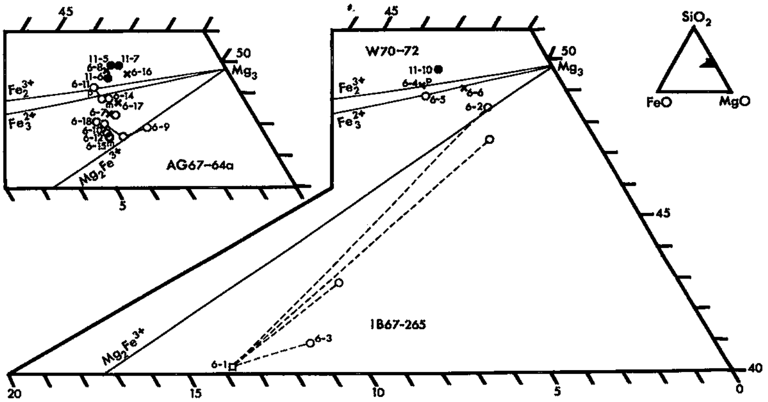

FIG. 10. MgO–FeO–SiO_2 diagrams for types 3 and 5. IB67–265: 6–1 olivine Fo_{86}, 6–2 and associated point, lizardite–1*T* + minor chrysotile–$2M_{c1}$ ± brucite mesh-rims, 6–3 and associated point, lizardite–1*T* + brucite mesh-rims. W70–72: 6–4 weakly Povlen-type-chrysotile–$2M_{c1}$ mesh-rims, 6–5 lizardite–1*T* mesh-centres, 6–6 chrysotile slip-veins, 11–10 antigorite blades. AG67–64a: 6–7 chrysotile–$2M_{c1}$ central partings, 6–8 chrysotile–$2M_{c1}$ mesh-rims, 6–9, 6–10 and associated point, lizardite–1*T* mesh-rims, 6–11, 6–12 and associated point, lizardite–1*T* mesh-centres, 6–14, 6–15 multilayer lizardite after diopside, 6–16 chrysotile–$2M_{c1}$ and $2Or_{c1}$ cross-fibre-asbestos veins, 6–17 chrysotile-$2Or_{c1}$ slip-veins, 6–18 lizardite–1*T* and 2*H* veins.

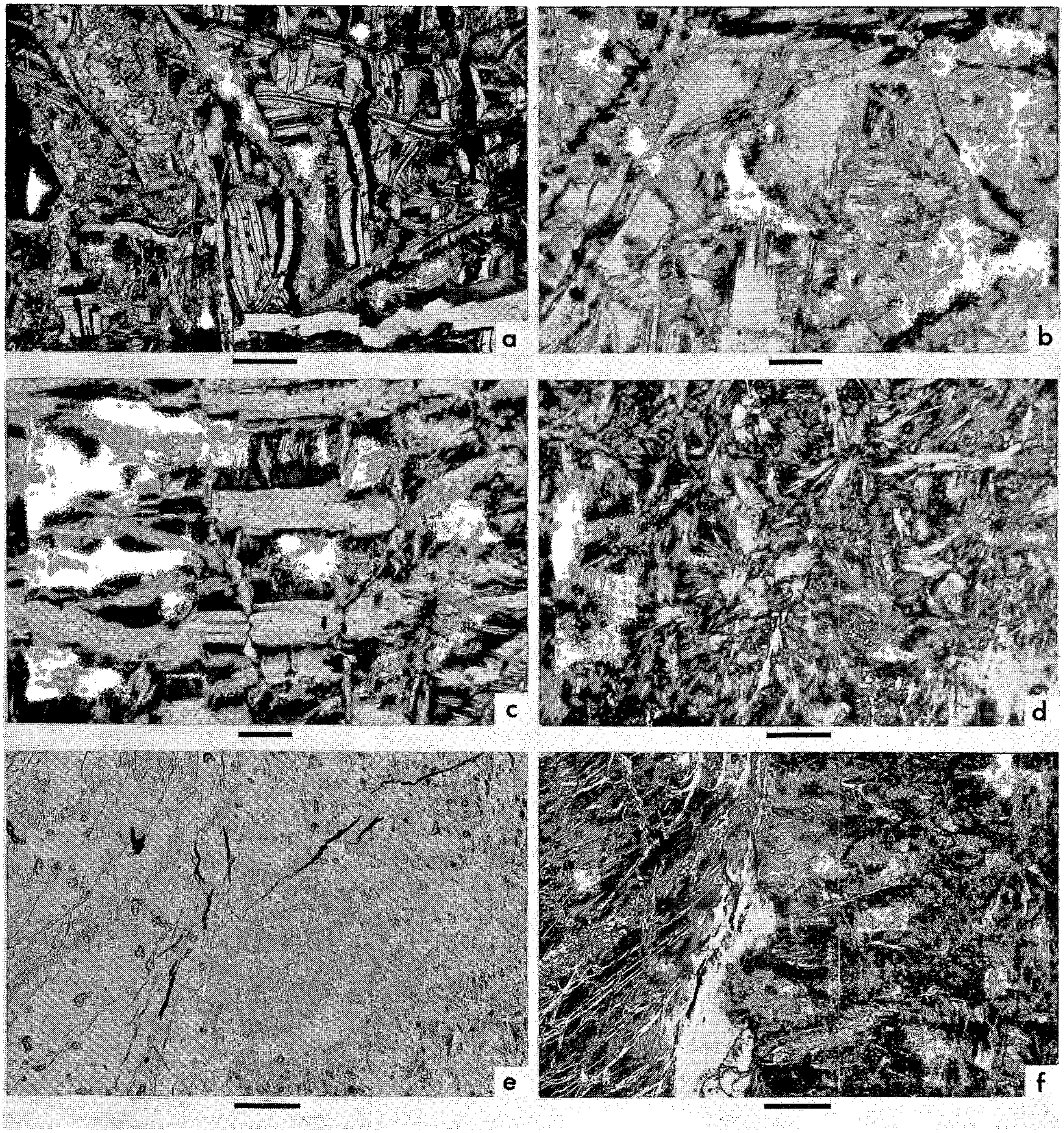

FIG. 11. (a) Central parting of chrysotile–2M_{c1} (6–7), compound mesh-rims of chrysotile–2M_{c1} (6–8) and lizardite–1T (6–9, 6–10), mesh centres of lizardite–1T (6–11, 6–12), early vein of chrysotile–2M_{c1} and 2Or_{c1} (6–16) cross-fibre asbestos (bottom right) disrupted by chrysotile–2Or_{c1} (6–17) slip-veins, late veins of lizardite–1T and 2H blades (6–18) on the left side intruded by even later veins of antigorite blades (11–6, 11–7). Sample AG67–64a. Crossed nicols. (b) Relict mesh-rims of lizardite–1T (7–2) in the top-left quadrant, mesh centres of Povlen-type chrysotile–2M_{c1} and 2Or_{c1} (7–2). Sample 18538. Crossed nicols. (c) Mesh rims of Povlen-type chrysotile–2M_{c1} (7–5), mesh centres of Povlen-type chrysotile–2M_{c1} + lizardite–1T (7–6). Sample 18501. Crossed nicols. (d) Interpenetrating texture of lizardite–1T blades (7–7). Sample 18559. Crossed nicols. (e) Engulfed lens on left, chrysotile–2M_{c1} and 2Or_{c1} with brown staining (8–12) and without staining (8–7 to 8–11) on right. Sample W70–74, plane-polarized light. (f) Same as (e) engulfed lens with mesh rims of chrysotile–2M_{c1} (8–1), mesh centres of lizardite–1T (8–2, 8–3), slip veins of Povlen-type chrysotile–2M_{c1} (8–4) disrupting mesh rims, antigorite blades (8–5) in zone from middle left side up toward top edge, foliated chrysotile–2M_{c1} and 2Or_{c1} at edge of lens (8–6). Sample W70–74. Crossed nicols. Bar represents 0.2 mm.

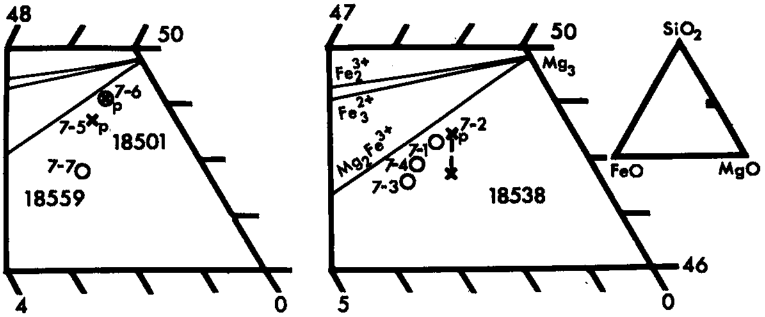

FIG. 12. MgO–FeO–SiO_2 diagrams for type 5. 18538: 7–1 lizardite–1*T* mesh-rims, 7–2 Povlen-type chrysotile–$2M_{c1}$ and $2Or_{c1}$ fibres in mesh centres and associated point of chrysotile + minor brucite, 7–3 lizardite–1*T* + traces of iowaite in marginal zone of bastite, 7–4 lizardite–1*T* interior zone of bastite. 18501: 7–5 Povlen-type chrysotile–$2M_{c1}$ mesh-rims, 7–6 Povlen-type chrysotile–$2M_{c1}$ + lizardite–1*T* mesh-centres. 18559: 7–7 lizardite–1*T* blades.

latter veins sometimes follow the slip zones, but also occur in fine gnash fractures without the slip serpentine. There is an increase in Fe with each successive set of veins (Table 6, Fig. 10), and a slight decrease in Al.

The Al contents of all serpentine phases after olivine in AG67–64a are higher than other chrysotile + lizardite retrograde mesh-textures (compare AG67–64a with IB67–265 and W70–72, Table 6). The Al and, particularly, the Cr contents of the multilayer lizardites (Fig. 8: 6–14, 6–15) are the highest, reflecting their pyroxene parentage. Chromium is low in all other phases except for the chrysotile cross-fibre-asbestos veins where they traverse the diopside bastites (Table 6, Fig. 8: 6–16). The Al

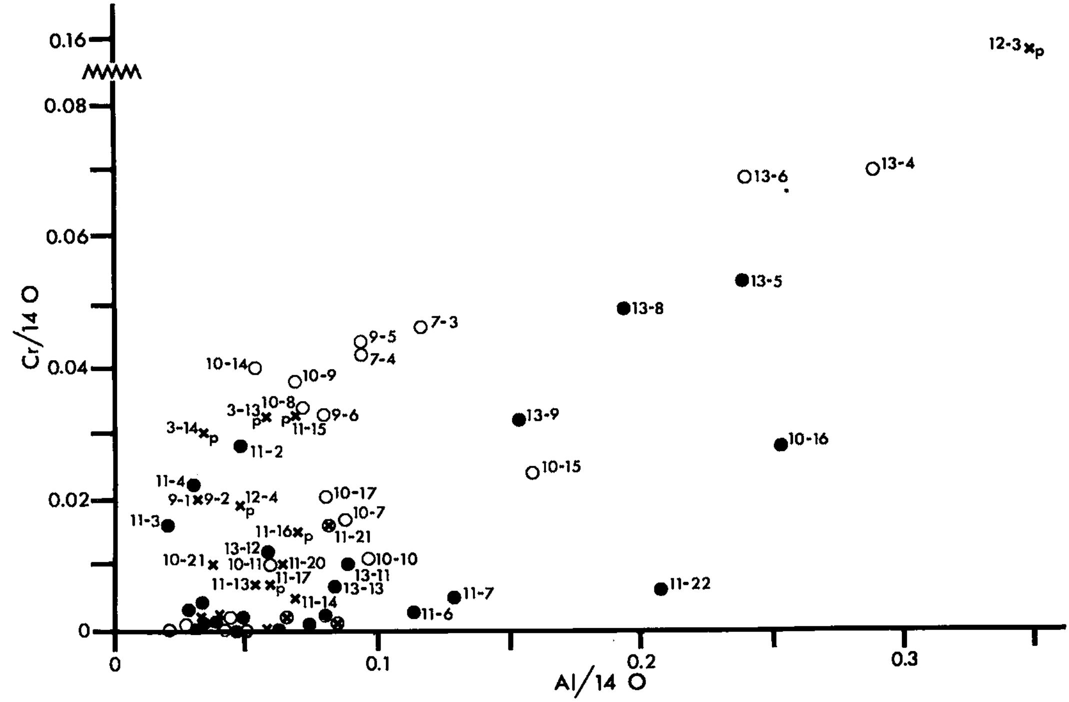

FIG. 13. Aluminum and chronium ions *per* formula unit for prograde bastites, all of which are numbered, and for associated rock- and vein-forming antigorite, chrysotile and lizardite, most of which are not numbered as they cluster too closely along the abscissa.

TABLE 7. PROGRADE TYPE-5 CHRYSOTILE ± LIZARDITE ± BRUCITE, OR LIZARDITE ± BRUCITE

Sample No.	18538				18501		18559
Analysis No.	1	2	3	4	5	6	7
Pts. Analyzed	5	12	3	8	4	8	11
SiO_2	41.0	40.9	39.4	39.9	41.3	42.3	40.3
Al_2O_3	0.33	0.45	1.0	0.82	0.38	0.36	0.45
Cr_2O_3	0.0	0.0	0.60	0.56	0.0	0.05	0.0
FeO^*	1.9	1.6	2.5	2.2	1.1	0.81	1.6
MnO	0.0	0.0	0.10	0.08	0.0	0.0	0.07
MgO	42.0	42.0	40.8	41.1	42.4	43.1	42.4
CaO	0.0	0.0	0.0	0.0	0.0	0.0	0.0
Total	85.23	84.95	84.40	84.66	85.18	86.62	84.82

Analysis No. 1, lizardite-$1T$ mesh rims; 2, Povlen-type chrysotile-$2M_{c1}$ and $2Or_{c1}$ fibres in mesh centres; 3, lizardite-$1T$ + traces of iowaite(?) in marginal zone of bastite; 4, lizardite-$1T$ interior zone of bastite; 5, Povlen-type chrysotile-$2M_{c1}$ mesh rims; 6, Povlen-type chrysotile-$2M_{c1}$ and lizardite-$1T$ mesh centres; 7, lizardite-$1T$ blades.

*Total iron calculated as FeO.

content of this chrysotile is the second highest found in this study (Fig. 2: 6–16). The chrysotile–$2Or_{c1}$ from the slip veins is also high for chrysotile (Table 6: 6–17). Chlorine was not detected.

PROGRADE TEXTURES

Type 5: chrysotile ± lizardite ± brucite

Type-5 serpentinization begins in the early stages of a prograde event through the recrystallization of earlier formed lizardite pseudomorphic textures or through the serpentinization of relict primary minerals. The products of these processes are varied mineralogically, being composed of chrysotile or lizardite or both ± brucite ± magnetite. The textures formed are generally, but not always, nonpseudomorphic.

Chrysotile + brucite. The prograde chrysotile + brucite is represented by sample 18538 (Table 1) in which Povlen-type chrysotile–$2M_{c1}$ and $2Or_{c1}$ occur as serrate veins or hourglass configurations in mesh centres probably developed after relict olivine (Fig. 11b; WW, Figs. 1d, 8c). Occasionally, minor amounts of brucite and very minor amounts of iowaite (identified by microbeam camera and microprobe) are associated with the chysotile. Brucite is usually present in the chrysotile as discrete, easily recognized grains (WW, Fig. 1c) but may also be submicroscopic, causing the analysis to plot off the Mg_3–Mg_2Fe^{3+} composition line (Fig. 12). Relict retrograde lizardite–$1T$ mesh-rims, with traces of iowaite and with magnetite grains along the central parting and very fine grains dispersed through the lizardite, infrequently are

TABLE 8. PROGRADE TYPE-6 CHRYSOTILE ± LIZARDITE AFTER TYPES 3 AND 7

Sample No.	W70-74											
Analysis No.	1	2	3	4	5	6	7	8	9	10	11	12
Pts. Analyzed	2	3	7	4	6	4	7	3	3	2	2	4
SiO_2	42.3	42.3	42.2	42.4	43.5	41.7	42.5	42.5	42.6	42.5	42.8	41.7
Al_2O_3	0.25	0.27	0.26	0.28	0.27	0.24	0.27	0.27	0.28	0.27	0.29	0.17
Cr_2O_3	0.02	0.0	0.0	0.0	0.0	0.0	0.0	0.0	0.02	0.03	0.02	0.0
FeO^*	2.6	2.6	3.0	1.7	2.1	2.3	2.0	3.2	3.6	4.3	5.1	5.7
MnO	0.02	0.03	0.03	0.0	0.0	0.0	0.0	0.07	0.03	0.04	0.3	0.02
MgO	41.6	41.7	41.9	42.0	41.7	41.1	42.6	41.1	40.9	40.3	40.4	39.2
CaO	0.02	0.0	0.0	0.0	0.0	0.0	0.0	0.0	0.0	0.0	0.0	0.0
Total	86.81	86.90	87.39	86.38	87.57	85.34	87.37	87.14	87.43	87.44	88.91	86.79

Analysis No. 1, chrysotile-$2M_{c1}$ mesh rims; 2 and 3, lizardite-$1T$ mesh centres; 4, Povlen-type chrysotile-$2M_{c1}$ slip vein; 5, antigorite blades (all analyses 1 to 5 are within a lens of serpentinite engulfed in foliated chrysotile: analyses 6 to 12); 6, colorless, foliated chrysotile-$2M_{c1}$ and $2Or_{c1}$ at edge of lens; 7, 8, 9, 10, and 11, colorless, foliated chrysotile-$2M_{c1}$ with variable $2Or_{c1}$; 12, pale brown chrysotile-$2M_{c1}$ and $2Or_{c1}$.

*Total iron calculated as FeO.

replaced by the chrysotile. The compositions (Table 7) of the relict lizardite and prograde chrysotile are similar, although the lizardite is slightly Fe-rich owing to the fine magnetite inclusions (Fig. 11: 7–1, 7–2). No magnetite occurs in the chrysotile. Lizardite–1*T* bastites after enstatite occasionally contain minor iowaite in the marginal zone (WW, Fig. 2c). The lizardite bastites are uniform in composition (Table 7) and are slightly more Fe-rich, particularly in the marginal zone (Fig. 9: 7–3, 7–4), and more Al- and Cr-rich than the chrysotile mesh-centres and lizardite–1*T* mesh-rims (Fig. 13: 7–3, 7–4). Manganese is present in minor amounts only in the lizardite–1*T* bastites (Table 7). Chlorine was detected once in five lizardite mesh-rim points analyzed, and once in seven chrysotiles analyzed. However, minor Cl was generally detected in the lizardite bastites, particularly in the marginal zones. This presence of minor Cl suggests that the 8.1 Å accessory mineral sometimes detected with the microbeam camera is iowaite, not brugnatellite.

Chrysotile + lizardite. Sample 18501 (Table 7) is composed of mesh rims of parallel, weakly Povlen-type chrysotile–$2M_{c1}$ fibres with minor lenses of magnetite and mesh centres of randomly oriented Povlen-type chrysotile–$2M_{c1}$ + lizardite–1*T* (Fig. 11c; WWZ, Fig. 2c). The chrysotile rims are slightly more Fe-rich than the chrysotile + lizardite mesh-centres (Table 7) but both have very low Fe contents (Fig. 12: 7–5, 7–6). All other cations are low and Cl was not detected.

Lizardite. Sample 18559 is composed mainly of lizardite–1*T* blades in subparallel orientation, but also in random orientation in some limited areas (Fig. 11d). The reflections on the microbeam X-ray-diffraction patterns are slightly broadened and diffuse. The compositions of the foliated and random lizardite are identical, Fe-poor (Table 7), and plot below the Mg_3–Mg_2Fe^{3+} composition line (Fig. 12: 7–7). Aluminum is the only significant minor element. Chlorine was not detected.

Type 6: chrysotile ± lizardite ± brucite

Type-6 serpentinization is the sheared equivalent of type 5. Sample W70–74 (Table 8), representing this type, is composed of a lens-shaped fragment of massive serpentinite engulfed in, and being altered to, complexly sheared, foliated chrysotile–$2M_{c1}$ with lesser but variable amounts of chrysotile–$2Or_{c1}$ (Figs. 11e, 11f). The random orientation displayed in the diffraction patterns of this chrysotile makes it impossible to determine if the Povlen-type structure is present. The serpentine within the lens is made up of chrysotile mesh-rims surrounding lizardite–1*T* mesh-centres in the form of broad plates or hourglass configurations, all with moderate but slightly variable Fe contents (Fig. 14: 8–1, 8–2, 8–3). This is a retrograde type-3 assemblage. Cross- and slip-fibre veins of Povlen-type chrysotile-$2M_{c1}$ cut through the mesh texture. All these earlier forms of serpentine have been partly replaced along linear cross-cutting zones and in discrete individual sites by fine-grained, moderately Fe-rich antigorite, which

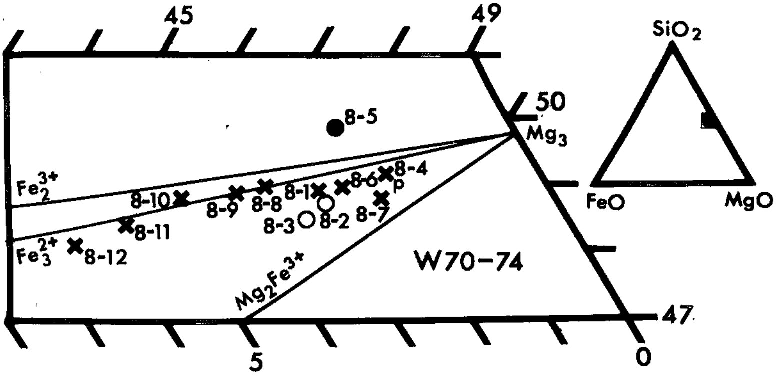

FIG. 14. MgO–FeO–SiO_2 diagram for type 6. W70–74: 8–1 chrysotile–$2M_{c1}$ mesh-rims, 8–2 and 8–3 lizardite–1*T* mesh-centres, 8–4 Povlen-type chrysotile–$2M_{c1}$ slip-vein, 8–5 antigorite blades (all analyses 1 to 5 are within a lens of serpentinite engulfed in foliated chrysotile: analyses 6 to 12), 8–6 colorless, foliated chrysotile–$2M_{c1}$ and $2Or_{c1}$ at edge of lens, 8–7, 8–8, 8–9, 8–10 and 8–11 colorless, foliated chrysotile–$2M_{c1}$ with variable $2Or_{c1}$, 8–12 pale brown chrysotile–$2M_{c1}$ and $2Or_{c1}$.

TABLE 9. PROGRADE TYPE-7 ANTIGORITE + BRUCITE

Sample No.	W75-62				W70-35			
Analysis No.	1	2	3	4	5	6	7	8
Pts. Analyzed	2	2	2	2	2	4	5	3
SiO_2	41.5	40.6	44.2	44.8	40.4	41.3	43.3	43.2
Al_2O_3	0.26	0.29	0.36	0.35	0.83	0.72	0.28	0.42
Cr_2O_3	0.26	0.27	0.02	0.0	0.59	0.45	0.0	0.0
FeO^*	1.0	1.1	0.90	1.4	2.0	1.0	1.0	1.2
MnO	0.0	0.04	0.0	0.04	0.04	0.02	0.0	0.03
MgO	42.2	41.9	43.4	43.1	42.1	42.9	42.5	42.4
CaO	0.0	0.0	0.0	0.0	0.0	0.0	0.0	0.0
Total	85.22	84.20	88.88	89.69	85.96	86.39	87.08	87.25

Sample No.	W70-35				W70-41a				
Analysis No.	9	10	11	12	13	14	15	16	17
Pts. Analyzed	2	4	3	2	8	10	3	7	3
SiO_2	42.0	40.9	41.0	39.6	44.3	44.3	42.7	40.5	0.57
Al_2O_3	0.60	0.71	0.53	0.51	0.13	0.15	0.28	0.24	0.27
Cr_2O_3	0.03	0.0	0.0	0.0	0.0	0.0	0.0	0.05	0.02
FeO^*	1.0	1.6	0.98	2.3	0.93	1.3	0.98	0.89	1.2
MnO	0.0	0.02	0.0	0.02	0.04	0.0	0.05	0.03	0.36
MgO	43.3	42.5	42.3	41.9	43.4	43.3	43.6	42.2	67.9
CaO	0.0	0.0	0.0	0.0	0.0	0.0	0.03	0.0	0.04
Total	86.93	85.73	84.81	84.33	88.80	89.05	87.64	83.91	70.36

Analysis Nos. 1 and 2, chrysotile-$2M_{c1}$ serrate vein; 3 and 4, antigorite blades; 5, lizardite-$1T$ in centre zones of bastites; 6, lizardite-$1T$ + chlorite in outer zones of bastites; 7 and 8, antigorite blades; 9, chrysotile-$2M_{c1}$ + lizardite-$1T$ margin of a recrystallization zone; 10, chrysotile-$2M_{c1}$ + lizardite-$1T$ central part of a recrystallization zone; 11, chrysotile-$2M_{c1}$ + minor parachrysotile marginal zone of a cross-fibre asbestos vein; 12, chrysotile-$2M_{c1}$ and $2Or_{c1}$ + brucite central zone of cross-fibre asbestos vein; 13 and 14, antigorite blades and grains; 15, chrysotile mesh rims; 16, Povlen-type chrysotile-$2M_{c1}$ + brucite in vein; 17, brucite in vein.

*Total iron calculated as FeO.

forms a prograde type-7 assemblage (8–5). Magnetite is rare but does occur as fine anhedral grains in the mesh texture. Minor relict, euhedral primary chromite is also present.

The lens of serpentinite, with its retrograde type-3 mesh-texture and prograde type-7 antigorite has been partly destroyed by shearing and has recrystallized to prograde, type-6 moderately well-foliated chrysotile–$2M_{c1}$ and $2Or_{c1}$ with a wide range of Fe contents (Table 8, Fig. 14: 8–6 to 8–12). This means that some of the original chrysotile, lizardite, antigorite, magnetite and chromite have been recrystallized to chrysotile. Irregular patches of pale-brown staining (Fig. 11e) in the foliated chrysotile give only chrysotile–$2M_{c1}$ and $2Or_{c1}$ diffraction patterns but are the most Fe-rich zones (Fig. 14: 8–12). Some unstained chrysotiles (8–11) have almost as high an Fe content and are among the most Fe-rich encountered in this study. No magnetite is present in the chrysotile except occasionally at the edges of the engulfed fragment. Slip veins of Povlen-type chrysotile–$2M_{c1}$ (8–4) traverse the fragment subparallel to the foliation and follow, disrupt and recrystallize earlier cross- and slip-fibre chrysotile veins and mesh-rims.

The minor-element content of all phases both within the fragment and in the foliated serpentine is low (Table 8). Aluminum occurs in small amounts fairly uniformly distributed through all phases. Chromium occurs in some of the foliated chrysotile (Table 8: 8–9, 8–10, 8–11) or chrysotile mesh-rims (8–1) modified by shearing, but not in the serpentines within the lens where the relict primary chromite occurs. Chlorine was not detected.

Type 7: antigorite ± brucite

Type-7 serpentinization occurs in the inter-

TABLE 10. PROGRADE TYPE-7 ANTIGORITE + BRUCITE AFTER OLIVINE AND PYROXENE

Sample No.	18544										
Analysis No.	1	2	3	4	5	6	7	8	9	10	11
Pts. Analyzed	6	5	3	2	1	10	2	4	2	2	4
SiO_2	41.2	41.8	40.8	42.0	1.2	57.0	42.2	39.9	40.0	41.6	41.4
TiO_2	0.0	0.0	0.0	0.0	0.05	0.0	0.0	0.0	0.0	0.0	0.0
Al_2O_3	0.0	0.19	0.17	0.30	0.32	1.3	0.78	0.62	0.61	0.86	0.54
Cr_2O_3	0.0	0.0	0.0	0.0	0.02	0.46	0.23	0.45	0.49	0.14	0.13
FeO^*	8.7	1.5	2.1	2.2	7.4	5.6	7.0	2.1	1.9	2.9	1.5
MnO	0.08	0.03	0.0	0.03	0.29	0.09	0.16	0.06	0.08	0.07	0.02
MgO	49.8	42.9	42.9	40.7	63.7	35.0	38.1	41.2	41.3	40.8	42.5
CaO	0.0	0.0	0.0	0.0	0.0	0.72	0.0	0.0	0.0	0.0	0.0
Total	99.78	86.42	85.97	85.23	72.98	100.17	88.47	84.33	84.38	86.37	86.09

Sample No.	W70-55									
Analysis No.	12	13	14	15	16	17	18	19	20	21
Pts. Analyzed	2	10	11	1	1	1	4	6	3	4
SiO_2	41.3	41.5	38.2	40.2	42.2	40.8	42.4	43.9	43.6	42.4
TiO_2	0.0	0.0	0.02	0.04	0.03	0.0	0.0	0.0	0.0	0.0
Al_2O_3	0.25	0.30	0.44	1.4	2.3	0.72	0.26	0.30	0.22	0.34
Cr_2O_3	0.0	0.0	0.50	0.31	0.38	0.27	0.02	0.02	0.0	0.13
FeO^*	1.9	1.4	1.6	4.4	3.3	2.5	1.5	2.4	2.7	1.4
MnO	0.02	0.02	0.07	0.06	0.04	0.05	0.03	0.04	0.03	0.0
MgO	43.3	42.8	40.3	39.5	39.0	42.0	43.6	42.3	41.5	44.0
CaO	0.0	0.0	0.0	0.0	0.0	0.0	0.0	0.0	0.0	0.0
Total	86.77	86.02	81.13	85.91	87.25	86.34	87.81	88.96	88.05	88.27

Analysis No. 1, olivine Fo_{91}; 2, lizardite-1*T* mesh rims; 3, lizardite-1*T* + brucite mesh centres; 4, antigorite grains; 5, brucite grain; 6, enstatite ($Ca_1Mg_{91}Fe_8$); 7, 8, 9, 10, and 11, lizardite-1*T* bastite after enstatite; 12, lizardite-1*T* mesh rims; 13, chrysotile-$2M_{c1}$ serrate veins and hourglass; 14, lizardite-1*T* bastites after enstatite; 15, lizardite-1*T* + chlorite blade after bastite; 16, antigorite + chlorite blade after bastite; 17, lizardite-1*T* + chlorite after bastite; 18, lizardite-1*T* bastites after amphibole; 19 and 20, antigorite blades; 21, chrysotile-$2M_{c1}$ cross-fibre asbestos veins.

*Total iron calculated as FeO.

mediate- and high-temperature ranges of prograde serpentinization, through the recrystallization of earlier retrograde lizardite + chrysotile ± brucite ± magnetite textures or through the serpentinization of relict olivines and pyroxenes to antigorite + brucite ± magnetite or antigorite ± magnetite nonpseudomorphic textures.

Antigorite + brucite. Five samples (W70–35, W70–41a and W75–62 in Table 9 and 18544 and W70–55 in Table 10) represent the antigorite + brucite, type-7 prograde assemblage. All but sample 18544 have formed at least in part after chrysotile + brucite, type-5 assemblages. In sample W75–62 (Figs. 15a, b), Fe-poor antigorite blades (Fig. 16: 9–3, 9–4) have formed through both pseudomorphic and nonpseudomorphic recrystallization of Fe-poor chrysotile–$2M_{c1}$ serrate veins (9–1, 9–2). In samples W70–35 (Fig. 15c) and W70–41a (Fig. 15d), Fe-poor antigorite blades (Fig. 16: 9–7, 9–8, 9–13, 9–14) have pseudomorphically replaced type-5, Fe-poor chrysotile mesh-rims and Fe-poor chrysotile serrate veins. In sample W70–35 brucite occurs so intimately associated with the antigorite that it can only be detected by microbeam camera and microprobe (Fig. 16). In sample W70–41a brucite is abundant and found as discrete grains towards the centres of former olivine grains (Fig. 15d) and less commonly is intimately mixed with the antigorite (Fig. 16). Magnetite is rare in both samples. In sample W70–55, both type-3 relict Fe-poor lizardite–1*T* mesh-rims (Fig. 18: 10–12) and type-5 Fe-poor chrysotile-$2M_{c1}$ + brucite (10–13) serrate veins and hourglass textures (Fig. 17a) are partly replaced by Fe-rich antigorite blades (Fig. 18: 10–19, 10–20). Brucite occurs in fine grains associated with the chrysotile and minor magnetite is associated with all three serpentine minerals. Chlorine was not detected in these samples.

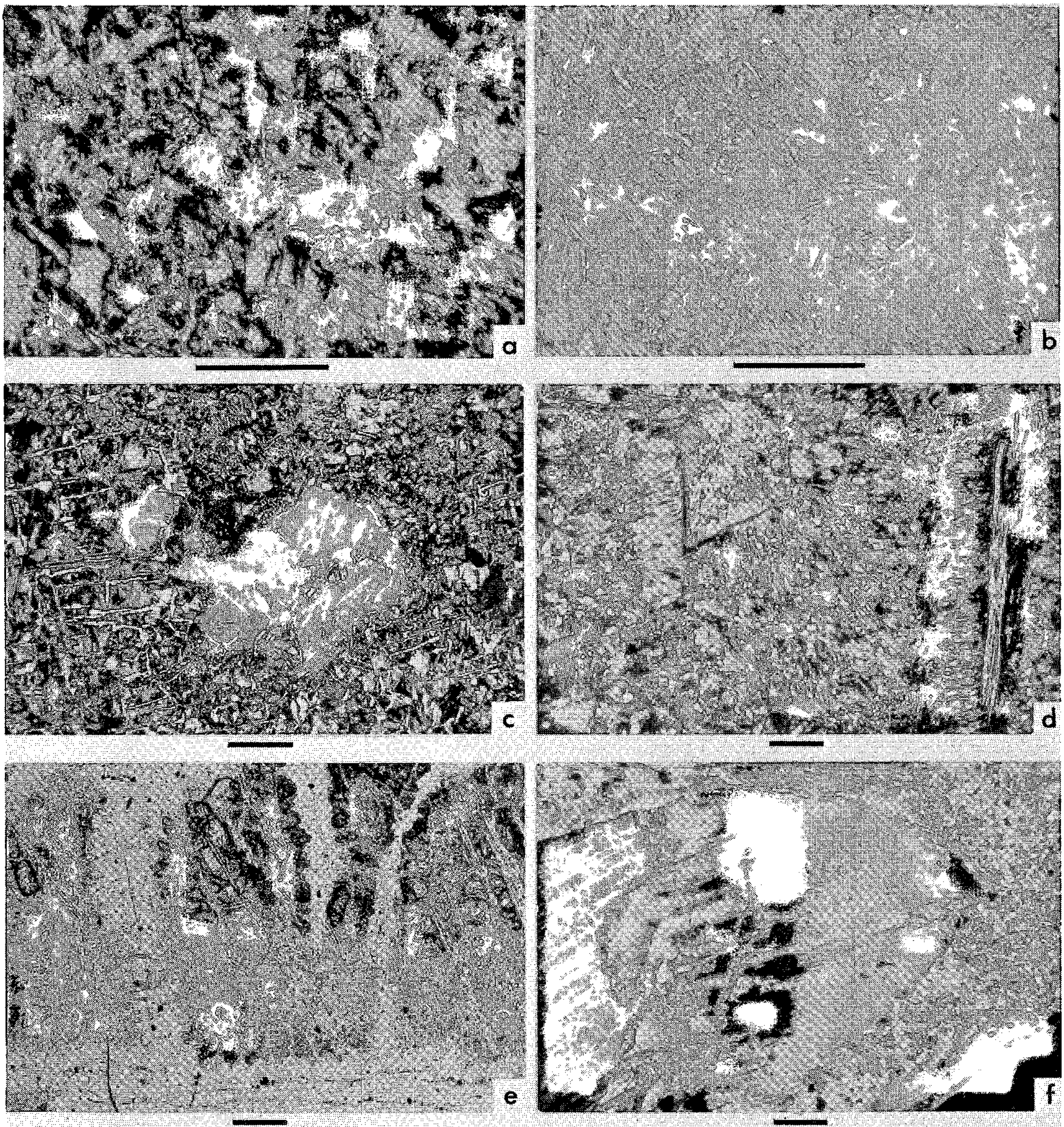

FIG. 15. (a) Relict chrysotile–$2M_{c1}$ serrate veins (9–1, 9–2). Sample W75–62. Crossed nicols. (b) Same as (a), showing antigorite blades (9–3, 9–4) replacing chrysotile serrate veins. Sample W75–62. Mainly reflected light with minor transmitted plane-polarized light. (c) Bastites of a chlorite-like mineral + lizardite–$1T$ (9–6) ± antigorite with small central zone (very dark grey) of relict lizardite–$1T$ (9–5), bastites surrounded by antigorite (9–8) + brucite in interpenetrating textures, antigorite (9–7) after chrysotile serrate vein to the left of bastites, elongate rectilinear antigorite blades on the left replace former mesh-rims. Sample W70–35. Crossed nicols. (d) Antigorite blades (9–13, 9–14) + brucite, vein along right side of Povlen-type chrysotile–$2M_{c1}$ (9–16) + brucite (9–17) marginal slip-zone and non-fibrous chrysotile + brucite central zone. Sample W70–41a. Crossed nicols. (e) Relict mesh-rims of lizardite–$1T$ (10–2), mesh centres (grey zones) of lizardite–$1T$ + brucite (10–3) and relict olivine (10–1) all replaced by antigorite (10–4) (colorless zone) and brucite (10–5) (adjacent to olivine). Sample 18544, plane-polarized light. (f) Relict enstatite (10–6), lizardite–$1T$ (10–7 to 10–9) bastite within magnetite ring, lizardite–$1T$ (10–10, 10–11) bastite outside magnetite ring. Sample 18544. Crossed nicols. Bar represents 0.2 mm.

Sample 18544 is only partly serpentinized (Figs. 15e, 15f) and provides information on the development of the antigorite + brucite directly from olivine, enstatite and lizardite–1*T* + brucite mesh-textures. The olivine (Fo_{91}; Fig. 16: 10–1) has altered to narrow, colorless mesh-rims (10–2) and pale grey mesh-centres (10–3) of a less Fe-rich lizardite–1*T* and variable amounts of submicroscopic brucite + magnetite (Fig. 15e). The estimated FeO value of the brucite is 20%. Brucite-free, slightly Fe-rich antigorite (Fig. 16: 10–4) has formed as veins of subparallel blades (Fig. 15e; WZ, Fig. 6p) along former olivine grain-boundaries and along major fractures in the olivine and replaced both olivine and lizardite + brucite mesh-textures. The areas between these veins, whether relict olivine or lizardite–1*T* + brucite mesh textures, have been replaced by interlocking, anhedral antigorite + brucite grains (WW, Fig. 5d).

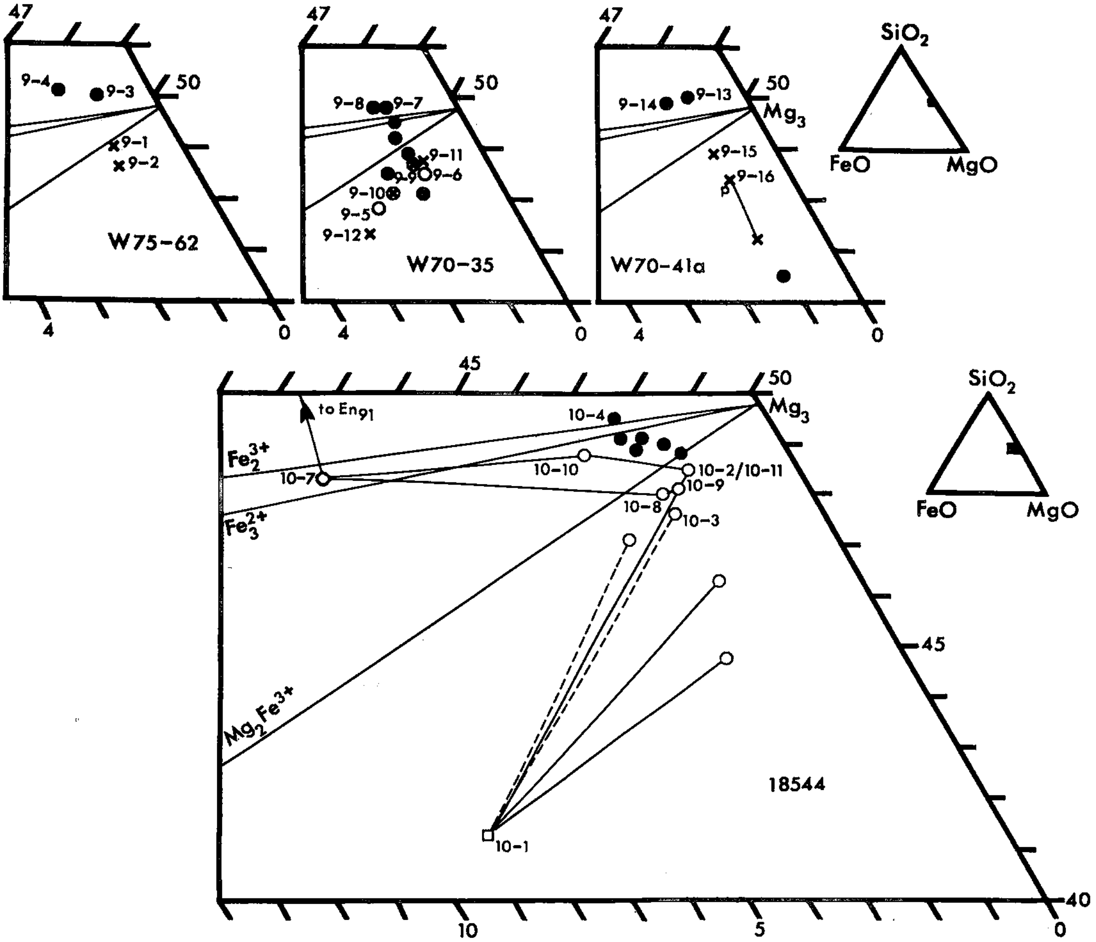

FIG. 16. MgO–FeO–SiO_2 diagrams for type 7. W75–62: 9–1 and 9–2 chrysotile–$2M_{c1}$ serrate veins, 9–3 and 9–4 antigorite blades. W70–35: 9–5 lizardite–1*T* in centre zones of bastites, 9–6 lizardite–1*T* + chlorite-like mineral in outer zones of bastites, 9–7 and 9–8 antigorite blades and associated points of antigorite + brucite, 9–9 chrysotile–$2M_{c1}$ + lizardite–1*T* margin of a recrystallization zone, 9–10 chrysotile–$2M_{c1}$ + lizardite–1*T* central part of a recrystallization zone, 9–11 chrysotile–$2M_{c1}$ + minor parachrysotile marginal zone of a cross-fibre-asbestos vein, 9–12 chrysotile–$2M_{c1}$ and $2Or_{c1}$ (?) + brucite central zone of cross-fibre-asbestos vein. W70–41a: 9–13 and 9–14 antigorite blades and grains, 9–15 chrysotile mesh-rims, 9–16 and associated point, Povlen-type chrysotile-$2M_{c1}$ + brucite in vein. 18544: 10–1 olivine Fo_{91}, 10–2 lizardite–1*T* mesh-rims and associated points of lizardite–1*T* + brucite mesh-rims, 10–3 and associated point, lizardite–1*T* + brucite mesh-centres, 10–4 antigorite grains and associated points of antigorite + brucite, 10–7 most Fe-rich lizardite–1*T* bastite after enstatite, 10–10 intermediate-Fe lizardite–1*T* bastite, 10–8, 10–9 and 10–11 Fe-poor lizardite–1*T* bastite (10–7, 10–8 and 10–9 are inside, 10–10 and 10–11 are outside the magnetite ring).

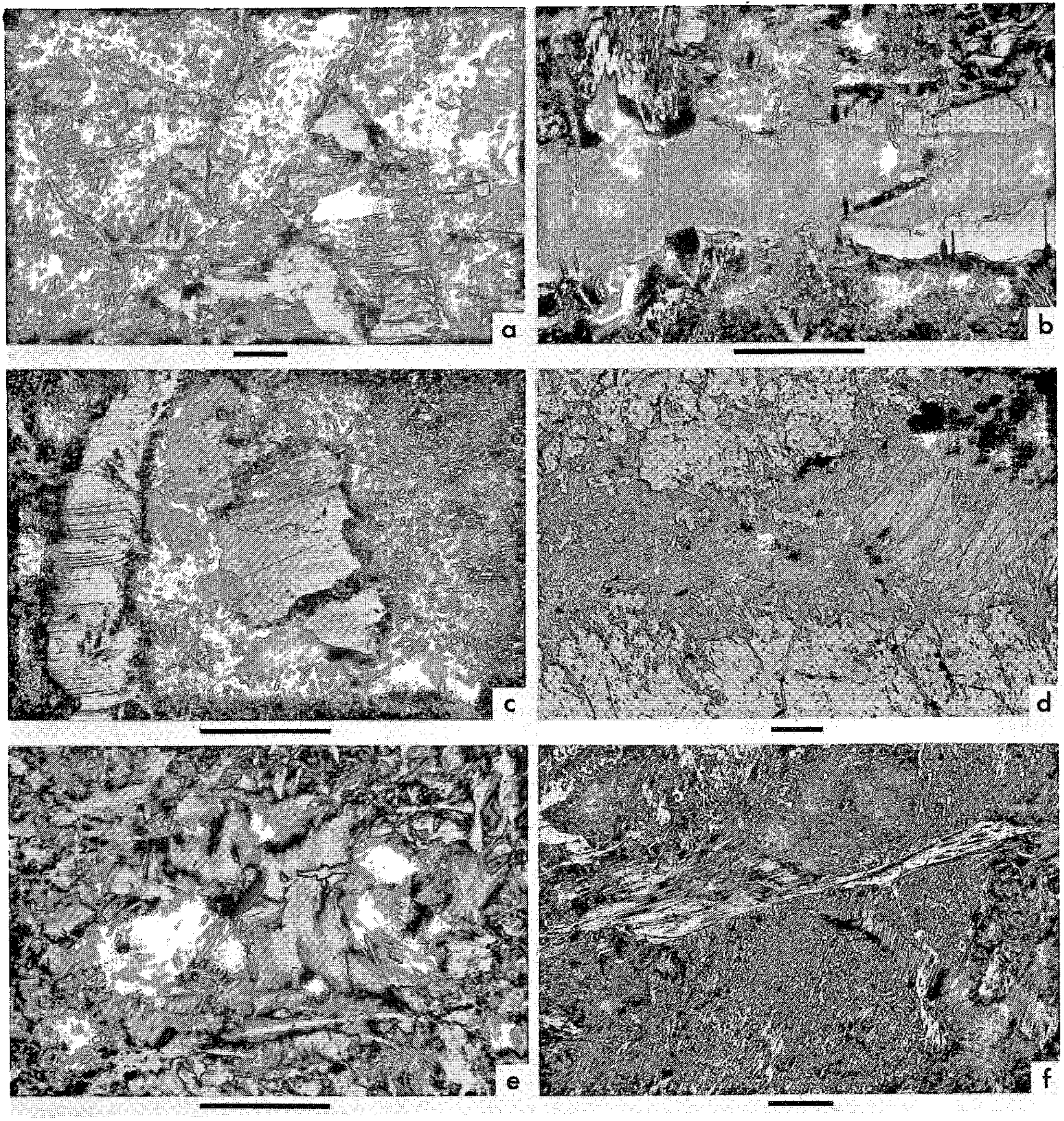

FIG. 17. (a) Enstatite bastite (to SE of centre) of lizardite–$1T$ (10–14) replaced by blades (white patches) of a chlorite-like mineral + lizardite (10–15, 10–17) or a chlorite-like mineral + antigorite (10–16), hourglass texture and serrate veins of chrysotile–$2M_{c1}$ (10–13) + minor brucite. Sample W70–55. Crossed nicols. (b) Relatively Fe-rich chrysotile–$2M_{c1}$ and $2Or_{c1}$ (?) (9–12) that has replaced (left half) an earlier chrysotile—$2M_{c1}$ + minor parachrysotile (9–11) cross-fibre-asbestos vein and the antigorite (9–7, 9–8) in the antigorite + brucite wall-rock adjacent to the vein. Sample W70–35. Crossed nicols. (c) Antigorite (12–6, 12–9) in fine interlocking texture, enstatite bastite of Povlen-type chrysotile–$2Or_{c1}$ (12–4) with relict retrograde composition (12–3) in the nearly extinct zone, antigorite (12–5, 12–7) replacing bastite along partings, veins of Povlen-type chrysotile–$2M_{c1}$ (12-10) cross-fibre asbestos. Sample 18543. Crossed nicols. (d) Enstatite bastite (right side) of Povlen-type chrysotile–$2M_{c1}$ and Minor $2Or_{c1}$ (11–15) recrystallized at the margins (11–16) and associated with a patch of Povlen-type chrysotile–$2M_{c1}$ and minor $2Or_{c1}$ serrate veins (1–17) across centre intermixed with antigorite (11–18, 11–19) on the top and bottom. Sample W76–5, plane-polarized light. (e) Antigorite blades (11–22) in an interpenetrating texture. Sample 18498. Crossed nicols. (f) Antigorite (13–10 to 13–12) in slip zone, antigorite (13–13) in unsheared veins, fine-grained slightly foliated antigorite (13–8). Sample T–179. Crossed nicols. Bar represents 0.2 mm.

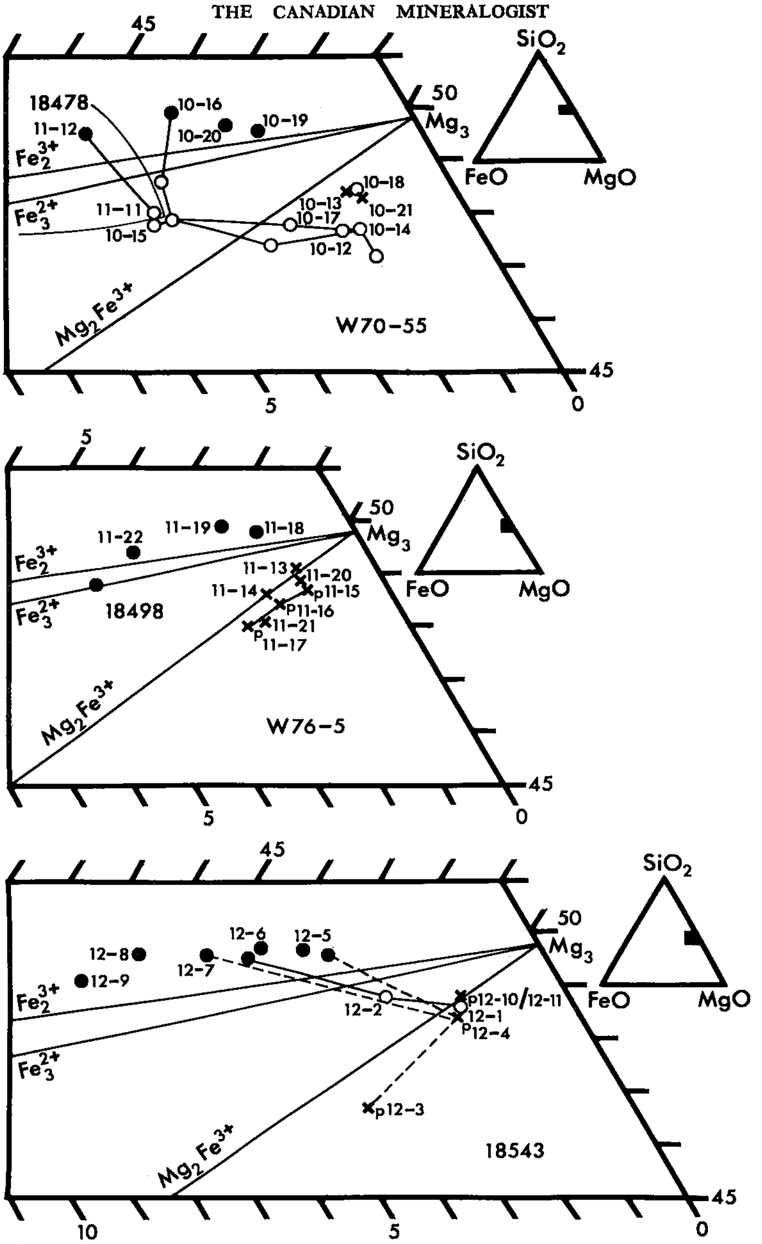

FIG. 18. MgO–FeO–SiO_2 diagrams for type 7. W70–55: 10–12 lizardite–$1T$ mesh-rims, 10–13 chrysotile–$2M_{c1}$ serrate veins and hourglass, 10–14 lizardite–$1T$ bastites after enstatite, 10–15, 10–17 and associated points, a chlorite-like mineral + lizardite–$1T$ blades after bastites, 10–16 a chlorite-like mineral + antigorite blades after bastite, 10–18 lizardite–$1T$ bastites after amphibole, 10–19 and 10–20 antigorite blades, 10–21 chrysotile–$2M_{c1}$ cross-fibre-asbestos veins. 18478: 11–11 lizardite–$1T$ relict mesh-rims, 11–12 antigorite blades. W76–5: 11–13 and 11–14 chrysotile mesh-rims, 11–15 and 11–16 Povlen-type chrysotile–$2M_{c1}$ and minor $2Or_{c1}$ bastites, 11–17 Povlen-type chrysotile–$2M_{c1}$ and minor $2Or_{c1}$ after serrate veins, 11–18 and 11–19 antigorite blades, 11–20 chrysotile–$2M_{c1}$ cross-fibre-asbestos vein, 11–21 chrysotile–$2M_{c1}$ + lizardite–$1T$ slip-fibre vein. 18498: 11–22 and associated point, antigorite blades. 18543: 12–1 lizardite–$1T$ hourglass texture, 12–2 lizardite–$1T$ + antigorite in recrystallized hourglass-texture, 12–3 and 12–4 Povlen-type chrysotile–$2Or_{c1}$ bastites after enstatite, 12–5 antigorite fine grains after bastite, 12–6, 12–7 and 12–9 antigorite fine grains (some of 12–7 after bastite and the point associated with 12–6 after hourglass texture), 12–8 antigorite coarse blades after hourglass texture, 12–10 Povlen-type chrysotile–$2M_{c1}$ cross-fibre-asbestos veins, 12–11 Povlen-type chrysotile–$2M_{c1}$ slip-fibre-asbestos vein.

Brucite occurs as discrete grains (Table 10: 10–5) or intimately associated with antigorite on a submicroscopic scale (Fig. 16). The microbeam diffraction-patterns from some lizardite + brucite mesh-centres contain weak antigorite reflections even though no antigorite is visible in thin section. Minor-element contents of these minerals (Table 10) are low except for Mn concentrated in brucite (10–5); Cl was not detected.

Three samples (W70–35, W70–55 and 18544) also contain bastites. In sample 18544 (Table 10), the lizardite–1*T* after enstatite $Ca_1Mg_{91}Fe_8$ undergoes a large loss of Fe (Fig. 16: 10–7 to 10–11); this has produced a cloud of fine-grained magnetite that rings the outer zone of the bastite in an atoll structure (Fig. 15f). The loss of Fe does not proceed as an advancing front but follows along former enstatite cleavages. The least-affected lizardite (Fig. 16: 10–7) lies within the magnetite ring and has a Mg/Mg + Fe ratio of 0.91, the same as the enstatite. The intermediate (10–10) and Fe-poor lizardite (10–8, 10–9, 10–11) occur on either side of the magnetite, with Mg/Mg + Fe ratios of 0.96 for intermediate lizardite and 0.97 and 0.98 for the Fe-poor lizardite, similar to the lizardite after olivine (10–2). The Al content is low (Table 10) but follows the same decreasing trend as Fe (Fig. 13). The pattern of the Cr is not as clear (Fig. 13) but may be affected by very fine opaque grains occurring in some of the lizardite within the magnetite ring (10–8, 10–9). The lowest Cr content (10–11) occurs in an Fe-poor lizardite outside the magnetite ring. Although no antigorite is visible within the bastite, a few of the microbeam diffraction-patterns of these lizardites also contain weak antigorite reflections, which suggests that as the composition changes, the lizardite begins to recrystallize to antigorite. Minor Cl was consistently detected in lizardites within the magnetite ring but none was detected outside the ring.

The bastites after pyroxene in samples W70–35 and W70–55 display a different response to the prograde environment. The normal retrograde lizardite–1*T* bastites recrystallize to a chlorite-like mineral + antigorite. This mineral produces a series of basal reflections from 001 to 007 and 13*l* or 20*l* reflections that strongly suggest a chlorite diffraction-pattern, but the composition is low in Al for normal chlorite. The chlorite-like mineral occurs intimately associated with both lizardite and antigorite so that complex diffraction-patterns were produced. Thus it was not possible to confirm the identification.

Although the mineralogical changes in the lizardite bastites are similar, in W70–35 and W70–55 the bastites are chemically and visually different. In sample W70–35 a small central zone of slightly Fe-rich lizardite–1*T* of probable relict retrograde origin (Figs. 15c, 16: 9–5) has partly recrystallized to the chlorite-like mineral ± antigorite and with a loss of Fe (Fig. 16: 9–6) and a minor loss of Al and Cr (Fig. 13: 9–5, 9–6). Scattered patches of very fine grained magnetite were produced by this process, similar to but very much less abundant than in bastites in sample 18544. Minor Cl was detected in two of the points analyzed.

In the bastites of sample W70–55 the lizardite–1*T* bastites are Fe-poor (Fig. 18: 10–14), similar to the relict lizardite–1*T* mesh-rims (10–12); it is not known if the bastite composition is an original retrograde type-3 composition or a recrystallization composition produced by the prograde type-5 chrysotile (10–13) + brucite serpentinization. The lizardite-bastites recrystallize to blades (Fig. 17a) composed of a variable mixture of lizardite–1*T*, the chlorite-like mineral and antigorite. The Fe content is variable but increases throughout the recrystallization (Fig. 18: 10–14 to 10–17); both Al-rich (Table 10, Figs. 2, 13: 10–15, 10–16) and Al-poor (10–17) blades evidently have formed. Chromium does not vary much (Fig. 13: 10–15 to 10–17). Thus Fe, Al and Cr seem to vary independently in this process. Minor Cl was detected in one of 14 points of normal lizardite and in one in 8 of the abnormal chlorite-like material. Sample W70–55 also contains lizardite–1*T* bastites after amphibole (Fig. 18: 10–18); these have compositions very similar to the chrysotile serrate veins (10–13) and are free of Cl.

Veins were produced as the final event, following the development of the rock-forming minerals, in three samples, W70–41a, W70–55 and W70–35. Those in W70–41a (Fig. 15d) are composed of marginal slip-fibre zones of Povlen-type Fe-poor chrysotile-$2M_{c1}$ + brucite (Fig. 16: 9–16) and zones of relatively pure brucite (Table 9: 9–17), and a central zone of a mixture of nonfibrous, Povlen-type chrysotile–$2M_{c1}$ blades and discrete brucite anhedral grains. The veins were developed after the rock-forming antigorite + brucite, but plot on the same Fe-trend as the earlier serpentine minerals and brucite (Fig. 16). Manganese is high in brucite (Table 9: 9–17) compared with chrysotile (9–16).

Sample W70–55 contains chrysotile–$2M_{c1}$ cross-fibre-asbestos veins (Fig. 18: 10–21) that have a similar composition to the chrysotile serrate veins (10–12) except for a high Cr content (Table 10), even though they have formed after the development of the relatively Fe-rich antigorite blades that replace the serrate veins.

Sample W70–35 has two sets of complex and closely related veins (Table 9). The first set contains chrysotile–$2M_{c1}$ + lizardite–$1T$ with abundant magnetite and brucite. These veins are not fracture-filling but follow sinuous planes and seem to form by recrystallization of the host antigorite. The antigorite adjacent to the veins has abundant discrete grains of magnetite and brucite unlike the rest of the antigorite, which is magnetite-free and contains submicroscopic brucite. The margins of these veins (Fig. 16: 9–9) are similar in composition to the host antigorite + brucite (9–7, 9–8) but the central zone is more Fe-rich (9–10). Complex fracture-filling veins (Fig. 17b) cut, but are closely related to, the recrystallization veins. The margins of these veins are composed of chrysotile-$2M_{c1}$ + minor parachrysotile cross-fibre asbestos (Fig. 16: 9–11) with a composition similar to the antigorite + brucite host-rock (9–7, 9–8) and the margin of the recrystallization veins (9–9). The cross-fibre-asbestos veins have been intruded along the central partings by a more Fe-rich nonfibrous chrysotile–$2M_{c1}$ + $2Or_{c1}$(?) + brucite (Fig. 16: 9–12). (The identification of the chrysotile–$2Or_{c1}$ is uncertain because the possible 203 reflection is obscured by the brucite 101 reflection. The presence of possible very faint $02l$ superlattice reflections suggests that this may be a Povlen-type serpentine with a cylindrical chrysotile–$2M_{c1}$ core and a polygonal overgrowth of multilayer lizardite. However, according to the convention described in the Analytical Methods, this is listed as chrysotile–$2Or_{c1}$ until the identification can be clarified.) Elongate lenses of magnetite with associated brucite parallel the chrysotile-asbestos fibres and often pass completely through both parts of the vein

TABLE 11. PROGRADE TYPE-7 ANTIGORITE

Sample No.	AG67-67b	18540			AG67-64a					W70-72
Analysis No.	1	2	3	4	5	6	7	8	9	10
Pts. Analyzed	3	2	1	3	5	2	2	3	3	10
SiO_2	44.6	43.2	42.9	43.8	42.5	42.3	42.0	54.6	54.6	44.2
Al_2O_3	0.35	0.44	0.18	0.27	0.63	1.0	1.2	0.32	0.29	0.33
Cr_2O_3	0.0	0.37	0.21	0.29	0.0	0.03	0.07	0.06	0.03	0.0
FeO^*	2.1	8.4	9.0	10.0	2.7	2.5	2.9	1.5	1.9	2.8
MnO	0.06	0.13	0.08	0.09	0.15	0.13	0.15	0.17	0.17	0.04
MgO	42.3	36.4	36.5	36.2	40.1	40.0	39.9	18.1	17.9	41.9
CaO	0.0	0.03	0.0	0.0	0.02	0.0	0.0	25.1	24.9	0.0
Na_2O	0.0	0.0	0.0	0.0	0.0	0.0	0.0	0.05	0.04	0.0
K_2O	0.0	0.0	0.0	0.0	0.0	0.0	0.0	0.04	0.0	0.0
Total	89.41	88.97	88.87	90.65	86.10	85.96	86.22	99.94	99.83	89.27

Sample No.	18478		W76-5									18498
Analysis No.	11	12	13	14	15	16	17	18	19	20	21	22
Pts. Analyzed	7	7	4	3	6	2	4	8	4	2	2	17
SiO_2	39.0	41.5	41.7	41.6	40.5	41.7	40.0	43.8	44.2	42.3	39.6	43.1
Al_2O_3	2.5	1.0	0.48	0.63	0.61	0.64	0.52	0.43	0.36	0.58	0.70	1.9
Cr_2O_3	0.0	0.0	0.09	0.08	0.43	0.20	0.10	0.03	0.1	0.14	0.21	0.08
FeO^*	4.1	4.7	1.1	1.7	1.1	1.7	2.2	1.4	1.8	1.1	1.9	3.3
MnO	0.02	0.05	0.0	0.0	0.0	0.0	0.0	0.0	0.0	0.0	0.0	0.02
MgO	38.00	37.7	42.1	42.3	41.6	42.8	41.2	42.7	42.5	43.0	40.9	40.9
CaO	0.0	0.0	0.0	0.0	0.0	0.05	0.0	0.0	0.0	0.0	0.0	0.0
Na_2O	0.0	0.0	0.0	0.0	0.0	0.0	0.0	0.0	0.0	0.0	0.0	0.0
K_2O	0.0	0.0	0.0	0.0	0.0	0.0	0.0	0.0	0.0	0.0	0.0	0.0
Total	83.62	84.95	85.47	86.31	84.24	87.09	84.02	88.36	88.96	87.12	83.31	89.30

Analysis No. 1, 2, 3, 4, and 5, antigorite blades; 6 and 7, antigorite blades in a vein; 8 and 9, secondary diopsides; 10, antigorite blades; 11, lizardite-$1T$ relict mesh rims; 12, antigorite blades; 13 and 14, chrysotile mesh rims; 15, 16, and 17, Povlen-type chrysotile-$2M_{c1}$ + minor $2Or_{c1}$ bastites; 18 and 19, antigorite blades; 20, chrysotile-$2M_{c1}$ cross-fibre asbestos vein; 21, chrysotile-$2M_{c1}$ + lizardite-$1T$ slip-fibre vein; 22, antigorite blades.

*Total iron calculated as FeO.

and into the adjacent host antigorite, which also contains abundant brucite and magnetite. The more Fe-rich central chrysotile replaces some of the early Fe-poor chrysotile asbestos and the antigorite of the wall rock (Fig. 17b).

Antigorite. Four samples of early-stage antigorite blades were analyzed, two from type-3 lizardite hourglass-textures (AG67–67b, 18540) and two from chrysotile + lizardite mesh-textures (AG67–64a, W70–72: Table 11). The microbeam X-ray-diffraction patterns recorded from this early antigorite are similar to the powder-diffraction patterns of samples 29 and 30 given by Whittaker & Zussman (1956, Table III, 5th & 6th columns). They contain fewer superlattice reflections than expected for antigorite, and are less streaky than those shown in Wicks & Zussman (1975, Figs. 6o and 6p), which suggests a less-well-developed antigorite structure.

The antigorite blades after the lizardite–1*T* hourglass (Fig. 6: 11–1), and the chrysotile + lizardite mesh-texture (Fig. 10: 11–5, 11–10) are all slightly less Fe-rich than the parent serpentine but the antigorite after Fe-rich Povlen-type chrysotile-bastites is more Fe-rich (Fig. 6: 18540). In general, the minor elements are similar (Table 11).

A more advanced, intermediate stage of the development of antigorite after retrograde type-3 lizardite–1*T* mesh-texture is illustrated by 18478. Mesh centres are completely replaced and mesh rims (Fig. 18: 11–11) partly replaced, by randomly oriented interpenetrating antigorite blades (11–12). The antigorite produces a well-developed microbeam diffraction-pattern and is slightly more Fe-rich than the host lizardite rims although the original mesh-centre composition is not known. The Al content of the lizardite–1*T* is uncommonly high, but is considerably reduced in the antigorite (Table 11). Chlorine was detected in all points of lizardite and antigorite analyzed; this is the only case of abundant Cl in antigorite textures encountered in the present study.

Sample W76–5 represents a well-advanced, almost complete development of antigorite with a well-developed diffraction pattern, after a possible chrysotile + lizardite mesh-texture. The antigorite (Fig. 18: 11–18, 11–19) and chrysotile (11–13, 11–14) have a similar range in Fe and minor elements (Table 11).

A fully developed antigorite serpentinite is illustrated by sample 18498. All earlier textures have been replaced by antigorite in interpenetrating textures, with scattered anhedral magnetite grains and partly replaced relict chromite grains. The Fe values of the analyses are fairly tightly grouped at a moderate Fe content (Fig. 18: 11–22) except for some strongly foliated antigorite that seems to be slightly more variable (Fig. 18: point associated with 11–22). The Al content of this antigorite is fairly high for antigorite (Fig. 2: 11–22). Other minor elements are generally low (Table 11) except for Cr, which rises slightly in antigorite near chromite grains.

In contrast to the typical development of antigorite described above, in which the grain size of the antigorite is relatively coarse and constant within each sample, sample 18543

TABLE 12. PROGRADE TYPE-7 ANTIGORITE

Sample No.	18543										
Analysis No.	1	2	3	4	5	6	7	8	9	10	11
Pts. Analyzed	3	2	2	10	3	6	7	3	1	11	3
SiO_2	41.3	42.8	38.8	40.5	44.0	44.4	44.6	44.9	44.3	42.2	42.5
Al_2O_3	0.40	0.45	3.2	0.43	0.31	0.26	0.27	0.32	0.32	0.37	0.40
Cr_2O_3	0.02	0.0	2.1	0.27	0.04	0.0	0.04	0.03	0.0	0.02	0.02
FeO^*	1.6	2.6	3.6	1.7	3.4	4.2	5.0	5.9	7.1	1.6	1.7
MnO	0.0	0.06	0.0	0.04	0.07	0.07	0.10	0.10	0.12	0.02	0.0
MgO	42.0	42.4	40.7	41.5	41.1	40.8	40.4	39.7	38.9	42.9	43.4
CaO	0.0	0.0	0.0	0.0	0.0	0.0	0.0	0.0	0.0	0.0	0.0
Total	85.32	88.31	88.40	84.44	88.92	89.73	90.41	90.95	90.74	87.11	88.02

Analysis No. 1, lizardite-1*T* hourglass texture; 2, lizardite-1*T* + antigorite in recrystallized hourglass texture; 3 and 4, Povlen-type chrysotile-$2Or_{a1}$ bastites after enstatite; 5, antigorite fine grains after bastite; 6, 7, and 9, antigorite fine grains (some of 7 after bastite); 8, antigorite coarse blades after hourglass texture; 10, Povlen-type chrysotile-$2M_{a1}$ cross-fibre asbestos veins; 11, Povlen-type chrysotile-$2M_{a1}$ slip-fibre asbestos vein.

*Total iron calculated as FeO.

contains both very fine-grained interlocking antigorite (Fig. 17c) that gives rudimentary diffraction patterns, and minor patches of very coarse-grained interpenetrating antigorite that produces well-developed diffraction patterns. The formation of the antigorite caused the Fe-poor lizardite–1*T* hourglass-textures (Fig. 18: 12–1) to recrystallize to a fine-grained lizardite (12–2) before complete recrystallization to a more Fe-rich antigorite. The antigorites have variable compositions (Table 12) but are more Fe-rich than the parent serpentine (Fig. 18: 12–5 to 12–9). Magnetite occurs in trace amounts.

Bastites are present in samples 18540, 18543 and W76–5. All seem normal lizardite bastites but all three are composed of Povlen-type chrysotile. Those in 18540 (Fig. 9b) are composed of a very Fe-rich Povlen-type chrysotile–$2M_{c1}$ and $2Or_{c1}$ with minor Povlen-type parachrysotile (Fig. 6: 3–13, 3–14) and have been partly replaced by even more Fe-rich antigorite blades (11–2 to 11–4). Aluminum is fairly low but Cr is relatively abundant in the chrysotiles (Fig. 13: 3–13, 3–14); the replacing antigorite has similar (11–2) or slightly lower (11–3, 11–4) Al and Cr contents than the parent. The microbeam diffraction-patterns indicate that these Povlen-type chrysotiles do not have well-formed cylindrical structures.

In sample 18543, Fe- (Fig. 18: 12–3), Al- and Cr-rich (Fig. 13: 12–3) Povlen-type chrysotile zones that must approximate the original composition (compare Fig. 13: 12–3 with Fig. 8) occur in some bastites (Fig. 17c). Most of the bastites have changed to an Fe- (Fig. 18: 12–4), Al- and Cr-poor (Fig. 13: 12–4) composition and are replaced along partings by a fine-grained Fe-rich antigorite (Fig. 18: 12–5, 12–7). The Povlen-type chrysotile in this case is chrysotile–$2Or_{c1}$ with a well-developed cylindrical structure as well as the Povlen structure.

Sample W76–5 is different from the other two examples (Fig. 17d). It contains well-formed Fe-poor (Fig. 18: 11–15) and Al-poor but relatively Cr-rich (Fig. 13: 11–15) bastites that have recrystallized at the margins to higher Fe and lower Cr compositions (11–16) and are associated with irregular patches of even higher Fe and lower Cr compositions (11–17). All three composition zones are composed of Povlen-type chrysotile–$2M_{c1}$ and minor $2Or_{c1}$. The chrysotile in the bastite is in parallel alignment and produces a fibre-type diffraction pattern indicating a cylindrical structure. The chrysotile at the margins of the bastites and in the zones away from the bastites are in random orientation. The irregular patches are probably not part of the bastites but are definitely associated with them; they may be relict chrysotile serrate veins being replaced by antigorite, although the textural evidence is not conclusive. Similarly, in some areas of the thin section, relict chrysotile mesh-rims may have been rejuvenated, replacing adjacent antigorite, but again the evidence is inconclusive.

Veins occur in several antigorite-bearing samples: 18540, AG67–67b, AG67–64a, W70–72, 18543 and W76–5. The chrysotile cross-fibre-asbestos veins cutting the lizardite hourglass-textures in samples 18540 and AG67–67b have been described in the section on type-3, lizardite + chrysotile veins. However, in both samples the chrysotile veins clearly cut the antigorite (Fig. 5e) but in places they also are slightly disrupted by antigorite blades. The chrysotile + lizardite mesh-texture (Fig. 10: 6–4, 6–5) and antigorite blades (11–10) in sample W70–72

TABLE 13. PROGRADE TYPE-8 ANTIGORITE

Sample No.	T-179												
Analysis No.	1	2	3	4	5	6	7	8	9	10	11	12	13
Pts. Analyzed	3	4	3	1	1	3	2	2	3	11	2	1	8
SiO_2	41.9	42.5	43.3	39.0	40.9	41.2	42.1	41.4	41.2	42.8	42.2	42.4	42.4
Al_2O_3	0.28	0.39	0.56	2.5	2.1	2.2	0.64	1.7	1.4	0.72	0.80	0.52	0.74
Cr_2O_3	0.04	0.0	0.0	0.92	0.70	0.93	0.0	0.65	0.42	0.02	0.13	0.16	0.09
FeO^*	4.6	4.3	6.0	9.0	7.9	7.3	5.5	6.9	7.4	6.6	8.1	10.1	8.6
MnO	0.0	0.03	0.07	0.02	0.12	0.09	0.06	0.11	0.08	0.08	0.10	0.26	0.14
MgO	40.9	40.8	38.7	36.6	35.2	37.1	38.1	37.0	36.5	38.1	36.8	34.4	35.8
CaO	0.02	0.02	0.0	0.02	0.11	0.13	0.0	0.0	0.0	0.04	0.05	0.16	0.10
Total	87.74	88.04	88.63	88.06	87.03	88.95	86.40	87.76	87.00	88.36	88.18	88.00	87.87

Analysis No. 1, lizardite-1*T* hourglass textures; 2, lizardite-1*T* recrystallized hourglass textures; 3, antigorite blades after recrystallized lizardite-1*T* hourglass textures; 4, lizardite-1*T* bastites; 5, antigorite blades after lizardite-1*T* bastite; 6, lizardite-1*T* recrystallized bastites; 7 and 9, antigorite coarse blades; 8, antigorite fine blades; 10, antigorite blades in slip-veins; 11 and 12, antigorite fibres in slip-vein; 13, antigorite blades in veins without shearing.

*Total iron calculated as FeO.

are cut by Fe-poor chrysotile–$2M_{c1}$ slip-veins (6–6).

The chrysotile + lizardite mesh-textures in sample AG67–64a have a complex vein-history, described above. The vein system continued in the prograde-antigorite stage with the development of Al-rich (Table 11) antigorite (Fig. 10: 11–6, 11–7) veins occupying the same fractures as, but not replacing the slightly Al-poor and slightly more Fe-rich lizardite (6–18). Accompanying antigorite slip-fibre veins were not analyzed.

Sample W76–5 is cut by Fe-poor chrysotile–$2M_{c1}$ cross-fibre-asbestos veins (Fig. 18: 11–20) and Fe-rich chrysotile–$2M_{c1}$ + lizardite–1*T* slip-veins (11–21) that display the same Fe-range as the bastites and associated chrysotile mesh-rims (Fig. 18). Both types of veins occupy some of the same fractures, with the cross-fibre veins following the slip veins, but both postdate the antigorite.

In sample 18543, Povlen-type chrysotile–$2M_{c1}$ forms closely related cross-fibre-asbestos (Fig. 17c) and slip-fibre veins of identical composition (Table 12, Fig. 18: 12–10, 12–11) that have been formed after antigorite development. The composition of these veins is also identical to the relict lizardite in the hourglass texture (12–1).

Type 8: *antigorite*

Type-8 serpentinization occurs during prograde shearing of ultramafic rocks at intermediate to high temperatures, and produces foliated antigorite ± brucite. Sample T–179, representing type 8, contains antigorite without brucite. Prior to shearing and the development of antigorite, the assemblage was composed of lizardite–1*T* hourglass-texture and bastite after enstatite without brucite or magnetite. The lizardite–1*T* hourglass has a moderate but slightly variable Fe content, minor Al content and only very minor amounts of other elements (Table 13, Fig. 19). The lizardite–1*T* bastites have much higher Fe (Fig. 19: 13–4), Al and Cr (Fig. 13: 13–4). The lizardite hourglass is partly recrystallized to fine-grained, randomly oriented lizardite–1*T* with a similar but not identical composition to the lizardite hourglass from which it formed (Fig. 19: 13–1, 13–2) but other areas contain both lizardite and antigorite and have compositions intermediate between the lizardite and antigorite (Fig. 19). To a lesser degree the lizardite bastites also have partly recrystallized to antigorite. The antigorites formed have the same high Fe content (Fig. 19) but slightly lower Al and Cr contents (Fig. 13: 13–5, 13–8, 13–9) as the host lizardite (13–4). But Al is still notably high for antigorite (Fig. 2: 13–5). Cross-fibre-asbestos veins of chrysotile–$2M_{c1}$ with minor parachrysotile cut the lizardite pseudomorphic textures, but are themselves cut by antigorite shear zones and veins. The shear-zone antigorites, as well as the recrystallization antigorite formed after lizardite pseudomorphs, have the greatest range in Fe contents found in this study (Table 13, Fig. 19). Fe-rich antigorites have a pale yellow birefringence rather than the bluish-grey color of less Fe-rich antigorites. Most of the vein- and rock-forming antigorites, except those after bastites, have moderately low Al and low Cr (Table 13).

INTERPRETATION

The combined electron-microprobe and micro-

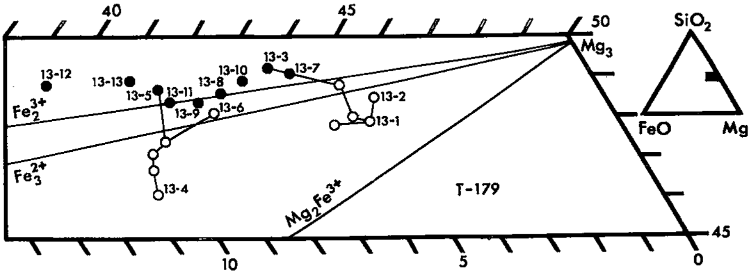

FIG. 19. MgO–FeO–SiO$_2$ diagram for type 8. T–179: 13–1 lizardite–1*T* hourglass–textures, 13–2 and three associated points, lizardite–1*T* recrystallized hourglass-textures, 13–3 antigorite blades after recrystallized lizardite–1*T* hourglass-textures, 13–4 lizardite–1*T* bastites, 13–5 antigorite blades after lizardite–1*T* bastite, 13–6 and three associated points, lizardite–1*T* in recrystallized bastites, 13–7 and 13–9 antigorite in coarse blades, 13–8 antigorite in fine blades, 13–10 antigorite blades in slip veins, 13–11 and 13–12 antigorite fibres in slip vein, 13–13 antigorite blades in veins without shearing.

beam-X-ray-camera study has provided data that help to clarify some of the details of the serpentinization process, but it also has revealed unsuspected complexities. The data will be discussed first in terms of successive generations of serpentines after olivine and pyroxene in unsheared environments, and then in instances of shearing. Finally, veins and the role of chlorine will be discussed.

Serpentinization of olivine

The formation of retrograde type-3, lizardite ± brucite mesh- and hourglass-textures after olivine has been outlined by Wicks *et al.* (1977) and Wicks & Whittaker (1977), and has been modified by Cressey (1979). Cressey has found that the advancing front of serpentinization into olivine is a two-stage process. At the front of serpentinization, fine-grained, randomly oriented serpentine is formed, followed closely by recrystallization to moderately well-oriented, coarser grained lizardite that forms the mesh rims, or, in the case where the two-fold process advances to completion, hourglass textures. Mesh centres are formed where the recrystallization to coarse lizardite stops and forms the mesh rims, but the advancing front of fine-grained random serpentine continues to consume all the olivine, forming the mesh centres. However, this interpretation ignores the observation made earlier by Wicks & Whittaker (1977) and again in the present study, that relict olivine in mesh centres is not always replaced by an advancing front of serpentine but may serpentinize simultaneously through the entire olivine relic. This seems to produce the lizardite–1*T* mesh centres, with anomalously high Si contents, at the intermediate stage between olivine and normal randomly oriented lizardite–1*T* mesh-centres (Figs. 5b, 6). Golightly & Arancibia (1979) have described similar Si-rich features in deeply weathered serpentinites in laterites but the two samples in our study, although surface samples, are not obviously deeply weathered and produce some sharp lizardite diffraction-patterns that suggest a well-developed crystallinity. Further detailed work is necessary to solve the high Si problem.

The microprobe and microbeam camera results from mesh textures after olivine indicate that lizardite–1*T* (± minor chrysotile: Cressey 1979) changes with degree of serpentinization from an inhomogeneous mineral with highly variable Fe contents to a homogeneous mineral with uniformly low Fe contents (Fig. 6). Simultaneously, the secondary magnetite produced forms coarser and coarser aggregates, and the brucite, where present, is more Fe-rich than the coexisting lizardite. Not much can be said about the retrograde antigorite type-1 mesh-textures, as only one sample was examined (Fig. 4). However, the chemical changes and development of magnetite are similar to those of the lower-grade type-3 lizardite mesh-textures.

Lizardite–1*T* hourglass textures (Fig. 5e) can be imagined developing as an extension of mesh textures (Wicks *et al.* 1977) but the conditions that produce lizardite–1*T* hourglass textures have been a puzzle. The uniform and low Fe-contents of lizardite–1*T* (Fig. 6: AG67–67b) and lizardite–1*T* + brucite (Fig. 7: AG67–70a) hourglass-textures suggest that they are developed as the end product of thorough serpentinization. However, sample 18540 (Fig. 6) has a uniform composition but it is Fe-rich, suggesting that the Fe-depletion path of serpentinization, although common, is not the only path followed. All lizardite hourglass-textures studied have been slightly replaced by minor amounts of antigorite (Fig. 5e), indicating that for some time the rocks had passed above the thermal stability of lizardite into the temperature range where antigorite is the stable serpentine mineral. It seems likely that the lizardite hourglass-textures developed during this increase in temperature. However, well-developed lizardite ± brucite hourglass-textures (AG67–70a) may be free of antigorite, indicating that the development of antigorite is not essential to the development of hourglass textures. Thus lizardite hourglass-textures may not be true retrograde textures, but may represent a bridge between type-3 retrograde and type-5 prograde serpentinization. Exactly the same arguments apply to chrysotile + lizardite mesh-textures (Fig. 11a) so that they too represent a bridge between types 3 and 5. This interpretation is strengthened by the chrysotile + lizardite mesh-texture in sample 18501, which was recognized as type 5 (Wicks & Whittaker 1977) by its association with other prograde textures. Thus the chrysotile + lizardite mesh-textures described as type 3 in Table 1 (AG67–64a, W70–72, IB67–265) and as type 5 (18501) are part of a series of textures bridging the retrograde and prograde regimes. This mild prograde event might also account for the development of the relatively rare chrysotile mesh-rims rather than the more common lizardite mesh-rims characteristic of most retrograde type-3 serpentinization.

During prograde metamorphism, olivine (whether primary or already partly altered to retrograde mesh-textures) may alter directly to chrysotile + brucite or to antigorite + brucite. The replacement is dominated by chrysotile or antigorite at the edges of the olivine grains and by brucite at the centres of the grains (Fig. 15d: W70–41a). The chrysotiles in the mesh centres and the lizardite in the associated relict mesh-rims have similar compositions; this suggests that they are both stable, with respect to one another, under type-5 conditions (Figs. 11b, 12: 18538, Fig. 18: W70–55).

With continued prograde metamorphism the chrysotile may be replaced pseudomorphically by antigorite preserving the form of the chrysotile hourglass and serrate veins (Fig. 15c) or nonpseudomorphically, destroying the earlier textures. In the pseudomorphic (Fig. 16: W70–35, W70–41a) or partly pseudomorphic (W75–62) replacement, the antigorite has a very similar or only slightly more Fe-rich composition than the parent chrysotile, which suggests that during a rise in temperature recrystallization took place without much change in composition (Evans *et al.* 1976, Fig. 4). In the nonpseudomorphic replacement, the antigorite has a considerably more Fe-rich composition (Fig. 18: W70–55), which suggests a more complex reaction. Antigorite + brucite may also form directly through the replacement of olivine without first altering to chrysotile + brucite (Figs. 15e, 16: 18544). This probably indicates that water was absent during early prograde conditions, but that it reached the rock later when the temperature was too great for the stable formation of chrysotile + brucite. A second possibility, based on the statement by Evans *et al.* (1976) that chrysotile + brucite can only form at extremely low pressures, is that pressures were too high for chrysotile + brucite to form from olivine + water. However, other samples such as 18538 from the same intrusion as sample 18544 do contain chrysotile + brucite, so that pressures probably were not above the limit for chrysotile + brucite; thus the supply of water was the limiting factor.

The development of serpentine + brucite rather than serpentine alone is dependent on bulk composition as well as temperature. In this respect it is interesting to note that all but two of the serpentine + brucite assemblages in this study have developed in dunites that have experienced different types of serpentinization. These include retrograde type-3 lizardite + brucite (18508, 18529, AG67–70a), type-3 and -5 chrysotile + lizardite + brucite assemblages (IB67–265), prograde type-5 chrysotile + brucite (W70–55) and type-7 antigorite + brucite assemblages (W70–35, W70–41a, W70–55). The two exceptions are olivine-rich harzburgites (18538, 18544), discussed in the pyroxene section. There are also four dunites that alter to brucite-free assemblages of type-3 lizardite (18491, AG67, 67b) and type-3 and -5 chrysotile + lizardite (W70–72, 18501) but at least for the last two, and possibly the first two, the temperature of serpentinization was high, probably above the temperature at which olivine would alter to serpentine + brucite.

During the earliest stages of antigorite-producing prograde metamorphism, antigorite appears as coarse isolated blades (Figs. 5e, 9b) or as very fine grains. In the latter case, antigorite may be detected by microbeam X-ray diffraction even before it can be seen with the microscope. Regardless of the grain size in the early stage, antigorite is poorly crystalline, as indicated by its diffraction patterns, but becomes more crystalline as its development advances. Antigorite crystallization may begin in fine-grained, poorly crystalline serpentine such as the mesh centres in retrograde lizardite ± brucite mesh-textures (Fig. 18: 18478) or in the poorly crystalline lizardite recrystallization-zones in lizardite hourglass-textures (Fig. 18: 12–1, 12–2) or along fine fractures or other planar features (Fig. 5e). Lizardite (Fig. 18: 18478) and chrysotile mesh-rims (Fig. 18: W76–5), to some extent, resist recrystallization to antigorite probably because of their greater degree of crystallinity.

The distribution of Fe among antigorite, the minerals being replaced and magnetite is variable, reflecting the conditions prevailing at the time of formation of the antigorite. Under nonshearing conditions the composition of all the pre-antigorite serpentines may migrate to a common nonantigorite composition before they recrystallize directly to coarse antigorite blades without producing phases with compositions intermediate to the parent serpentines and the resulting antigorites (Figs. 16, 18). In the case of fine-grained antigorite recrystallization the resulting mixtures of antigorite and parent serpentine produce intermediate compositions which make it appear that the compositions migrate across to the resulting antigorite composition (Figs. 10, 18: 18543).

In well-developed prograde textures the composition of the serpentine becomes quite homogeneous, similar to advanced retrograde textures. This is true of type-7 antigorite (Fig. 18: 18498) and antigorite + brucite (Fig. 16: W70–35) textures as well as type-5 chrysotile + brucite (Fig. 12: 18538), chrysotile + lizardite (Fig. 12: 18501) and lizardite (Fig. 12: 18559). In the case of the lizardite type-5 interpenetrating textures (Fig. 11d) it is not possible, on the basis of a single sample, to establish its position in the prograde regime, but as it has been developed by prograde events it also serves to indicate that lizardite does have a stability field in prograde metamorphism.

Serpentinization of pyroxene

The data collected from enstatite bastites indicate that their role in the various serpentinization processes is mineralogically and chemically more complex than previously understood. In the following discussion we have adopted the assumption, described by Wicks & Whittaker (1977, Table 5) that serpentinization is a topotactic process that preserves the anion framework of close-packed oxygens of the host mineral. All the retrograde enstatite-bastites studied are composed of lizardite–1*T* or multilayer lizardites, and have Al and Cr contents that set them apart from the associated lizardite–1*T* after olivine (Fig. 8), although they do follow a similar path of development. Early-formed bastites seem to have a greater variation in Fe contents than later-formed bastites (Fig. 6). In the late stage of retrograde serpentinization the lizardite bastites tend to be more Fe-rich than the associated lizardite ± brucite mesh-textures (Figs. 6, 7). The mobility of individual elements is variable. Calcium is probably the most mobile as it is completely removed from thoroughly serpentinized bastites. Although mobile within bastites, iron does not seem to leave because secondary magnetite is very rarely produced during serpentinization of enstatite. Aluminum has a more complex distribution. The pyroxenes must be the main source of minor but persistent Al in most lizardite ± brucite mesh- and hourglass-textures, and the Al in the multilayer-lizardite veins (discussed below).

The mobility of Al is surprising, as Al is the element that most efficiently reduces the misfit between the octahedral and tetrahedral sheets. Therefore, it might be expected to be fixed in the nearest octahedral or tetrahedral site of an available lizardite and thus not widely redistributed. The explanation for the mobility is that the migration of Al is linked to that of Si. One third of the Si in enstatite is removed during serpentinization so that the Si-rich bulk composition becomes that of serpentine (WW, Table 5). Some of the Al in enstatite is in the tetrahedral site and seems to move with the Si. Interestingly, the lizardite + brucite bastites after enstatite (18529) that have lost the most Si owing to the development of brucite have also lost the most Al and Cr (Fig. 8: compare 5–12 to 5–14 with 3–10 to 3–12). In spite of this loss of some Al, most bastites remain more Al-rich than the associated mesh-textures (Fig. 8). Chromium is slightly less mobile in bastites, but there is evidence that Cr is depleted at the edges of lizardite bastites (Fig. 8: 3–5). Only three examples of diopside bastites (Table 3: FW–L–4, 18530, Table 6: AG67–64a) were examined in this study, so that it is not possible to follow their development as closely as the enstatite bastites. However, all examples studied have the distinctive high Cr and Al of the enstatite bastites (Fig. 8: 3–16, 3–17, 3–18, 6–14, 6–15), and are also potential sources of Al (Table 3: 3–15, Table 6: 6–13).

The persistence of bastites in prograde environments where lizardite mesh-textures have been replaced by antigorite has been described by Dungan (1979b). Caruso & Chernosky (1979) have suggested that Al-bearing lizardites have a higher thermal stability than low-Al antigorites at low pressures. These observations are in agreement with the results of the present study, but the mineralogical and chemical aspects of the persistence of bastites in prograde regimes is more complex and more varied than previously expected. Three different processes have been observed in pyroxenes and pyroxene bastites affected by prograde metamorphism: 1) serpentinization of pyroxene to lizardite (or lizardite + secondary diopside) during the simultaneous development of prograde chrysotile + brucite or antigorite ± brucite; 2) recrystallization of lizardite bastites to a chlorite-like mineral + antigorite during the development of prograde antigorite + brucite, and 3) recrystallization of Povlen-type-chrysotile bastites to antigorite during the development of prograde antigorite.

The first case, that of direct serpentization of relict pyroxenes during prograde metamorphism, was observed for both enstatite (18544) and diopside (AG64–64a). In the enstatite example the rock was only slightly serpentinized before a prograde event produced antigorite + brucite from the olivine, and minor relict lizardite + brucite mesh-textures (Figs. 15e, 16) and lizardite from the enstatite (Fig. 15f). The lizardite formed directly from the enstatite has an Fe content similar to the enstatite (Fig. 16: 10–7) but the lizardite away from the enstatite has undergone a large loss of Fe which produces abundant secondary magnetite (Fig. 15f) and a small loss of Al and Cr (Fig. 13: 10–7 to 10–11) in response to the continuing prograde metamorphism. The end product, lizardite, has the same Fe content (Fig. 16), but slightly higher Al and Cr contents, as the newly formed antigorite + brucite mixtures. However, weak antigorite reflections in some of the diffraction patterns from this Fe-poor lizardite indicate that the lizardite bastite has begun to recrystallize directly to antigorite, although there is no optical expression of this.

In the diopside example the olivine has been completely serpentinized to type-3 and type-5 chrysotile + lizardite mesh-textures and the diopside has been partly serpentinized to multilayer lizardite + secondary diopside (Table 11). The chrysotile + lizardite mesh-textures have been partly replaced by antigorite but the lizardite after diopside has not been replaced, probably because of its relatively high Cr and moderate Al contents (Fig. 8: 6–14, 6–15). Presumably the diopside continues to react to form lizardite + secondary diopside as the antigorite develops around it. The secondary diopsides have formed throughout the chrysotile + lizardite mesh-textures often attached to secondary magnetite and are not directly attached to the primary diopside or lizardite bastite. Secondary diopside + antigorite have been described by Peters (1968) and Trommsdorff & Evans (1972) and secondary diopside + lizardite have been described by Dungan (1979a). However, in sample AG67–64a, the secondary diopsides have developed in association with both lizardite and antigorite.

An example of enstatite altering to lizardite as olivine alters to chrysotile + brucite concludes the discussion on this type of bastite development. Sample 18538 seems to have experienced mild retrograde serpentinization which produced lizardite mesh-rims and relict olivine mesh-centres and minor lizardite + iowaite after enstatite. Later, during prograde metamorphism, the relict olivine was altered to chrysotile + minor brucite but the enstatite continued to alter to lizardite. Since there is no relict olivine or enstatite, confirmation of this interpretation is not possible. However, this interpretation is supported by the very low brucite content of the chrysotile + brucite formed after olivine (Fig. 11b) and the presence of chrysotile-asbestos veins. Both features can be accounted for by the loss of Si from the enstatite during the prograde event. The difference in composition between the lizardite of the bastite and the chrysotile probably prevented the replacement of lizardite by chrysotile (Table 7). However, the relict lizardite mesh-rims and chrysotile have very similar compositions (Table 7) and yet the chrysotile does not replace the lizardite, suggesting that chrysotile + lizardite of similar compositions can coexist during mild prograde metamorphism.

The second case, that of recrystallization of lizardite enstatite-bastite to a chlorite-like mineral + antigorite, was observed to occur in two ways during the recrystallization of chrysotile + brucite assemblages to antigorite + brucite assemblages (Figs. 15c, 17a). In sample W70–35 the recrystallization produced little visible effect (Fig. 15c), but a major chemical change occurred. Iron was lost (Fig. 16: 9–5, 9–6) until the Fe content reached that of the surrounding antigorite + brucite assemblage. Aluminum and chromium were also lost (Fig. 13) but did not reach the amounts in the antigorite + brucite. In sample W70–55 the recrystallization is visible as large blades of the chlorite-like mineral + variable amounts of both lizardite and antigorite (Fig. 17a). The chemical changes during recrystallization occurred with a large increase in Fe (Fig. 18: 10–14 to 10–17) and with a variable increase in Al and a drop in Cr (Table 10, Fig. 13: 10–14 to 10–17). According to Caruso & Chernosky (1979), chlorite + antigorite would persist to higher temperatures than lizardite at high pressures, and lizardite to higher temperatures than antigorite at low pressures. However, the addition of Al to antigorite, such as in the present case, would expand the stability field of chlorite + antigorite to lower pressures.

The third case, that of Povlen-type-chrysotile bastite recrystallizing to antigorite, was observed to occur in two samples that have undergone recrystallization of the lizardite hourglass-textures to antigorite (18540, 18543), and in one sample of well-developed prograde antigorite (W76–5). The origin of the Povlen-type-chrysotile bastites is not known because no intermediate developmental stages have been found. In one sample (18543) the bastites have undergone a large loss of Fe (Fig. 18: 12–3, 12–4) and particularly Al and Cr (Fig. 13: 12–3, 12–4) in response to the prograde event and could have, during this loss, recrystallized from normal lizardite-bastites to Povlen-type-chrysotile bastites. This interpretation is supported by the development of chrysotile after lizardite in bastites in sample 18500 in response to a prograde event (Wicks & Whittaker 1977, Cressey 1979). However, it is also possible that the Povlen-type-chrysotile bastite may have formed directly from enstatite during the prograde development of the lizardite hourglass-textures.

The antigorite that replaces the Povlen-type-chrysotile bastites is more Fe-rich in two samples (Fig. 6: 3–13, 3–14, 11–2 to 11–4, Fig. 18: 12–3, 12–4, 12–7). The third sample (W76–5) is more complex and puzzling. Well-formed low-Fe (Fig. 18: 11–15) and -Al (Fig. 13: 11–15) but relatively high-Cr bastites (Fig. 13: 11–15) of Povlen-type chrysotile recrystallize at their margins to higher Fe and lower Cr Povlen-type chrysotile (Fig. 17d), and are associated with zones of more Fe-rich, Cr-poor Povlen-type chrysotile that occur surrounded by, and probably replaced by, antigorite. This migration of Fe is in the opposite direction to the migration in the other samples but the textural relationships between the Fe-rich Povlen-type chrysotile and antigorite are not clear and the problem must be studied further. The process is also complicated by the presence of minor magnetite and carbonate along the edges of some of the bastites.

In summary, it can be seen that bastites do not remain inert during prograde metamorphism, but have several possible paths of recrystallization. Generally, but not always, they lose Fe (Figs. 16, 18), Al and Cr (note the contraction of Fig. 13 compared with Fig. 8) during prograde metamorphism. It is clear that the identification criteria given for bastites by Wicks & Whittaker (1977, Table 4, p. 477), can only be used for identification of retrograde bastites.

Shearing

The effect of shearing was studied only in the prograde regime. The chaotic conditions produced by shearing result in the development of a wide range of Fe contents in both the chrysotiles produced in type-6 (Figs. 11e, 11f) and in the antigorites in type-8 (Fig. 17f) prograde shearing. However, the method of recrystallization in the two environments is quite different. In the chrysotile type-6 assemblages (Figs. 11e, 11f), the recrystallization of relict textures takes place mainly at the edge of the enclosed lens and, to a lesser degree, along internal shear planes where mechanical destruction is a major factor in the recrystallization to the new chrysotile (Fig. 14). Within the lens the relict chrysotile + lizardite mesh-textures and the antigorite are relatively unaffected except where shear planes pass through the lens. The replacement of antigorite by chrysotile as a result of prograde shearing should dispel the idea that a strong shearing-stress is necessary for the development of antigorite. In the antigorite type-8 assemblage (Fig. 17f), antigorite develops as blades and fibres along shear zones where mechanical disruption occurs (Fig. 19: 13–10 to 13–12), but antigorite also develops throughout the rock as foliated and randomly oriented recrystallization products of lizardite–$1T$ hourglass-textures and bastites (Fig. 19: 13–7 to 13–9). This would suggest that temperature as well as mechanical disruption was an important factor in the development of this type-8 assemblage. The effect of even a mild stress on the Fe-content is illustrated in sample 18498, in which minor foliated antigorite has a slightly higher Fe content (Fig. 18: 18498; unmarked point is a single analysis) than the more abundant randomly oriented antigorite (11–22).

The role of mechanical disruption in recrystallization is also demonstrated in sample 18543 in which an Fe-poor, Povlen-type chrysotile–$2M_{c1}$ has developed in closely related cross-fibre asbestos (Fig. 17c), and slip-fibre veins during retrograde fracturing and shearing after the development of prograde antigorite. The cross-fibre veins do not react with the Fe-rich wall-rock antigorite (Figs. 17c, 18) but the chrysotile in the slip-fibre veins does react and replace some antigorite.

Veins and wall-rock recrystallization

The veins encountered in serpentinites may be chemically related to the host serpentine, although they are usually slightly Fe-poor, or they may be chemically dissimilar. Many veins do not react with the wall-rock serpentines but other veins do. Whether or not a vein does react depends on vein and wall-rock chemistry and temperature.

Retrograde type-3 lizardite ± brucite mesh-texture assemblages typically contain veins of lizardite or nonfibrous chrysotile such as the early lizardite veins in sample 18479 (Fig. 9c). The composition of the host lizardites is slightly variable (Table 2, Fig. 7: 2–12 to 2–15, Table 3, Fig. 6: 3–7, 3–8). The composition of the vein lizardite has the Al content of the bastites and generally lower Fe, but is obviously related to the host minerals (Table 4, Fig. 7: 4–1). The later, complex veins (Fig. 9c) with higher-Al, low-Fe multilayer-lizardite margins (Table 4: 4–2, 4–3, 4–6) have a very different composition compared with the host lizardite but nowhere does the multilayer-lizardite marginal zone react with the host lizardite–$1T$ mesh-textures, bastites or earlier veins. The central zone is composed of low-Al moderate-Fe chrysotile–$2M_{c1}$ so that the vein could be a natural example of the partition of Al between lizardite and chrysotile if equilibrium has been reached. The source of the Al for these veins is the serpentinizing pyroxene. The lack of reaction between the vein and wall rock probably reflects the fact that retrograde serpentinization proceeded with decreasing temperature, producing early- to intermediate-stage mesh-textures and the low-temperature veins.

In sample 18530 multilayer-lizardite veins (Fig. 5c; WW, Fig. 6a) developed in association with the serpentinization of enstatite to multilayer lizardite. The composition of the multilayer lizardite in the veins and the lizardite–$1T$ in the mesh textures is quite similar (Figs. 6, 12) but there is extensive recrystallization of mesh centres to multilayer lizardite of the same composition as the veins. High Al is not the only reason for the development of multilayer lizardites, as examples of lizardite–$1T$ of similar or higher Al contents are present in mesh rims and mesh centres. The reaction of the vein material with the wall rock probably occurs because temperatures were high enough to promote the reaction. It is probable that this condition was produced by a very mild prograde event. Wicks & Whittaker (1977) classified multilayer-lizardite textures as part of type-5, prograde serpentinization. This may not be entirely correct. Multilayer-lizardite textures are closely associated with the serpentinization of pyroxene late in type-3 retrograde serpentinization, as illustrated by sample 18479, but the more active recrystallization of wall rock may be related to mild prograde conditions as illustrated in sample 18530. Thus multilayer lizardites may occur in both types of serpentinization so that in some cases they represent another connection between retrograde type-3 and prograde type-5 textures.

Unfortunately, veins were not encountered in all the prograde samples studied. However, in some of the samples that were analyzed the composition of the pre-antigorite host mineral seems to control the composition of the veins that develop after an antigorite + brucite prograde event. Thus after the antigorite + brucite development in sample W70–41a (Fig. 15d), the chrysotile + brucite slip-veins (Fig. 15d) contain chrysotile of a similar composition to the earlier rock-forming chrysotile (Table 9, Fig. 16). Similarly in sample W70–55, in spite of the development of the Fe-rich chlorite-like mineral + antigorite in the bastites and minor Fe-rich antigorite replacement of chrysotile in the chrysotile + brucite textures, the chrysotile–$2M_{c1}$ cross-fibre-asbestos veins that develop after the antigorite event are very similar in composition to the dominant chrysotile serrate veins and hourglass textures (Table 10, Fig. 18). This suggests that the composition of the vein solutions was influenced or controlled by the composition of the rock-forming chrysotile and not the antigorite.

The chemistry of the retrograde serpentine surrounding a chrysotile vein seems to continue to control the composition of the vein even as the vein responds to a prograde event such as the shearing of type 6. Thus the chrysotile asbestos veins and the chrysotile mesh-rims within the lens of retrograde chrysotile + lizardite mesh-textures (Figs. 11e, 11f) are recrystallized to chrysotile slip-veins by the movement along the shear planes associated with the development of the prograde foliated chrysotile surrounding the lens, but retain a composition more similar to the retrograde textures (particularly the chrysotile rims) than most of the newly generated prograde textures (Table 8, Fig. 14).

However, the bulk composition of the rock-forming mineral does not always prevail. In sample W70–35, slightly Fe-rich veins of chrysotile + lizardite react with and replace both the rock-forming antigorite and the earlier chrysotile cross-fibre-asbestos veins (Table 9, Figs. 17b, 16), illustrating that veins can affect the rock-forming minerals.

In antigorite type-7 prograde textures the veins bear a complex relationship to the antigorite. In samples 18540, AG67–67b and W70–72 the chrysotile veins clearly form after the development of minor antigorite (Figs. 5e, 9b) but in two cases, 18540 and AG67–67b, they are also slightly disrupted by the antigorite. Regardless of the minor disruption of the antigorite, the composition of the chrysotile veins in 18540 is intermediate between the host lizardite hourglass-texture and Povlen-type-chrysotile bastite (Fig. 6). In both AG67–67b and W70–72 the chrysotile is less Fe-rich than the associated lizardite and antigorite (Figs. 6, 10) but have similar minor-element contents (Tables 2, 4, 6, 11). In sample 18543 the development of antigorite is well advanced, unlike the previous examples, but the chrysotile cross- and slip-fibre veins following antigorite development have the Fe composition of the relict lizardite hourglass-textures (Table 12, Fig. 18) although the minor-element compositions between all major phases, except the bastites, are similar. This suggests that after the antigorite event the composition of the veins was influenced by the relict retrograde serpentines, not by the antigorite.

Only one sample (AG67–64a) containing several generations of veins was studied (Fig. 11a). The mildly prograde type-3 and -5 chrysotile + lizardite mesh-textures are first cut by chrysotile cross-fibre-asbestos veins with a composition similar to the chrysotile mesh-rims, except where they pass through lizardite bastites after diopside and pick up Cr (Table 6). Following the cross-fibre veins there was development of successive, closely-spaced generations of veins, each with distinctive morphology and slightly different compositions. Thus the chrysotile–$2M_{c1}$ cross-fibre-asbestos veins were later disrupted by chrysotile–$2Or_{c1}$ slip-veins which in turn were disrupted by lizardite–$1T$ and $2H$ veins that occupy some of the same fractures (Fig. 11a). There is a slight increase in Fe and decrease in Al between each closely related generation (Table 6: 6–16 to 6–18). If the serpentinized diopside is the source of the aluminum, the decrease in aluminum among the successive veins may represent a decrease in degree of serpentinization of diopside. In terms of the MgO–FeO–SiO_2 diagram (Fig. 10), each successive generation moves away from antigorite compositions. However, a final set of relatively Al-rich antigorite veins (Table 11: 11–6, 11–7) accompanying the prograde development of antigorite may represent a regeneration of the serpentinization of the diopside to multilayer lizardite + secondary diopside.

Thus although the relationship of the veins to the host minerals is complex, there are many cases in which a close chemical relationship is apparent between the vein serpentine and the host minerals. There is also a close mineralogical relationship. Although the serpentine minerals may be different, the relative abundance of the accessory minerals brucite and magnetite is usually the same in the veins as in the host rock. The cases in which the vein has a very different chemical composition are less abundant but where the rock-forming and the vein-forming serpentines differ in composition, there are often differences in the abundance of accessory minerals.

Role of chlorine

Rucklidge & Patterson (1977) examined olivines partly altered to mesh textures and found that Cl occurs in association with the serpentine adjacent to relict olivine. Rucklidge & Patterson proposed that Cl, probably as $Fe_2(OH)_3Cl$, was present as an active component at the serpentinization front. Later Miúra & Rucklidge (1979) found that Cl was associated with very fine-grained serpentine without any associated hydroxyl-chlorides and suggested that the Cl was simply adsorbed on positively charged crystal-surfaces.

In the present study, Cl was most frequently detected in early-stage retrograde type-3 lizardite ± brucite mesh-textures and bastites, rarely in the late-stage textures, and almost never in type-3 and -5 lizardite ± brucite hourglass-textures and chrysotile + lizardite mesh-textures. It seems to be absent in almost all the prograde mineral-assemblages formed after olivine or products of its serpentinization with the exception of one sample (18478), in which it was consistently detected in all points analyzed in both lizardite–$1T$ mesh-rims and the antigorite blades formed after the lizardite. Chlorine occurs infrequently in prograde lizardite-bastites and in the associated recrystallized chlorite-like mineral + antigorite, but was invariably detected in the lizardite within the magnetite atoll-structure near the relict enstatite in sample 18544. It is absent in the Povlen-type-chrysotile bastite associated with antigorite textures. In one lizardite–$1T$ bastite associated with chrysotile + brucite textures it probably occurs in iowaite. Chlorine has also been found in iowaite in other serpentinites from Iowa (Kohls & Rodda 1967) and Manitoba (Wicks 1969).

These results should not be given too much emphasis; they were gathered as a secondary observation and are not the results of an extensive study directed at Cl distribution. Chlorine was only noted where encountered in the serpentines being analyzed; no attempt was made to find Cl-bearing phases. The iowaite was discovered by accident. Chlorine does appear to be present in some active fronts of serpentinization and probably participates in the serpentinization process. However, it is probably not essential to the process; its presence may simply reflect its initial presence in the water responsible for serpentinization.

CHEMICAL RELATIONSHIPS AMONG THE SERPENTINE MINERALS

An explanation for the distribution of analyses on the MgO–FeO–SiO_2 (Fig. 1) and MgO–Al_2O_3–SiO_2 (Fig. 2) diagrams can now be given. Antigorites from all prograde type-7 and -8 assemblages and from the single retrograde type-1 assemblage all plot above the Mg_3–$Fe^{2+}{}_3$ composition line and form a distinctive group on the MgO–FeO–SiO_2 diagram (Fig. 1).

The large group of $1T$ and multilayer lizardites that plot closer to the Mg_3–Mg_2Fe^{3+}

composition line than the Mg_3–Fe^{3+}_2 composition line (Fig. 1) all occur in retrograde type-3 lizardite ± brucite assemblages (Figs. 6, 7) and in relict retrograde type-3 assemblages in various prograde rocks (Figs. 12, 14, 16, 18). The second group of lizardites that plots along the Mg_3–Fe^{2+}_3 and Mg_3–Fe^{3+}_2 composition lines is composed at both the Fe-poor and Fe-rich ends of lizardites from retrograde type-3 textures (Fig. 6). The intermediate-Fe lizardites of this group occur in rocks that have been partly altered to antigorite type-7 (Figs. 6, 10, 18) or type-8 (Fig. 19) prograde assemblages. Two lizardite bastites of this group (Fig. 16: 10–7, 10–10) have formed in an antigorite + brucite environment. In the first case the compositions of the lizardites have been modified by the development of antigorite, or perharps the lizardites have begun to recrystallize to antigorite. In the second case the lizardites have formed at the same time and in the same environment as antigorite.

The group of Fe-poor chrysotiles, including Povlen-type chrysotiles, that plot near or below the Mg_3–Mg_2Fe^{3+} composition line (Fig. 1) occur in prograde rocks, either of chrysotile ± brucite type-5 (Fig. 12), antigorite ± brucite type-7 (Figs. 16, 18) or lizardite hourglass-texture type-3 and -5 (Fig. 6: 4–17) assemblages. The second group of more Fe-rich chrysotiles that plot along the Mg_3–Fe^{2+}_3 and Mg_3–Fe^{3+}_2 composition lines occur in veins in retrograde type-3 assemblages (Fig. 7) or in chrysotile prograde type-6 assemblages (Fig. 14). Two others of the second group occur in veins and mesh rims in chrysotile + lizardite type-3 and -5 mesh-textures (Fig. 10) that have been partly replaced by antigorite type-7 assemblages. The small third group of chrysotiles that plot well above the Mg_3–Fe^{3+}_2 composition line, within the antigorite group, occur in prograde lizardite hourglass-textures (Fig. 6) and in chrysotile + lizardite mesh-textures (Fig. 10), all partly replaced by antigorite type-7. The composition of some chrysotiles involved in prograde antigorite-producing metamorphism seems to be modified (as are the compositions of some lizardites) toward that of antigorite.

Thus antigorite, chrysotile and lizardite each have their own distinctive distribution pattern on the MgO–FeO–SiO_2 diagram. The overlap of chrysotiles and lizardites with antigorites occurs only where these two minerals have been affected by, or formed during, an antigorite prograde event. There is overlap of Fe-poor chrysotiles and lizardites, but at intermediate Fe contents, chrysotiles follow the Mg_3–Fe^{2+}_3 and Mg_3–Fe^{3+}_2 composition lines and lizardites, except for those affected by prograde antigorite, parallel the Mg_3–Mg_2Fe^{3+} composition line. At high Fe contents lizardites plot near the Mg_3–Fe^{2+}_3 and Mg_3–Fe^{3+}_2 composition lines.

The maximum FeO values of 12% for antigorite, 9% for chrysotile and 16% for lizardite are considerably greater than those given by Whittaker & Wicks (1970), but are difficult to discuss specifically without knowledge of the oxidation state of the Fe. The chrysotile at 9% FeO value is composed of Povlen-type chrysotile–$2M_{c1}$ or $2Or_{c1}$ and minor Povlen-type parachrysotile, but all three, as indicated by the microbeam diffraction-patterns, have imperfectly formed cylindrical structures. This could mean that this FeO value is beyond the limit for well-formed cylindrical chrysotile structures. The fact that with high Fe-values lizardites leave the Mg_3–Mg_2Fe^{3+} composition line and plot near the Mg_3–Fe^{3+}_2 composition line may mean that the limit of Fe^{3+}-for-Si substitution is reached near an FeO value of 11 to 12% and that further Fe^{3+}-for-Mg substitution in lizardite is coupled with vacancies in the octahedral sheet to maintain overall charge-balance. Further Mössbauer investigations on well-studied samples are needed.

The serpentine minerals do not plot in distinct groups on the MgO–Al_2O_3–SiO_2 diagram (Fig. 2) but because there is no problem of oxidation state, more information can be obtained on Al substitution. The fact that only two chrysotiles containing over 1% Al_2O_3 and eight antigorites up to 3% Al_2O_3 occur on Figure 2, whereas nearly three dozen lizardites ($1T$ and multilayer polytypes) plot at greater than 1% Al_2O_3 values, could be interpreted as a demonstration that the curved antigorite and chrysotile structures do not accept much Al in substitution. However, this may simply be an expression of the scarcity of Al in serpentinized ultramafic rocks. Most of the three dozen Al-rich lizardites are pseudomorphic after pyroxene, which is relatively Al-rich. One Povlen-type-chrysotile–$2Or_{c1}$ bastite (12–3) plots at an Al_2O_3 value of 4%. Although this sample is a Povlen-type chrysotile, the symmetry of the microbeam diffraction-patterns indicates that it also contains a well-developed cylindrical structure, presumably in the core. This single sample shows that under some conditions where Al is available, chrysotile will accept it at least up to this Al_2O_3 value. Gillery (1959) and Chernosky (1975) found in their hydrothermal studies that chrysotile is produced up to a limit of $x = 0.25$, where $x = Al$ in the formula $(Mg_{6-x}Al_x)(Si_{4-x}Al_x)O_{10}$

$(OH)_8$; this is equivalent to 5.3% Al_2O_3 on Figure 2. Sample 12–3, at an Al content near $x = 0.2$, suggests that in nature the limit of Al substitution in chrysotile might be greater than that found in hydrothermal studies.

The substitution of Al in the octahedral and tetrahedral sheets of the serpentine structure reduces the mismatch between these two sheets and ultimately eliminates curved structures (Wicks & Whittaker 1975). The amount of Al substitution required to produce a fit between the two sheets, $b_{oct} = b_{tet}$, has been calculated in terms of the b parameters as $x = 0.75$ by Radoslovich (1962) and in terms of the areas of the sheets as $x = 0.6$ by Caruso & Chernosky (1979). These correspond to Al_2O_3 values of 15.8% and 12.7% respectively on Figure 2; neither chrysotile nor antigorite would approach these limits, but their actual limits are not known.

Figure 2 presents more information on Al substitution in lizardite. Although many lizardites plot below the 1% Al_2O_3 value, many (particularly in bastites) plot at up to 7% Al_2O_3 and three from a vein (4–2, 4–3, 4–6) plot at up to 19% Al_2O_3. This provides further evidence for a solid solution between lizardite and amesite. Gillery (1959) found that Al substitution promoted 6-layer structures in hydrothermal studies. In the natural specimens in Figure 2 all multilayer lizardites plot from 1 to 19% Al_2O_3 and lizardite–1*T* samples from 0.3 to 5% Al_2O_3 values. This overlap in composition indicates that Al is not the only factor involved in multilayer-lizardite development. The position of the Al-rich lizardites near the Mg_3–Mg_2Al composition line indicates an approximately equal distribution of Al between octahedral and tetrahedral sites.

Figure 3 illustrates that substitution for Si in the tetrahedral sites of both vein-forming and rock-forming chrysotiles and of antigorite (even when adjusted for the effect of the structural formula) is very limited. This is not surprising in view of their low Al values illustrated in Figure 2. Lizardites have the greatest range of substitution. Those formed after olivine and some of those formed in veins have the least extensive, and those after pyroxenes and those in the rest of the veins the most extensive substitution. The multilayer lizardites generally have more substitution than the single-layer polytype. These greater substitutions in lizardite bastites and multilayer lizardites also reflect the high Al-contents illustrated in Figure 2.

CHRYSOTILE-ASBESTOS DEPOSITS

The characteristic association of serpentine textures found in asbestos deposits was discussed by Wicks & Whittaker (1977). In the present study, samples were selected to represent various types of textures and not various asbestos deposits. Nevertheless, over half the samples are from mines (Table 1) and illustrate some of the chemical processes of chrysotile-asbestos development.

There is evidence of a limited retrograde type-3 lizardite ± brucite serpentinization in some asbestos deposits but the main serpentinization has been a prograde event that has developed a variety of serpentine textures and the chrysotile asbestos veins. The prograde event may be fairly mild with the development of chrysotile ± lizardite ± brucite, intermediate with the development of antigorite + brucite, or sufficiently intense to produce minor but not extensive amounts of antigorite without brucite. The chrysotile veins develop at all stages and seem relatively unaffected by the development of minor antigorite, but extensive development of antigorite eliminates chrysotile-asbestos veins. However, some veins may form in the retrograde environment after the development of antigorite.

The asbestos veins are chemically and mineralogically related to the host rock. There is a strong trend for the development of Fe-poor serpentine minerals in the rock-forming chrysotile ± lizardite ± brucite and antigorite + brucite assemblages and in the associated asbestos veins. However, there are exceptional instances of Fe-rich serpentine, particularly in shear zones. When antigorite ± magnetite assemblages begin to develop the antigorite is often fairly Fe-rich, but the postantigorite chrysotile-asbestos veins are usually related chemically to the associated relict pre-antigorite serpentines.

IMPLICATIONS FOR PHASE DIAGRAMS

The results of the present study have a bearing on parts of the serpentine phase-diagram. Lizardite is the most abundant product of retrograde low-temperature serpentinization but the observation of its occurrence in a number of prograde serpentinites (with and without chrysotile) in this study indicates that it has a stability field as great as that of chrysotile. Specifically, lizardite was observed as the major serpentine in hourglass textures of types 3 and 5 and in interpenetrating textures of type-5 prograde serpentinization. Lizardite was also observed as a major component with chrysotile in mesh textures of type-5 prograde serpentinization. In addition, lizardite bastites after enstatite that apparenly formed during chrysotile + brucite type-5 serpentinization were observed. The serpentinization of pyroxene to lizardite during type-7 prograde serpentinization was observed for both enstatite to lizardite during antigorite + brucite serpentinization and for diopside to lizardite + secondary diopside during antigorite + secondary diopside serpentinization, suggesting that lizardite + antigorite may be a common association in this type of serpentinization. Lizardite bastites were also observed reacting to a chlorite-like mineral + antigorite (± lizardite) during antigorite + brucite prograde serpentinization.

Perhaps the strongest evidence of a stability field for lizardite similar to that for chrysotile is the observation of Fe-poor antigorite replaced by an intimate mixture of slightly more Fe-rich chrysotile and lizardite. If a stability field for chrysotile can be inferred from the observation of chrysotile forming directly from antigorite (Evans *et al.* 1976), it follows that a similar stability field for lizardite can be inferred from the observation of lizardite forming from antigorite. Furthermore it has been shown that, except for the cylindrical structure, chrysotile and lizardite have many structural similarities (Wicks & Whittaker 1975), may coexist within a Povlen-type fibre (Middleton & Whittaker 1976, Cressey & Zussman 1976), and often form together in mesh centres, bastites and hourglass textures (Cressey 1979).

The composition of lizardite bastites is usually more Al- and Cr-rich, and often more Fe-rich than the associated lizardite after olivine, which tends to be more easily replaced by antigorite. The study by Caruso & Chernosky (1979) has done much to establish the importance of Al in the stability of lizardite; further studies extending Moody's (1976) investigation of the effect of Fe, although difficult, are now required to establish fully the relationships of lizardite, antigorite and chrysotile. Data on the effect of Cr are also needed. Studies of the opaque minerals and other phases are also required to provide further details of the process.

The presence of Povlen-type-chrysotile bastite after enstatite and its alteration to antigorite during type-7 prograde serpentinization was surprising. It is not known whether the Povlen-type chrysotile formed directly from enstatite or after lizardite bastites. More studies on partly altered enstatites are required. Detailed studies are needed on the nature of the Povlen-type chrysotile to establish whether the outer polygonal zone has chrysotile- or lizardite-type stacking.

The eight types of serpentinization were proposed by Wicks & Whittaker (1977) to help unravel the complexities of serpentine-mineral textures and to emphasize that serpentinization is not one, but several processes. They were not meant to substitute for phase diagrams. As a result of the present study it was discovered that lizardite ± brucite hourglass-textures and chrysotile + lizardite ± brucite mesh-textures, although closely related to lizardite ± brucite type-3 retrograde textures, are promoted by prograde type-5 serpentinization and thus form a bridge between type-3 and type-5 serpentinization. Similarly, multilayer lizardites are closely related to the retrograde type-3 serpentinization of pyroxenes, but their full development is promoted by mild prograde type-5 serpentinization, so that they also form a bridge between type-3 and type-5 serpentinization.

ACKNOWLEDGEMENTS

Our appreciation is extended to the following mining companies that allowed us access to their properties or supplied us with samples: Asbestos Corporation Ltd., Bell Asbestos Mines Ltd., Canadian Johns-Manville Co. Ltd., Falconbridge Nickel Mines Ltd., Flintkote Mines Ltd., INCO Ltd., and National Asbestos Mines Ltd. All the staff of the Department of Mineralogy and Geology at R.O.M. are thanked for their help and encouragement, particularly Miss Helen Driver, Dr. R. I. Gait, Mrs. Joey Gait, Dr. J. A. Mandarino, Mr. Robert A. Ramik and Mr. Vincent Vertolli. The authors gratefully acknowledge the useful comments of Dr. J. V. Chernosky, Jr.

REFERENCES

AUMENTO, F. (1967): A serpentine mineral showing diverse strain-relief mechanisms. *Amer. Mineral.* **52**, 1399-1413.

BLAAUW, C., STROINK, G., LEIPER, W. & ZENTILLI, M. (1979): Mössbauer analysis of some Canadian chrysotiles. *Can. Mineral.* **17**, 713-717.

CARUSO, L.J. & CHERNOSKY, J.V., JR. (1979): The stability of lizardite. *Can. Mineral.* **17**, 757-769.

CHERNOSKY, J.V., JR. (1975): Aggregate refractive indices and unit cell parameters of synthetic serpentine in the system $MgO-Al_2O_3-SiO_2-H_2O$. *Amer. Mineral.* **60**, 200-208.

CRESSEY, B.A. (1979): Electron microscopy of serpentinite textures. *Can. Mineral.* **17**, 741-756.

——— & ZUSSMAN, J. (1976): Electron microscopic studies of serpentinites. *Can. Mineral.* **14**, 307-313.

DUNGAN, M.A. (1977): Metastability in serpentine–olivine equilibria. *Amer. Mineral.* **62**, 1018-1029.

——— (1979a): Bastite pseudomorphs after orthopyroxene, clinopyroxene and tremolite. *Can. Mineral.* 17, 729-740.

——— (1979b): A microprobe study of antigorite and some serpentine pseudomorphs. *Can. Mineral.* 17, 771-740.

Evans, B.W. (1977): Metamorphism of alpine peridotite and serpentinite. *Ann. Rev. Earth Planet. Sci.* 5, 397-447.

———, Johannes, W., Oterdoom, H. & Trommsdorff, V. (1976): Stability of chrysotile and antigorite in the serpentinite multisystem. *Schweiz. Mineral. Petrog. Mitt.* 56, 79-93.

Frost, B.R. (1975): Contact metamorphism of serpentinite, chloritic blackwall and rodingite at Paddy-Go-Easy Pass, Central Cascades, Washington. *J. Petrology* 16, 272-313.

Gillery, F.H. (1959): The X-ray study of synthetic Mg–Al serpentines and chlorites. *Amer. Mineral.* 44, 143-152.

Golightly, J.P. & Arancibia, O.N. (1979): The chemical composition and infrared spectrum of nickel- and iron-substituted serpentine from a nickeliferous laterite profile, Soroako, Indonesia. *Can. Mineral.* 17, 719-728.

Hess, H.H. & Otalora, G. (1964): Mineralogical and chemical composition of the Mayaguez serpentinite cores. *In* A Study of Serpentinite, the AMSOC Core Hole near Mayaguez, Puerto Rico (C.A. Burk, ed.), *Nat. Acad. Sci. – Nat. Res. Counc. Publ.* 1188, 152-168.

Kohls, D.W. & Rodda, J.L. (1967): Iowaite, a new hydrous magnesium hydroxide ferric oxychloride from the Precambrian of Iowa. *Amer. Mineral.* 52, 1261-1271.

Kunze, G. (1956): Die gewellte Struktur des Antigorits. I. *Z. Krist.* 108, 82-107.

——— (1958): Die gewellte Struktur des Antigorits. II. *Z. Krist.* 110, 282-320.

——— (1961): Antigorit. Strukturtheoretische Grundlagen und ihre praktische Bedeutung für die weitere Serpentin-Forschung. *Fortschr. Mineral.* 39, 206-324.

Lapham, D.M. (1964): Spinel–orthopyroxene compositions and their bearing on the origin of the serpentinite near Mayaguez, Puerto Rico. *In* A Study of Serpentinite, the AMSOC Core Hole near Mayaguez, Puerto Rico (C.A. Burk, ed.), *Nat. Acad. Sci. – Nat. Res. Counc. Publ.* 1188, 134-144.

Middleton, A.P. & Whittaker, E.J.W. (1976): The structure of Povlen-type chrysotile. *Can. Mineral.* 14, 301-306.

——— & ——— (1979): The nature of parachrysotile. *Can. Mineral.* 17, 693-697.

Miura, Y. & Rucklidge, J.C. (1979): The structural occurrence of chlorine in serpentine. *Geol. Assoc. Can./Mineral. Assoc. Can. Program Abstr.* 4, 67.

Moody, J.B. (1976): An experimental study on the serpentinization of iron-bearing olivines. *Can. Mineral.* 14, 462-478.

Morandi, N. & Felice, G. (1979): Serpentine minerals from veins in serpentinite rocks. *Mineral. Mag.* 43, 135-140.

Page, N.J (1967): Serpentinization at Burro Mountain, California. *Contr. Mineral. Petrology* 14, 321-342.

——— (1968): Serpentinization in a sheared serpentinite lens, Tiburon Peninsula, California. *U.S. Geol. Surv. Prof. Pap.* 600-B, 21-28.

Peters, T. (1968): Distribution of Mg, Fe, Al, Ca and Na in coexisting olivine, orthopyroxene and clinopyroxene in the Totalp serpentinite (Davos, Switzerland) and in the alpine metamorphosed Malenco serpentinite (N. Italy). *Contr. Mineral. Petrology* 18, 65-75.

Plant, A.G. & Lachance, G.R. (1973): Quantitative electron microprobe analysis using an energy dispersive spectrometer. *Proc. Eighth Nat. Conf. Electron Probe Analysis (New Orleans), Pap.* 13.

Radoslovich, E.W. (1962): The cell dimensions and symmetry of layer-lattice silicates. II. Regression relations. *Amer. Mineral.* 47, 617-636.

Rozenson, I., Bauminger, E.R. & Heller-Kallai, L. (1979): Mössbauer spectra of iron in 1:1 phyllosilicates. *Amer. Mineral.* 64, 893-901.

Rucklidge, J.C. & Patterson, G.C. (1977): The role of chlorine in serpentinization. *Contr. Mineral. Petrology* 65, 39-44.

Trommsdorff, V. & Evans, B.W. (1972): Progressive metamorphism of antigorite schist in the Bergell tonalite aureole (Italy). *Amer. J. Sci.* 272, 423-437.

Whittaker, E.J.W. & Wicks, F.J. (1970): Chemical differences among the serpentine "polymorphs": a discussion. *Amer. Mineral.* 55, 1025-1047.

——— & Zussman, J. (1956): The characterization of serpentine minerals by X-ray diffraction. *Mineral. Mag.* 31, 107-126.

Wicks, F.J. (1969): *X-ray and Optical Studies on Serpentine Minerals.* D.Phil. thesis, Univ. Oxford, England.

——— (1979): Mineralogy, chemistry and crystallography of chrysotile asbestos. *In* Short Course in Mineralogical Techniques of Asbestos Determination (R.L. Ledoux, ed.), *Mineral. Assoc. Can. Short Course* 4, 35-78.

——— & Whittaker, E.J.W. (1975): A reappraisal of the structures of the serpentine minerals. *Can. Mineral.* 13, 227-243.

——— & ——— (1977): Serpentine textures and serpentinization. *Can. Mineral.* 15, 459-488.

———, ——— & Zussman, J. (1977): An idealized model for serpentine textures after olivine. *Can. Mineral.* 15, 446-458.

——— & Zussman, J. (1975): Microbeam X-ray diffraction patterns of the serpentine minerals. *Can. Mineral.* 13, 244-258.

Received October 1979, revised manuscript accepted October 1979.